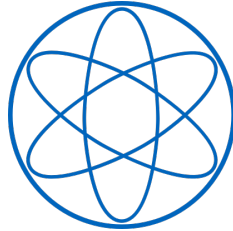


CHAIR OF DARK MATTER (E47)
DEPARTMENT OF PHYSICS



Characterization of the IOV Instrument for the Cube Sat Compton Telescope ComPol

Master's Thesis

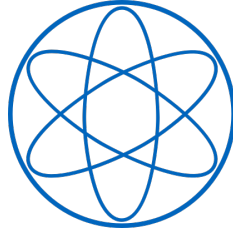
CORDULA GERTRUD MARIA SCHMITZ-SINN



TECHNICAL UNIVERSITY OF MUNICH



TECHNISCHE UNIVERSITÄT MÜNCHEN



FAKULTÄT FÜR PHYSIK
LEHRSTUHL FÜR DUNKLE MATERIE (E47)

Master's Thesis

Characterization of the IOV Instrument for the Cube Sat Compton Telescope ComPol

Author: Cordula Gertrud Maria Schmitz-Sinn
Reviewer: Prof. Dr. Susanne Mertens

I confirm that this master's thesis is my own work and I have documented all sources and material used.

Munich, 2023-06-01

Cordula Gertrud Maria Schmitz-Sinn

Abstract

Black holes, neutron stars and white dwarfs are fascinating objects in the universe. To better understand these compact objects, great efforts have been made in recent decades. But some questions are still unanswered. The Compton Polarimeter (ComPol) is a CubeSat mission to study the spectrum and polarization of the black hole binary system Cygnus X-1 over a period of at least one year in the hard X-ray region to gain new insights into its geometry, accretion disk properties, X-ray emission mechanisms and other features. An adapted instrument is currently being prepared for an in-orbit verification mission on an external platform aboard the International Space Station (ComPol-IOV). The launch is planned for the end of 2023.

The focus of this work is on the characterisation of the Silicon drift detector (SDD) module, the prototype for the ComPol-IOV mission. The physical motivation for the characterisation measurements is to reproduce the angle-dependent Θ -differential cross-section for incoherent scattering by a Compton scattering experiment. Thereby the used setup consists of the SDD module, originally designed for the TRISTAN experiment, as scatter target and a commercially available Lanthanum(III)Bromide detector as calorimeter. The angular dependence of Compton scattering is experimentally achieved by changing the angle between the beam axis of the radioactive source (^{241}Am) and the LaBr_3 calorimeter. In addition, simulations were carried out with a simplified setup consisting of only the two detectors.

With the Compton scattering measurements in the final setup, which avoids shielding by the printed circuit board (PCB), the angle-dependent Θ -differential cross-section for incoherent scattering in the angular range between $\sim 75^\circ$ and $\sim 152^\circ$ could be reproduced. It is also shown that a low energy threshold and thus a good energy resolution of the SDD, is crucial to resolve small scattering angles in particular and likewise to obtain a high sensitivity in the low energy range for the ComPol mission. The results from measurements were confirmed by the simulations to investigate the influence of the lower energy threshold in the SDD module. Furthermore, it was found through simulations that especially at angles around 90° , a longer path length of the photon through the Silicon of the SDD leads to self-absorption in the SDD and thus a lower number of Compton events. This is relevant for the polarization measurements of the ComPol mission, since polarization dependency is highest in this angular range.

Zusammenfassung

Schwarze Löcher, Neutronensterne und Weiße Zwerge sind faszinierende Objekte im Universum. Um diese kompakten Objekte besser zu verstehen, wurden in den letzten Jahrzehnten große Anstrengungen unternommen. Doch einige Fragen sind noch unbeantwortet. Das Compton Polarimeter (ComPol) ist eine CubeSat-Mission, die das Spektrum und die Polarisation des Röntgendoppelstern Systems Cygnus X-1 über einen Zeitraum von mindestens einem Jahr im harten Röntgenbereich untersuchen soll, um neue Erkenntnisse über seine Geometrie, die Eigenschaften der Akkretionsscheibe, die Mechanismen der Röntgenemission und andere Merkmale zu gewinnen. Ein angepasstes Instrument wird derzeit für eine IOV-Mission auf einer externen Plattform an Bord der internationalen Raumstation (ISS) vorbereitet. Der Start ist für Ende 2023 geplant.

Der Schwerpunkt dieser Arbeit liegt auf der Charakterisierung des Silizium-Drift-Detektors (SDD), des Prototypen für die ComPol-IOV-Mission. Die physikalische Motivation für die Charakterisierungsmessungen besteht darin, den winkelabhängigen differentiellen Wirkungsquerschnitt für inkohärente Streuung durch ein Compton-Streuexperiment zu reproduzieren. Der verwendete Aufbau besteht aus dem SDD-Modul, das ursprünglich für das TRISTAN-Experiment entwickelt wurde, welches als Streutarget verwendet wird und einem handelsüblichen Lanthan(III)Bromid-Detektor als Kalorimeter. Die Winkelabhängigkeit der Compton-Streuung wird experimentell durch die Änderung des Winkels zwischen der Strahlachse der radioaktiven Quelle (^{241}Am) und dem LaBr_3 -Detektor realisiert. Darüber hinaus wurden Simulationen mit einem vereinfachten Setup, welches nur aus den beiden Detektoren besteht, durchgeführt.

Mit den Compton-Streuungsmessungen im endgültigen Aufbau, in dem die Abschirmung durch die Leiterplatte vermieden wird, konnte der differentielle Wirkungsquerschnitt für inkohärente Streuung im Winkelbereich zwischen $\sim 75^\circ$ und $\sim 152^\circ$ reproduziert werden. Außerdem wurde gezeigt, dass eine niedrige Energieschwelle und daher eine gute Energieauflösung der SDDs entscheidend ist, um insbesondere kleine Streuwinkel aufzulösen und ebenso eine hohe Sensitivität im niedrigen Energiebereich für die ComPol-Mission zu erhalten. Die Ergebnisse der Messungen wurden durch Simulationen zur Untersuchung des Einflusses der unteren Energieschwelle im SDD-Modul bestätigt. Darüber hinaus wurde durch Simulationen festgestellt, dass insbesondere bei Winkeln um 90° eine längere Weglänge des Photons durch das Silizium des SDD zur Selbstabsorption im SDD und damit zu einer geringeren Anzahl von Compton-Ereignissen führt. Dies ist relevant für die Polarisationsmessungen der ComPol-Mission, da die Polarisationsabhängigkeit in diesem Winkelbereich am größten ist.

Contents

1	Compton Telescopes	1
1.1	Introduction	1
1.2	Cygnus X-1: Scientific Motivation	1
1.3	Interaction of Photons in Matter	5
1.3.1	Photoelectric Effect	5
1.3.2	Compton Scattering	5
1.3.3	Pair Production	7
1.4	Compton Telescopes	7
1.4.1	Event Reconstruction	8
1.4.2	Polarimetry	9
2	The ComPol Project	11
2.1	Silicon Drift Detector (SDD) - in General	11
2.2	ComPol	15
2.2.1	SDD-Detector Modul for ComPol	16
2.2.2	CeBr ₃ -Detector for ComPol	16
2.2.3	Photomultipliers	17
2.2.4	Detector Resolution	17
2.2.5	Data Analysis for ComPol	19
3	Characterization of the Prototype SDD Modul	21
3.1	Scientific Motivation	21
3.2	Experimental Setup	21
3.2.1	The CAEN Digitizer and the used Firmware	25
3.2.2	Experimental Reproduction of the Scattering Angles	27
3.2.3	Including Source Positions	28
3.3	Americium Sources	30
3.4	Analysis Chain	31
3.5	Measurements	35
3.5.1	Measurements with a ⁵⁵ Fe Source	35
3.5.2	Measurement Runs in an Evolving Setup (two Source Positions)	36
3.5.3	Measurement Run in the Rearranged Setup	45
3.6	Simulations	49
3.7	Summary and Discussion	56
4	Conclusion and Outlook	59

A Appendix	61
A.1 Abbreviations and Acronyms	61
A.2 Random Coincidence Events and Propagation of Statistical Uncertainties .	63

Compton Telescopes

1.1 Introduction

Black holes, neutron stars and white dwarfs are fascinating objects in the Universe. To understand these compact objects in more detail, great efforts have been undertaken in the last decades [15]. But still some questions remain. To gain more information it is necessary to expand the observation methods beyond the border of classical imaging. The small size to distance ratio makes it impossible to get knowledge about these compact objects via optical methods. To retrieve data from them other possibilities have been developed. The Compton Polarimeter (ComPol) is a CubeSat mission. Its goal is to investigate the spectrum and polarization of the black hole binary system Cygnus X-1 over the duration of at least one year in the hard X-ray range (20 keV - 2 MeV) to get new insights into its geometry, accretion disk properties, X-ray emission mechanisms, and further characteristics, [36]. The ComPol mission will focus its observation on only one astronomical source as the detector area is very small. Therefore the amount of data which will be collected will be low in comparison to standard X-ray satellite missions.

In section 1.2 the target object Cygnus X-1 is presented briefly. The processes of interaction of photons in matter are described in section 1.3 with focus on Compton scattering in subsection 1.3.2. The working principle of a Compton telescope and polarization measurements are explained in section 1.4.

1.2 Cygnus X-1: Scientific Motivation

The Black Hole Binary (BHB) System Cygnus X-1 is a strong galactic X-ray source located in the constellation Cygnus (swan), consisting of a black hole (BH) and the blue supergiant variable star HDE 226868 [44], see **Fig:** 1.1. The compact object was the first accepted black hole, it was discovered by Bolton et al. [12] in 1972.

In 2021, the mass of the black hole was revised up to 21.2 ± 2.2 times the mass of the sun after the re-determination of the distance to Cygnus X-1 to 7200 light-years by using the Very Long Baseline Array [37]. The compact object and the blue supergiant orbit each other during an orbital period of 5.6 days [13]. The black hole continuously accretes matter from the companion. The X-ray spectrum of Cygnus X-1 strongly fluctuates and several different spectral states can be identified. The states are distinguished by their luminosity and their dominant X-ray energy range, see **Fig:** 1.2

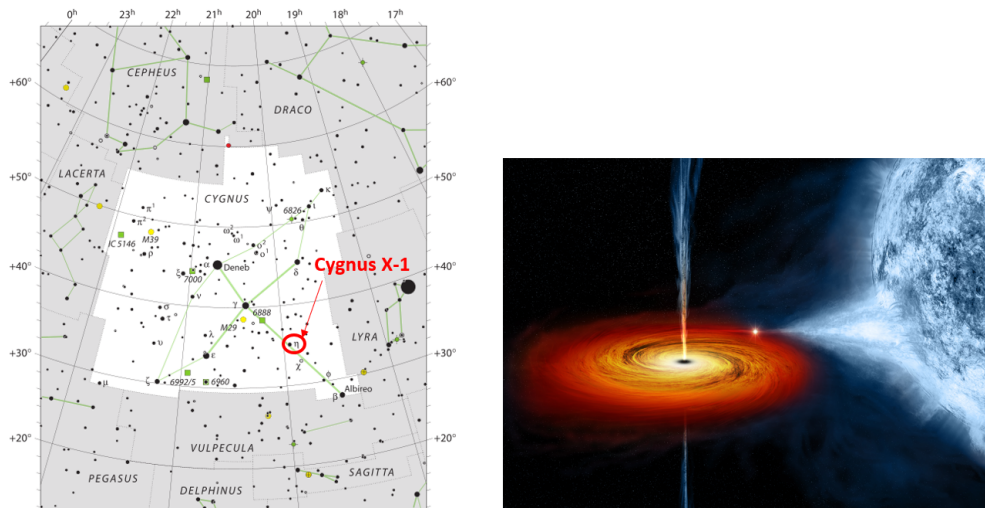


Figure 1.1 Cygnus X-1.

Left: Location of the BHB Cygnus X-1 in the constellation Cygnus (swan). Adapted from [1]

Right: Artist's illustration of Cygnus X-1 accreting material from its companion. Taken from [2]

The **Low Hard State (LHS)** has an maximum emission energy about ~ 100 keV. Its overall luminosity in the X-ray spectrum is lower than in the High Soft State.

The **High Soft State (HSS)** has an maximal emission energy about ~ 1 keV. Its overall luminosity in the X-ray spectrum is higher than in the LHS. [24], [16]. The LHS and HSS spectra are shown in **Fig: 1.2**.

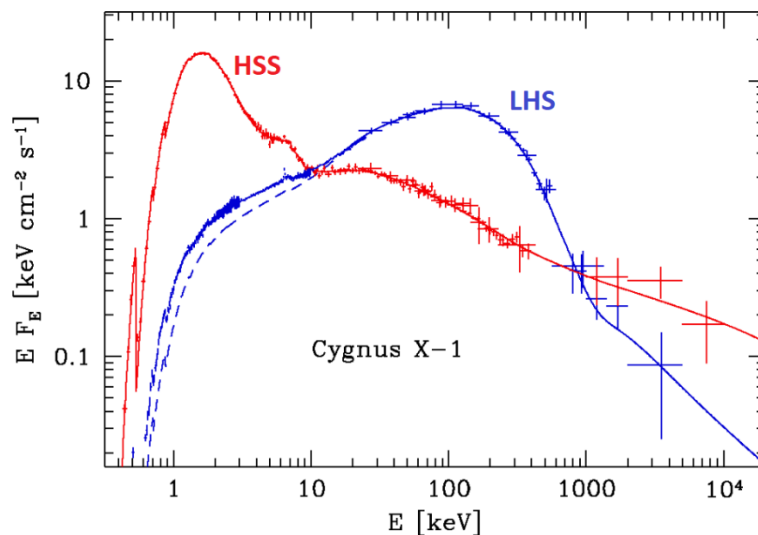


Figure 1.2 Cygnus X-1, Spectra of the two Main States. The two main states of Cygnus X-1, the Low Hard State (blue) and the High Soft State (red) are shown. The Low/High in the name of the state describes the luminosity and Hard/Soft refers to the dominant X-ray energy range of the state. The maximum emission in the LHS is at ~ 100 keV and for HSS at ~ 1 keV. Figure adapted from [43]

The BHB tends to remain in the HSS and the LHS states for several years. But also a far more unstable and short-lived **Intermediate State** can be occupied in between the LHS and the HSS. The LHS was the dominant emission state of Cygnus X-1 during the last 20 years [24], [30]. Both, the LHS and the HSS, consist of a low energy part in between 0.5 keV and 10 keV, a high energy part in between 10 keV and 400 keV and a hard tail

for energies above 400 keV. These parts are differently pronounced depending on the state and can be produced by several physical processes. These are mainly:

Thermal emission, synchrotron radiation and inverse Compton scattering [36],[30]

The importance and the interplay of these processes are not yet completely understood. It is therefore the aim of the ComPol mission to gain more insights into the X-ray production mechanisms of the different states of the system [36].

The LHS

The LHS spectrum of Cygnus X-1 has two main mechanisms that could be responsible, illustrated in **Fig: 1.3**):

Inverse Compton scattering of soft photons in the hot Corona

Theoretical models predict that the black hole and the inner part of the accretion disk are surrounded by a hot corona with a thermal temperature of ~ 70 keV. The photons undergo inverse Compton scattering on these electrons, gain energy from that process and are shifted towards the hard range of the spectrum [16].

Synchrotron emission in the jets

The jets of a BHB consist of a small amount of matter, which does not fall into the black hole. This matter is accelerated perpendicular to the accretion disk. Due to synchrotron radiation in the jet formation region hard X-rays could be created.[43]

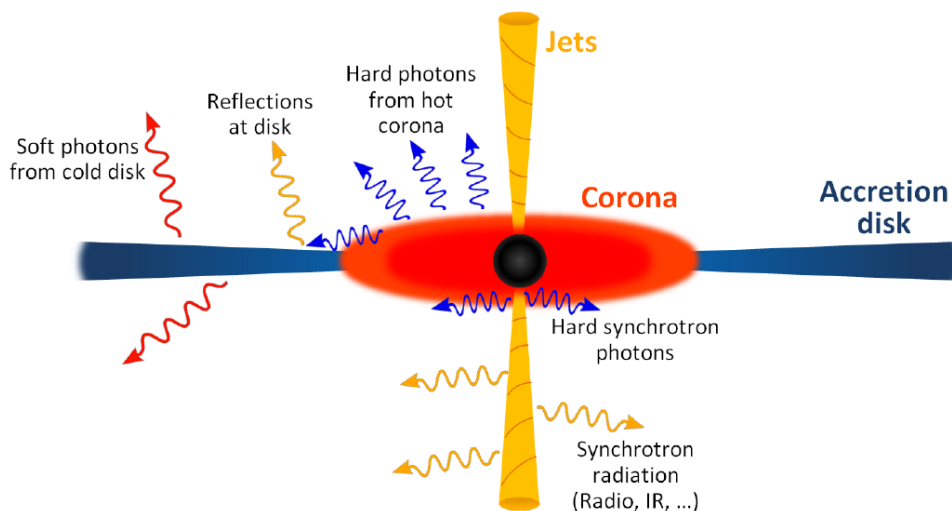


Figure 1.3 Illustration of the Low Hard State, LHS.

A possible geometry and the emission mechanisms for Cygnus X-1 in the LHS are shown. The black hole is indicated by a black circle in the center, the companion star is not shown. In the presence of a Corona, the hard emission can be explained by inverse Compton scattering. Furthermore, hard X-rays are created in the formation region of the jets via synchrotron radiation. Taken from [36].

The HSS

The HSS spectrum of Cygnus X-1 does not match to the presence of a hot corona and further, no radio emission from jets has been detected. It can be concluded that no jet formation exists in the HSS [43]. Without a corona and jets the physical models taken into account are: (shown in **Fig: 1.4**)

Thermal emission of soft X-rays directly from the accretion disk. The disk can reach closer to the black hole, therefore more soft photons can be emitted directly from the disk [36].

Inverse Compton scattering on electrons, which are free falling into the BH.

That process could be responsible for the (weak) high energy component of the HSS [31]. **Synchrotron radiation in the inner accretion disk.** That could generate the faint hard component of the HSS [36], [30].

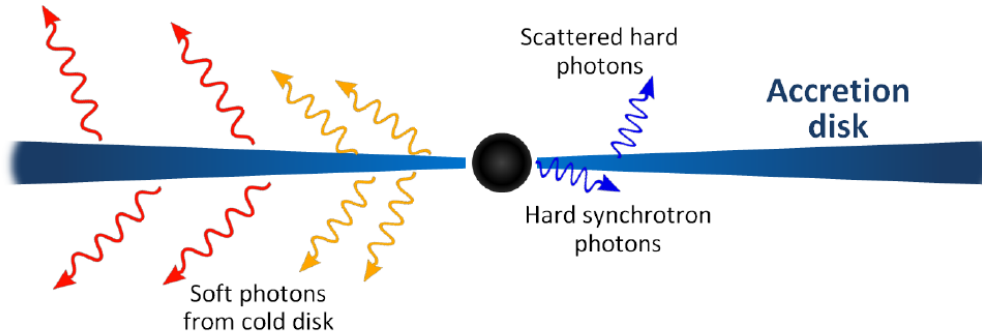


Figure 1.4 Illustration of the High Soft State, HSS. A possible geometry and emission mechanisms for Cygnus X-1 in the HSS are shown. The black hole is indicated by a black circle in the center, the companion star is not shown. Low energetic photons are emitted by the accretion disk. Without a corona, the hard component of the HSS is generated via synchrotron radiation in the inner parts of the accretion disk and via inverse Compton scattering on free-falling electrons. Taken from [36].

The hard X-ray tail of both states can be explained by synchrotron radiation from jets, due to their high degree of polarization [30].

Many further processes to determine a complete model of a BHB have to be taken into account, e.g. geometrical effects, coronal effects, reflections and relativistic effects. Furthermore the mass and the spin of the BH and also the orientation of the system play a huge role in the overall description of such a system.

Concerning Cygnus X-1, still many questions have to be answered: **It is unknown which are the links between the effects mentioned above and the emitted radiation spectrum. Furthermore, it is not known which mechanism causes the states and how the transition between different states works.** Polarization measurements could help to answer some of those open questions as stated in [36]:

Polarized radiation can be produced in a BHB via synchrotron radiation and scattering. The degree of polarization and the plane of orientation of the polarization depends on the composition of the corona and the kinematics of the system. An other important role in X-ray and polarization measurements is played by the orientation of the BHB to the observer. The number of photons reaching the observer from each region of the BHB depends on the alignment to the rotation axis and thus the accretion disc and the jets. By measuring the radiation spectrum and also the degree and plane of polarization in various energy ranges, conclusions can be drawn concerning several parameters of the astrophysical object[36].

The ComPol CubeSat will observe the spectrum of Cygnus X-1 in the energy range between 20 keV and 2 MeV. Simultaneously the polarization for energies up to 300 keV will be measured. An initial sensitivity study had been performed by Matthias Meier [36], determining the minimum detectable polarization (MDP) of ComPol after one year of data taking to 13% [36]. A further study including a conservative estimation for the cosmogenic activation, resulted in an MDP of 17%, [22]. This is in the order of magnitude measured for Cygnus X-1 ($P \leq 20\%$) in the energy range between 250 keV and 400 keV. [39].

1.3 Interaction of Photons in Matter

Photons interact in matter depending on their energy and the properties of the material. The main interaction processes are **photoelectric effect, Compton scattering and pair production**. Dominant processes in the X-ray energy range are photoelectric effect and Compton scattering.

1.3.1 Photoelectric Effect

The photoelectric absorption of a X-ray photon by an electron shell of an atom is denoted as photoelectric effect. If the photon energy is larger than the ionization energy of the electron, the photon is absorbed and an electron is ejected from the shell. The cross section of the interaction process increases step wise when the photon energy exceeds the binding energy of an electron shell. The cross-section further scales with the atomic number Z according to Z^5 and the energy of the $E^{-3.5}$, therefore this process is most prominent in high Z elements and at low energies.

1.3.2 Compton Scattering

Compton scattering, discovered in 1923 by Arthur H. Compton [17], is the inelastic scattering of a photon on a free or nearly free electron. A schematic sketch of a Compton scattering process is shown in **Fig:** 1.5. In this process the incident photon transfers some of its initial energy to the electron, it is deflected by an angle Θ and its wavelength λ is shifted by $\Delta\lambda$ according to:

$$\Delta\lambda = \lambda_C(1 - \cos \Theta), \quad (1.1)$$

with $\lambda_C = h/m_e c$. The energy of the scattered photon $E(\Theta)$, depending on the scattering angle Θ can be calculated as follows:

$$E(\Theta) = \frac{E_0 m_e c^2}{m_e c^2 + E_0(1 - \cos \Theta)}, \quad (1.2)$$

and therefore the energy of the electron $E_e(\Theta)$ is given by:

$$E_e(\Theta) = E_0 - E(\Theta) = \frac{E_0^2(1 - \cos \Theta)}{m_e c^2 + E_0(1 - \cos \Theta)}. \quad (1.3)$$

The energies of the scattered photon and of the scattered electron depending on the scattering angle are shown in **Fig:** 1.5 for an incoming electron with an energy of 59.5 keV, e.g. produced by an Americium (^{241}Am) source.

The differential cross-section for Compton scattering, originally described by Klein and Nishina [28] by using polar coordinates is given by the following equation:

$$\frac{d\sigma_{CS}}{d\Omega} = \frac{r_0^2 \epsilon^2}{2} \left(\frac{1}{\epsilon} + \epsilon - 2 \sin^2(\Theta) \cos^2(\Phi) \right), \quad (1.4)$$

with $\epsilon = E(\Theta)/E_0$, the ratio of the energies of the scattered to that of the incident photon. The classical electron radius is denoted by r_0 , whereas Θ is the scattering angle and Φ the azimuthal scattering angle, describing the angle between the polarization vector ξ of the initial photon and the propagation direction of the scattered photon. Integrating the

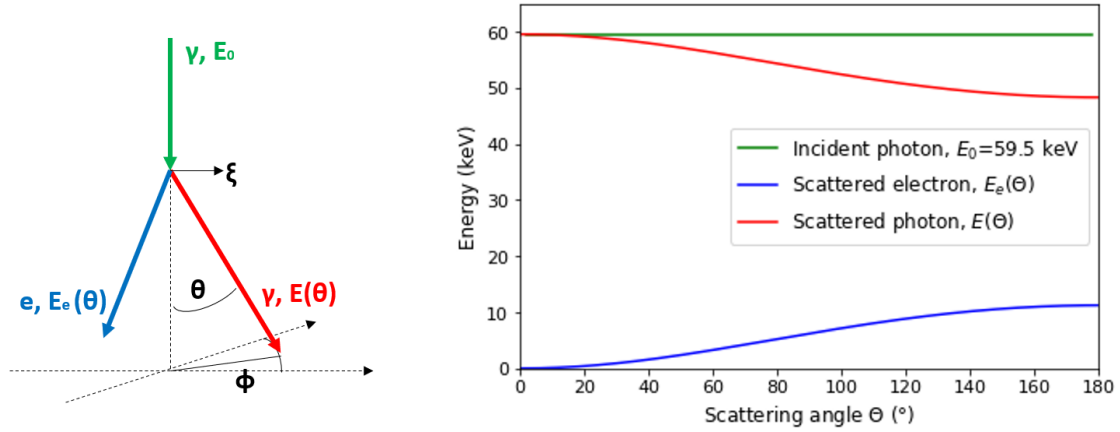


Figure 1.5 Compton Scattering Process.

Left: Schematic sketch of the scattering process. The incident photon (green) with an energy of $E_0=59.5$ keV, e.g. from an Americium (Am^{241}) source, transfers some of its initial energy to the electron e (blue) and is deflected by the angle Θ . The energy of the scattered photon (red) decreases depending on Θ . Figure adapted from [36]

Right: Energies of the scattered photon $E(\Theta)$ and the scattered electron $E_e(\Theta)$ depending on the scattering angle Θ , exemplary illustrated for an initial photon energy of 59.5 keV, e.g. from an Americium (^{241}Am) source.

differential cross-section over the azimuth angle Φ leads to the Θ -differential cross-section, a function depending on Θ , [34]:

$$\sigma_{CS,\Theta}(E_0, \Theta) := \frac{d\sigma_{CS}}{\sin(\Theta)d\Theta} = \pi r_0^2 \epsilon^2 \left(\frac{1}{\epsilon} + \epsilon - \sin^2(\Theta) \right), \quad (1.5)$$

Incoherent Scattering

Classical Compton scattering applies to free electrons only, but electrons in a material are bound to atoms. To correctly describe scatter effects in a material, incoherent scattering has to be considered. This is done by introducing the so called incoherent scattering factor S to correct the differential cross-section for the case of bound electrons. The cross section for incoherent scattering is the product of the differential cross-section for Compton scattering and the correction factor S :

$$\frac{d\sigma_{IS}}{d\Omega} = S(E_0, \Theta) \cdot \frac{d\sigma_{CS}}{d\Omega}, \quad (1.6)$$

where the correction factor depends on the momentum transfer $\Delta p = \sin(\Theta/2)E_0/hc$ between the incident photon and the electron. The value of the correction factor S is material dependent as it corresponds to the number of electrons of an atom that contributes to the scattering cross-section. Based on a fit to experimental data of Hubbell et al. [27], Maier [34] derived the correction factor for Silicon ($Z=14$) according to:

$$S_H(E_0, \Theta) = 14 \cdot \frac{1 + \exp(-0.18(E_0 \sin(\Theta/2))^{0.87})}{1 + 7.19 \cdot \exp(-3.11E_0 \sin(\Theta/2))}, \quad (1.7)$$

with the energy of the incoming photon E_0 . The Θ -differential cross-section for incoherent scattering can be calculated by using the result of equation 1.5:

$$\sigma_{IS,\Theta}(E_0, \Theta) := \frac{d\sigma_{IS}}{\sin(\Theta)d\Theta} = S(E_0, \Theta) \cdot \frac{d\sigma_{CS}}{\sin(\Theta)d\Theta}, \quad (1.8)$$

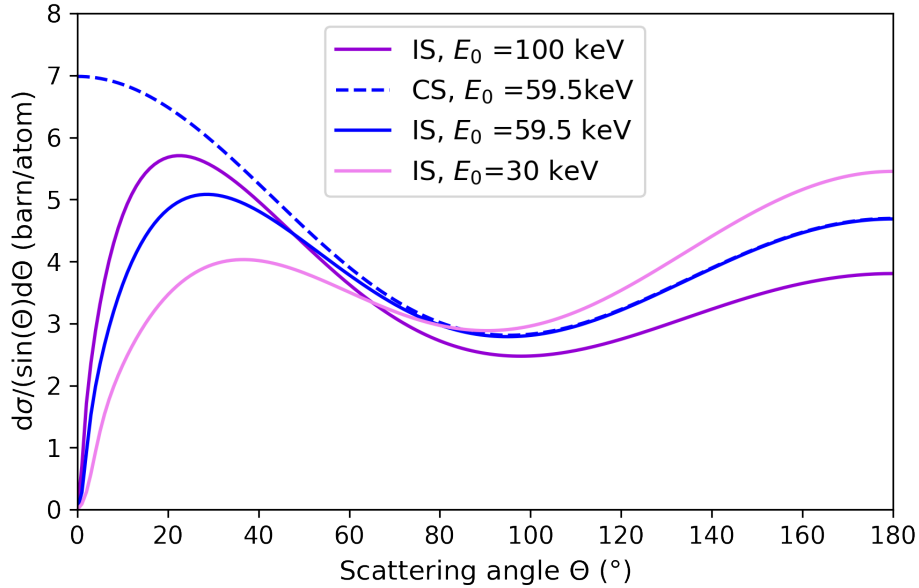


Figure 1.6 Θ -Differential Cross-sections for Incoherent Scattering (IS), in Silicon ($Z=14$), for three different energies. The energies of the incident photon are 30, 59.5 and 100 keV. For comparison, the dashed line illustrates the Θ -differential cross-sections for coherent scattering (CS), exemplary for an initial photon energy of 59.5 keV, e.g. from an Americium (^{241}Am) source. Figure idea taken from [34]

The difference between Compton scattering and incoherent scattering is shown in **Fig: 1.6**, being most pronounced at low energies and small scattering angles. Further, the influence of the energy of the incoming photon on the Θ -differential cross-sections for incoherent scattering is depicted for three energy values. See **Fig: 1.6**

However, it is more common to use the term Compton scattering for both processes, which will also be applied in this work.

1.3.3 Pair Production

The production of an electron and a positron in the vicinity of a nucleus from a high energy photon is called pair production. The energy threshold for the occurrence is $E > 1022$ keV. The vicinity of a nucleus is needed for momentum conservation. The energy range of pair production is out of the X-ray range and therefore irrelevant for this thesis.

1.4 Compton Telescopes

Generally Compton telescopes are gamma-ray detectors which utilize Compton scattering to determine the polarization and the origin of the observed γ -rays. They are usually applied to detect γ -rays in the energy range where Compton scattering is the dominating interaction process. The direction of motion of the scattered photon can be determined

by measuring the position of the initial Compton interaction and the energy deposits of the scattered X-ray. This so called event reconstruction is described in section 1.4.1. A polarization analysis is then conducted on that basis (section 1.4.2). The ComPol telescope (chapter 2) follows the working principle of the COMPTEL type [45], the simplest type of Compton telescope.

1.4.1 Event Reconstruction

The COMPTEL detector system consists of two energy- and position- sensitive detectors arranged in a stacked order, see **Fig: 1.7**.

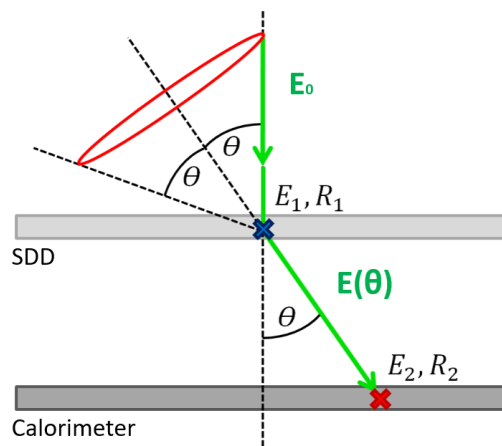


Figure 1.7 Schematic Illustration of a COMPTEL Type Compton Telescope.

An exemplary Compton event is shown. First, a X-ray photon (green) interacts via Compton scattering process in the upper detector. The Energy E_1 is deposited at the position R_1 . Subsequently, the deflected photon is fully absorbed in the lower detector at the position R_2 and deposits the energy E_2 . The origin of the initial photon can be confined to a cone surface (red circle) with an opening angle of 2Θ by detecting the positions and energy deposits. Figure adapted from [36]

A Compton event consists of a coincident event in both detectors. In the first detector the photon undergoes Compton scattering at position R_1 and transfers the energy E_1 to the electron. Afterward, the photon gets completely absorbed in the second detector via photo effect at position R_2 . The energy deposits there is E_2 [36] [45]. This second detector acts as a calorimeter and consists usually of scintillating material. From the Compton formula, equation 1.1, the scattering angle Θ can be calculated from:

$$\cos(\Theta) = 1 - m_e c^2 \left(\frac{1}{E_2} - \frac{1}{E_1 + E_2} \right), \quad (1.9)$$

where the initial photon energy is $E_1 + E_2 = E_0$ and the wavelength shift $\Delta\lambda$ has been expressed in terms of the energy [36]. From the scattering angle the initial direction of the X-ray can be confined to a cone surface with an opening angle of 2Θ . A COMPTEL type Compton telescope cannot resolve the direction of the recoil electron, therefore the initial direction cannot be confined any further. For a more detailed description of the working principle of COMPTEL telescopes, see Zoglauer [45]. To determine the position of an X-ray source precisely, a significant number of Compton events have to be measured and the intersection point of all resulting Compton cones has to be calculated. A so called Compton camera can observe the entire solid angle of 4π . [36]. The position reconstruction is not needed anymore by restricting the observation to one specific direction. To achieve this, the telescope is aligned towards one source and a collimator is added in front of

the detector system [36], which leads to a suppression of the number of Compton events from other directions. During a process called event selection, useful Compton events from Cygnus X-1 are distinguished from background events, see subsection 2.2.5 for a description related to ComPol.

1.4.2 Polarimetry

As mentioned in section 1.4.1, Compton telescopes can also be used to measure the degree of polarization P and the dominant polarization plane of a X-ray source. The cross-sections for coherent scattering and for incoherent scattering are maximal for scattering angles of $\Phi = 90^\circ$ and $\Phi = 270^\circ$. This has been calculated using equations 1.4 and 1.6. A sketch of the polarization dependence is given in **Fig:** 1.8. The calculation and the figure can be interpreted as follows:

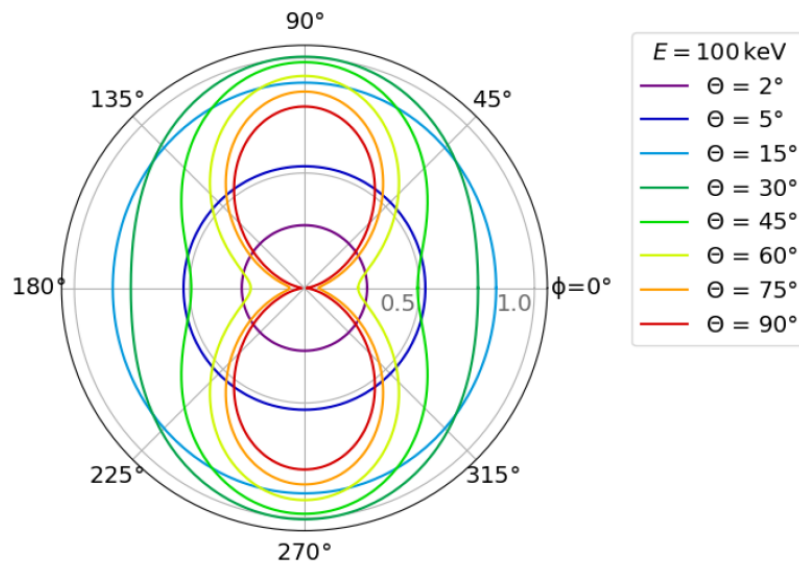


Figure 1.8 Polar Plot of the Differential Cross-section for Incoherent Scattering in Silicon for an Incident Photon with an Energy of 100 keV.

The calculation has been done according to equation 1.6. The colored lines show the dependence of the cross-section on the azimuthal scattering angle Φ for a specific scattering angle Θ . The azimuthal angle Φ is described with respect to the initial polarization vector ξ . The radial distance to the midpoint corresponds to the amplitude in barn/atom. Taken from [36]

- The probability for the photon to be scattered in a direction which is orthogonal to the initial polarization vector is increased.
- As $\sin(2\pi) \sim 0$, the detectable polarization signature is weak for scattering angles close to 0° and 180° .
- The higher the energies, the smaller the scattering angle on average and the weaker the dependence on the polarization.

The probability distribution for the azimuthal scattering angle can be calculated from equation 1.6. The real azimuthal scattering angle Φ in the reference frame of the initial X-ray is not known, therefore an arbitrary new scattering angle Φ toward a fixed reference frame in the detector system is introduced [36]. The probability distribution for this new scatter angle can be expressed by [41]:

$$f_P(\Phi) = C \cdot [1 + a \cdot \cos(2(\Phi - \Psi))] \quad (1.10)$$

The parameter C describes the offset of the azimuthal scattering angle distribution and is related to the total number of events. The modulation amplitude a describes the amplitude of the cosine curve and is calculated by the ratio of the absolute amplitude A and the offset C . The value of a has to lie between 0 and 1. The angle Ψ denotes the polarization angle in the reference frame of the instrument and leads to a shift along the x-axis of the probability distribution. Using equation 1.10 it is possible to calculate the degree of Polarization P by dividing the measured modulation amplitude a by the modulation amplitude for 100% polarized light μ to $P = a/\mu$. The modulation amplitude for 100% polarized light μ depends on the used instrument and has to be determined experimentally via a calibration measurement.

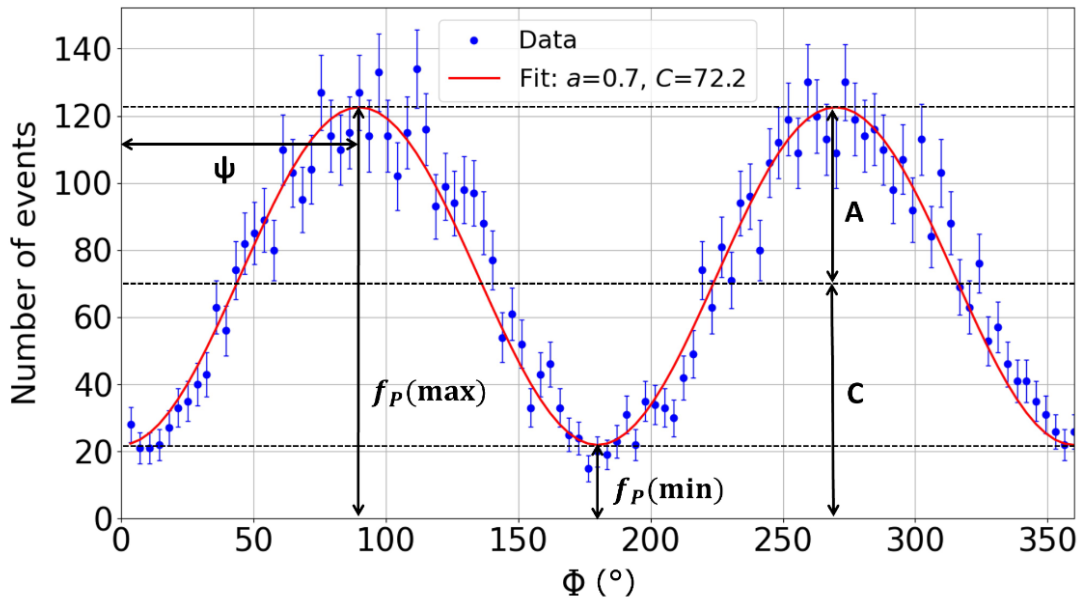


Figure 1.9 Exemplary Data and Fit of the Cosine Modulation of the Azimuthal Scattering Angle Distribution for Polarized Photons.

Illustration of the absolute amplitude A , the offset C , and the polarization angle Ψ in the reference frame of the instrument. The amplitude A is proportional to the degree of polarization. The polarization angle Φ corresponds to the plane of polarization. Taken from [22].

The ComPol Project

As stated in section 1.1, ComPol, is a CubeSat mission to perform a long-term measurement of the black hole binary system Cygnus X-1 in the medium to hard X-ray range. The CubeSat will focus on Cygnus X-1 for up to one year. The components of the instrument are engineered by different research groups, the Technical University Munich (TUM), the Commissariat à l'énergie atomique (CEA) in Paris, the RadLab at the Politecnico di Milano (Polimi), and the Laboratory for Rapid Space Missions (LRSM) in Garching. The latter is funded by the ORIGINS excellence cluster at the TUM. Currently, an adapted instrument is in preparation for an In-Orbit-Verification (IOV) mission on an external platform aboard the International Space Station (ISS), further denoted as ComPol-IOV. The launch will be in the end of 2023. The main goal of the ComPol-IOV is to prove the functionality and durability of the instrument in the space environment of a low earth orbit (LEO). Besides that, it allows for a in-orbit background study and for developing data acquisition routines using real data. The focus of this thesis is the characterization of the Silicon drift detector (SDD) module, the prototype for the ComPol-IOV mission. This Chapter provides an overview of the ComPol project. The ComPol detector system consists of two layers. A Silicon drift detector (SDD), described in section 2.2.1, makes up the first layer and a CeBr₃ scintillator, described in section 2.2.2, the second one. First, an introduction on SDDs in general is given in section 2.1, leading to a description of the SDD Detector for the ComPol and the ComPol-IOV mission in subsection 2.2.1. The LaBr₃ detector substitutes the CeBr₃ for the characterization measurements, performed in this thesis and described in chapter 3. Besides the crystal material, also the readout electronics is different for the two detectors. The CeBr₃ is read out by Silicon Photo multipliers (SiPMS) and the LaBr₃ is read out by a classical Photo-multiplier (PMT). The working principle of PMTs and SiPMS is described in section 2.2.3. An introduction to energy resolution is given in section 2.2.4 and the data analysis chain for ComPol is described in section 2.2.5.

2.1 Silicon Drift Detector (SDD) - in General

The ComPol detector system consists of two layers, an SDD, described in section 2.2.1, makes up the first layer and a CeBr₃ scintillator, described in section 2.2.2, the second one. In this section SDDs are described in general. The SDD is a special type of semiconductor detector which is widely used for X-ray spectroscopy and as particle detectors or trackers. A much higher energy resolution and lower detection threshold can be achieved than by using e.g. scintillation detectors. SDDs have a very small readout anode relative to their sensitive volume, leading to a reduced readout capacitance and thus a low noise level [40], [19]. In the following, the basics of semiconductor detectors and SDDs will be introduced, for more profound information see e.g. [40], [29].

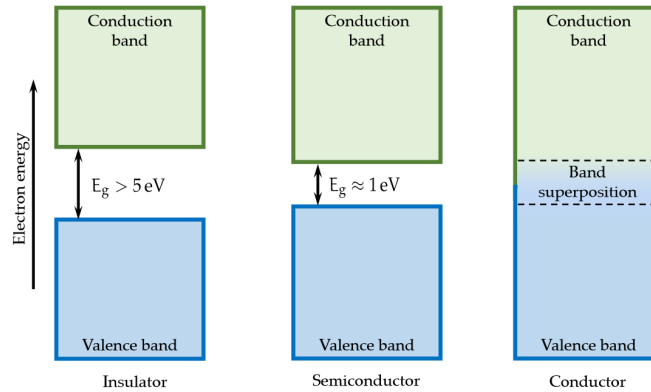
Table 2.1 Properties of the Semiconductor Material Silicon.

The quantity Z denotes the atomic number, ρ the density at $T = 300$ K and ϵ the average energy which is necessary to build an electron-hole pair. E_g is the band gap. The values of ϵ , E_g , and the mobility are given for the typical operating temperature of Silicon ($T = 300$ K). Data taken from [29]

	Z	ρ (g/cm ³)	ϵ (eV)	E_g (eV)	Mobility (cm ² /(V · s))	
					Electrons	Holes
Silicon	14	2.33	3.62	1.106	1350	480

Semi Conductor Detectors

The energy of electrons in a solid is confined to energy bands. The highest, yet occupied band is called valence band, the next higher-lying, non-populated band is called conduction band. In between these bands is a gap which is referred to as band gap (E_g). Its size determines whether the material is called an insulator, a semiconductor, or a conductor [40]. The band structure corresponding to these different types is illustrated in **Fig. 2.1**.

**Figure 2.1 Band Structures of an Insulator, a Semiconductor, and a Conductor.**

Insulators have a relatively large gap between the valence and the conduction band of $E_g > 5$ eV. Semiconductors have a smaller band gap of $E_g \approx 1$ eV. In conductors the valence and conduction bands are superimposed. Taken from [19].

In conductors, the electrons can move easily between the valence and conduction bands via thermal excitation. An insulator has a large band gap thus the electrons from the valence band cannot move into the conduction band. A semiconductor has a smaller band gap. If a valence electron gains sufficient thermal energy it can be elevated into the conduction band. The thermal excitation creates an electron in the conduction band and an associated vacancy (hole) in the valence band, together called electron-hole pair. The current induced by electrons which move to the conduction band increases strongly above a certain temperature. This quantity is called leakage current, which is a source of noise when the semiconductor is used as a radiation detector. Therefore, semiconductor detectors are often operated at low temperatures. The band gap in semiconductor materials can be used for particle detection. If a charged particle or a gamma ray enters the material, valence electrons are excited into the conduction band [19]. In an external electric field, the electrons are collected to the anode and the holes are collected to the cathode. This enables to measure the deposited energy and to use the semiconductor as a detector. The main properties of the semiconductor material Silicon is given in **Tab. 2.1**.

Impurities and Doping

Ideal crystals without any impurities do not exist. The small residual impurities affect the band levels, the band gap and therefore the conductivity. The acceptor impurities provide additional holes and the donor impurities provide additional electrons. If an acceptor atom (e.g. Boron) with three valence electrons is inserted into a four-valent crystal lattice, e.g. Silicon, an additional hole is available, called p-type crystal due to the presence of positive acceptor impurities. If a donor atom with either one (e.g. Lithium) or five valence electrons (e.g. Phosphorus) is inserted into a four-valent crystal lattice, one additional electron is available, called n-type crystal due to the presence of negative donor impurities. In general acceptor as well as donor impurities are present in the crystal lattice. The intentional introduction of impurities into a lattice is called doping. It is used to make to create a p-n transition [29], [40].

Diode and Depletion

A diode is the combination of a p-type and an n-type semiconductor material, see **Fig. 2.2**. At the junction between the materials (the p-n-junction) free electrons diffuse into the p-type region, recombining there with holes. This leads to the so called depletion zone, a space charge region around the junction until the electric field of the space charge compensates the exchange of more electrons. It can be used as the active volume of a semiconductor detector. When energy is deposited in the depletion zone, electron-hole pairs are created. The average energy required to create an electron-hole pair is for Silicon $\epsilon_{si} \approx 3.65 \text{ eV}$. Due to the electric field the charge carriers are separated, they do not recombine but drift instead to the non-depleted regions. There they can be measured as a reverse current.

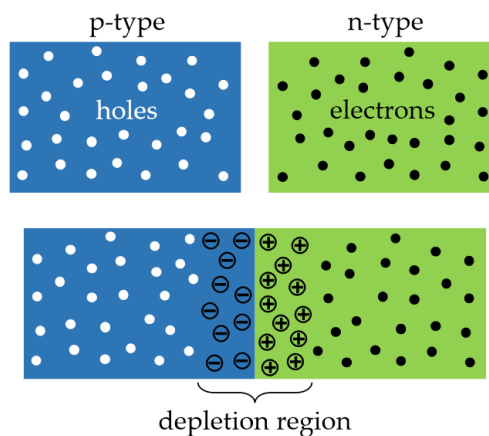


Figure 2.2 Combining p-Type and n-Type Semiconductor Materials to build a Diode.

A depletion zone is created at the junction between the two materials. Taken from [19].

The detector is only sensitive to charge depositions in the depletion zone. This very small region can be extended by applying an electric voltage to the diode. The voltage is applied in a reverse bias configuration, that means the negative terminal is applied to the p-type side and the positive terminal is applied to the n-type side. Thereby, the electrons and holes are attracted to the sides. The size of the depletion region increases with increasing bias voltage and decreasing net impurity concentration. The so called depletion voltage is the voltage, at which the detector obtains full depletion. As soon as a reverse bias voltage is applied, a semiconductor detector behaves as a capacitor with capacitance C_D .

PIN Diodes

PIN (positive, intrinsic, negative) diode detectors use the above mentioned method to deplete a large silicon volume. They consist of a bulk of very pure intrinsic silicon which usually is of n-type with a very low donor density. On the top and bottom surfaces of the bulk, thin layers of p- and n-type silicon with a high acceptor and donor density are added by doping. The bulk can be fully depleted by applying a reverse bias voltage, depending on the thickness and the doping concentration. [19]

Silicon Drift Detector (SDD) [19]

The sideways depletion was introduced by E. Gatti and P. Rehak to produce semiconductor detectors for ionizing particles with a low anode capacitance [11]. This detector type is called Silicon Drift Detector. An SDD adds the principle of sideways depletion to the PIN, an SDD is illustrated in **Fig. 2.3**. A volume of a high-resistivity semiconductor material (n-type Silicon) is covered by rectifying p-doped junctions on the upper and lower surface. The (negative) bias voltage is applied on the entrance window side (back contact) of the detector. The p-junctions on the detector readout side are segmented strip-like (drift rings). They are biased in a way that they generate an electric field with a strong component parallel to the surface. Therefore signal electrons which are released in the depleted volume by the absorption of ionizing radiation, drift towards the readout contact, the collecting anode. The anode has small physical dimensions, therefore the detector has a small capacitance, independent of the detector area. The small capacitance allows for low electronic noise and high rate operation of the SDD. Furthermore, SDDs have fast and efficient charge collection properties. To get the ultimate noise performance a junction field-effect transistor (JFET) is integrated directly into the anode structure of the chip. Therefore the readout electronics can be placed at a distance of several cm to the detector chip and the anode capacitance is still only 180 fF, leading to an excellent signal-to-noise ratio. An inner guard ring (IGR) shields the n-JFET from the silicon bulk.

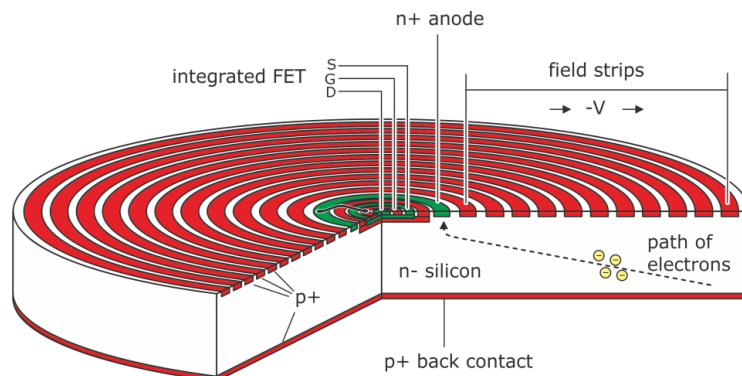


Figure 2.3 Schematic Sketch of a Silicon Drift Detector.

An electric field guides the electrons to the collecting n+ anode in the center of the detector. The latter is surrounded by several drift rings. The entrance window for radiation is on the opposite side (p+ back contact). The illustrated detector has an integrated field-effect transistor (FET) close to the anode. The FET forms the first part of the signal readout chain. In contrast, the SDDs in the ComPol project don't have a FET. The dashed line shows the drift path of electrons to the anode. Figure taken from [32].

The TRISTAN Detector

The so-called TRISTAN detector is a new detector system which is currently under development.[19] Its aim is the search for sterile neutrinos on the keV mass scale with the Karlsruhe Tritium Neutrino (KATRIN) experiment. The beta decay spectrum of tri-

tium will be measured in total, to search for a kink-like distortion. To achieve this, an excellent energy resolution is required. The detectors has the following advantages:

- Possibility to handle high count rates (100 kcps/pixel)
- Excellent energy resolution (300 eV FWHM at 20 keV; 140 eV FWHM at 5.9 keV)
- Availability of an integrated signal readout stage.

The SDD concept is very flexible in shape and size. The pixels are 450 μm -thick hexagonal cells arranged in a honeycomb structure. The detector entrance window has a minimal thickness of about 50 nm to minimize the dead area and associated energy losses. Each detector pixel has 20 hexagonal drift rings which are biased via a voltage divider of 5 M Ω total resistance.

Following the above mentioned advantages, the SDD technology is predestined for the ComPol experiment. For an efficient background exclusion it is required to accurately measure the energy deposition during Compton scattering.[36]. Another advantage of this detector type is the small atomic number Z of Silicon ($Z= 14$). As shown in section 1.3.2, the cross-section for Compton scattering does not depend on Z , but the cross-section for photoelectric absorption does as it scales with Z^5 , see section 1.3.1. For a successful event reconstruction it is necessary to have a Compton scattering with subsequent photoelectric absorption of the photon. If the number of photons absorbed in the first detector layer are reduced, the number of Compton events in the first detector layer increases.

2.2 ComPol

ComPol, as mentioned above, is the planned CubeSat mission that carries a Compton telescope of the COMPTEL type, see chapter 1, working as a spectrometer and polarimeter simultaneously, covering the energy range of 20 keV to 2 MeV and 20 keV to minimal 300 keV, respectively. Therefore it will be able to close the energy gap between ~ 180 and 300 keV. So far the following four key studies were performed:

- A first feasibility study (ODY SSEUS Space Inc., 2018) [35]
- A first sensitivity study (Matthias Meier, 2019) [36]
- A background, activation and shielding study (Cynthia Glas, 2022) [22]
- A mechanical design and shielding study against optical photons for the IOV mission (Katrin Geigenberger, 2022) [21]

The ComPol CubeSat will consist of 3 CubeSat Units. The standardized size of one unit is 10x10x11.35 cm^3 and the maximum weight is 1.3 kg [9]. That would lead to a size of 10x10x34 cm^3 and a weight of 3.9 kg for ComPol. Due to the strong limitation in size and weight, most of the heavy shielding material must be omitted, making the satellite sensible to cosmic radiation, and dust particles. They relatively quickly degrade the electronics and shorten the lifetime of the satellite. A typical lifetime in orbit for a CubeSat is estimated to 1 year. The detector system for the ComPol consists of a Silicon Drift Detector, described above in section 2.1, where Compton scattering takes place (see subsection 1.3.2). After this first detector, the scattered photons are absorbed in a CeBr_3 scintillator, operating as a calorimeter. A schematic sketch of the setup with an exemplary Compton interaction is shown in **Fig. 2.4**. [36] The most important characteristics of the SDD and the scintillator for the ComPol project are summarized in the following subsections.

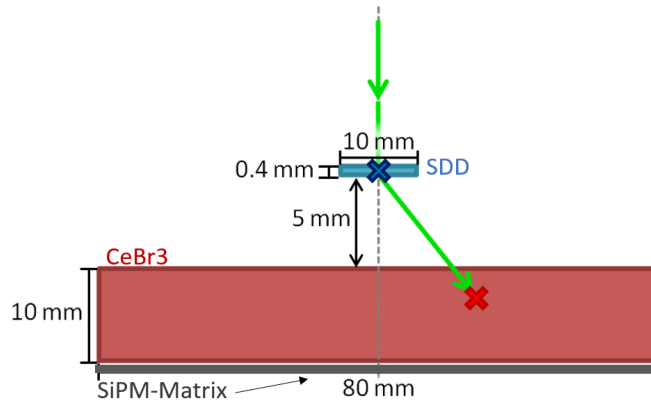


Figure 2.4 Detector Setup of the ComPol CubeSat.

The SDD from the TRISTAN project is illustrated in blue and the CeBr_3 scintillator in red. The base of both detectors is approximately quadratic. An exemplary X-ray event (green) is shown. The incident photon undergoes Compton scattering in the SDD (blue cross) and a subsequent photoelectric absorption in the CeBr_3 scintillator (red cross). Figure adapted from [36]

2.2.1 SDD-Detector Modul for ComPol

The SDD module for the ComPol mission will be build of several hexagonal pixels. The SDD were originally developed for the TRISTAN project of the KATRIN experiment, as introduced in section 2.1. The preliminary module design consists of 31 pixels. Each pixel has a size of 2 mm. The overall dimensions of the module are $10 \times 12.7 \text{ mm}^2$, the height is 0.45 mm, illustrated in the left part of **Fig. 2.5**. In the ComPol-IOV mission two smaller 7-pixel TRISTAN SDDs will be used, shown in the right part of **Fig. 2.5**. For an efficient background rejection, the energy deposition during the Compton scattering event has to be measured as accurately as possible. The energy resolution of the SDD is determined by the Fano noise and the noise originating from the detector electronics and the readout chain, see section 2.2.4 [38], [14].

2.2.2 CeBr_3 -Detector for ComPol

The material chosen for the calorimeter is Cerium(III)Bromide (CeBr_3), which is a scintillating crystal. Scintillation light is created by ionizing radiation interacting in the detector volume. The wavelength of maximum emission thereby is at 380 nm [25]. The read out of the scintillation light will done by a matrix of 64 Silicon Photomultipliers (SiPM), briefly introduced in the following subsection. The measured scintillation light distribution depends on the position of the interaction and the energy of an incoming photon in the detector. The readout system to reconstruct the interaction point is based on an artificial neural network. After training the latter with data from simulations, the interaction point can be determined with an accuracy in the order of a few millimeter. The development has been done at Université Paris-Saclay [23]. Furthermore, CeBr_3 has a good absorption efficiency for X-rays and a position resolution of the same order of magnitude as the first detector layer. The CeBr_3 module has a size of $80 \times 80 \times 10 \text{ mm}^3$. The spatial resolution of the CeBr_3 detector is limited to 2.5 mm parallel to the detector plane and 2.2 mm in the vertical dimension (height of the detector). The lower energy threshold of the calorimeter is 10 keV and the overall energy resolution can be calculated on the basis of measurements with various radioactive sources, see[23] and subsection 2.2.4.

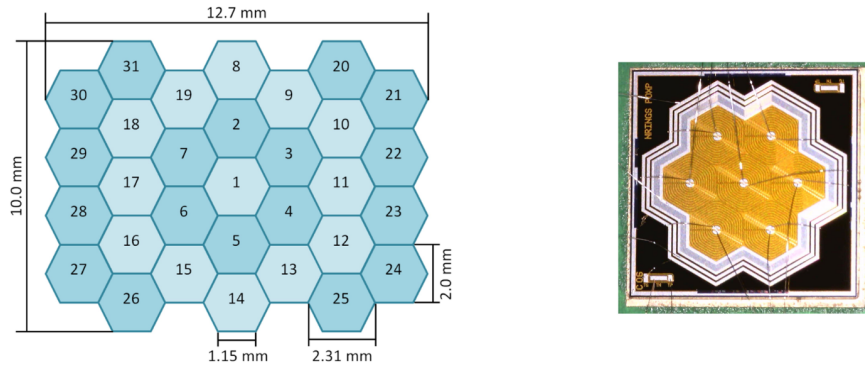


Figure 2.5 Module Design and Prototype of the Silicon Drift Detector.

Left: The SDD module for the ComPol mission consists of 31 hexagonal pixels with a size of 2mm.

Right: The seven pixel prototype SDD (originally developed for TRISTAN). It will be used in the ComPol-IOV mission. In the center of each pixel is an anode. It is surrounded by the drift rings. The dimensions of the pixels are the same as in the sketch on the left. Two bonding wires are attached to each pixel, one for the anode and one for the innermost drift ring. The outermost drift rings are connected such that individual bonding wires for each pixel are not required [36]. Figure taken from [22]

2.2.3 Photomultipliers

A Photo-multiplier (short for Photo-multiplier tube (PMT)) is an extremely sensitive detector, making it possible to detect radiation in the wavelength-range from ultraviolet to near-infrared of the electromagnetic spectrum [18]. Even a single photon detection is possible. More specifically, a PMT is a vacuum phototube, an evacuated glass housing which contains a photocathode, several so called dynodes, and an anode. Incident photons hit the photocathode material, subsequently electrons are ejected from the surface as a consequence of the photoelectric effect. The electrons are directed by the focusing electrode toward the electron multiplier. The electron multiplier consists of a number of electrodes, the dynodes. The gain factor grows exponentially with the number of dynodes. Typical multipliers have about $n = 10$ dynodes. If 4 electrons are ejected from each dynode for each impinging electron, the number of electrons (i.e. the current) is increased by a factor of $4^{10} \sim 10^6$.

Silicon Photomultipliers (SiPM) are photomultipliers based on semiconductor technique, being used for applications where low radiation levels must be measured and quantified with high precision [8]. They are small, need only low voltages and are mechanically robust compared to PMTs, which is important for the application in a CubeSat. Every SiPM consists of a vast number of photo-sensitive micro-cells. Each micro-cell includes one photo-diode operating in Geiger mode and is coupled with the others by a metal or polysilicon quenching resistor. It is possible to generate signals with a dynamic range from a single photon to 1000 photons for a device with an area of 1mm^2 only. An introduction to SiPMs can be found in [8].

2.2.4 Detector Resolution

The energy resolution is an important property of detector systems, see e.g. [40]. It is relevant for the ComPol mission as well as for the measurements performed during this thesis. The energy resolution describes how precise the energy deposit of a particle interaction in the detector can be measured. The most important contributions to the energy resolution are the **Fano noise**, the **series noise** and the **shot noise**. The effects of series

noise and shot noise are often combined to a so called **electronics noise**.

The **Fano noise** describes the statistical fluctuation of the number of electron hole pairs created in the detector per unit energy deposit in the volume.

The **series noise** describes the effect that the pre-amplifier can only measure the tiny charge of an event with limited precision. The series noise scales with the anode capacitance. It dominates the fluctuations on the waveform on short timescales.

The **shot noise** describes the effect that the leakage current in the detector diode adds a random number of electrons to the charge cloud. It dominates fluctuations on the signal waveform on large timescales.

There is an optimal timescale on which the detector pulses should be evaluated in order to obtain the best energy resolution. The so called noise curve is illustrated in **Fig: 2.6**. The electronic noise can be reduced by the detector design, for example by lowering the anode capacitance which leads to less series noise. Lowering the leakage current by cooling leads to less shot noise. However, the Fano noise sets a fundamental limit which can be achieved with a silicon detector. This limit can only be overcome by changing the detector material or physical detection mechanism e.g. in microcalorimeters. For silicon semiconductor detectors the fundamental limit lies at 120 eV FWHM for energies of 5.9 keV,[19].

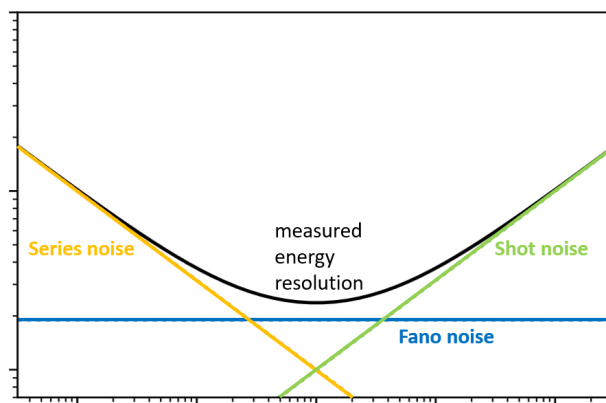


Figure 2.6 Energy Resolution depending on the Shaping Time.

The Fano noise, the series noise and the shot noise contribute to the measured energy resolution. Only the Fano noise does not depend on the shaping time. Adapted from [40].

The energy resolution of both detectors depends on the energy. That of the SDD is dominated by the Fano noise:

$$\sigma_{Fano} = \sqrt{F \cdot \omega \cdot E}, \quad (2.1)$$

where F is the Fano factor and ω is the energy necessary to create an electron hole pair in Silicon. Both factors are temperature dependent. The relevant temperature is expected to be between -20° and $+20^\circ$ [36], [33]. Therefore the Fano factor is $F \sim 0.17$ and the energy to create an electron hole pair $\omega \sim 3.64$ eV, determined in [38]. The noise contributions of the detector electronics ($\sigma_{el} \sim 60$ eV) and the readout chain are small compared to the Fano noise [14]. The total energy resolution of the SDD can be calculated to:

$$\sigma_{E,SDD} = \sqrt{F \cdot \omega \cdot E + \sigma_{el}^2}, \quad (2.2)$$

The comparison between the Fano limit and the total energy resolution of the SDD is illustrated in **Fig 2.7**. These values, calculated by using equations 2.1 and 2.2 are used

for the simulations carried out in this thesis. The values for a calorimeter consisting of Lanthanum(III)Bromid (LaBr_3) are taken from measurements by Gostojić [23]. The values of the resolution of the calorimeters were determined by measuring Full Width at Half Maximum (FWHM) of several X-ray and γ -ray lines for various radioactive sources, see [23]. An interpolation of the values for LaBr_3 is presented in **Fig:2.8**. Also the energy resolution of the CeBr_3 calorimeter was measured by Gostojić, see [23]. The energy limits, for the measurements with ComPol are $E_{min,SDD}=2$ keV for the SDD and $E_{min,CeBr_3}=10$ keV, see M.Meier [36] for more information.

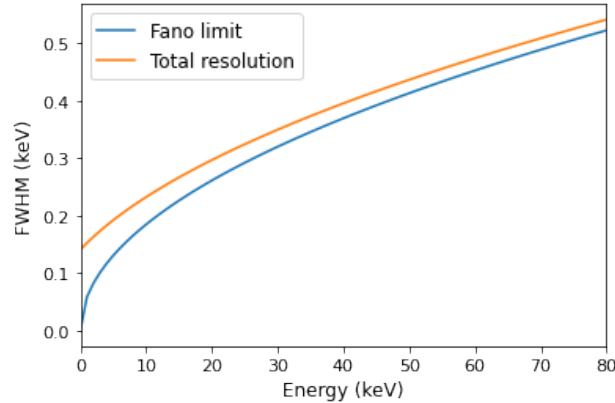


Figure 2.7 Energy Resolutions of the SDD

Comparison of the total energy resolution of the SDD and the resolution from the Fano limit only, calculated by using equations 2.1 and 2.2. These values are used for the simulations carried out in this thesis.

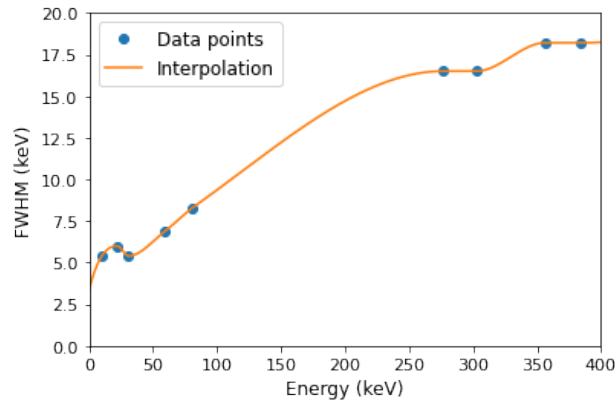


Figure 2.8 Energy Resolutions of the LaBr_3 Calorimeter.

Illustration of the energy resolution of the LaBr_3 calorimeter, measured for discrete energies by Gostojić [23] and interpolated between the data points. These values are used for the simulations carried out in this thesis.

2.2.5 Data Analysis for ComPol

To achieve the scientific goal, gaining more information about the degree and plane of polarization of the X-rays from Cygnus X-1 presented in section 1.2, the rate of background events has to be suppressed compared to the rate of signal Compton events from the astrophysical source as efficiently as possible, see [36]. This background reduction is done by external shielding, as described in [22] and via a selection process, implemented in

python. Afterwards the polarization analysis is performed followed by the determination of the sensitivity.

Event Selection

Only events which undergo Compton scattering in the SDD with subsequent complete absorption of the scattered X-ray in the calorimeter are considered for the polarimetry analysis. The majority of all events have to be identified as background events and rejected. In the event selection process background events are selected in several steps. For details see [36], [22]:

- **Coincidence Cut:** Only events with interactions in both detectors at the same time will be taken into account.
- **Energy Cut:** Only the energy range of interest is considered. The sum of energies, deposited in both detectors < 300 keV. The probability for Compton scattering is the highest for energies between 20 keV and 300 keV. The low energy threshold for acceptance is defined by the detector thresholds and set to 11 keV.
- **Selection of Compton Events:** For the selection two different methods of calculating the scattering angle Θ are used. A geometrical calculation of Θ is done, with the knowledge of the interaction points, R_1 , R_2 in the SDD and in the calorimeter in **Fig. 1.7**, and the geometric assembly and orientation towards the source. Additionally, the cosine of the scattering angle can be determined using the Compton formula, equation 1.9 and the detected energy deposit in both detectors. If the event is a useful Compton event, both obtained scattering angles are equal.
- **Selection of Events with large Scattering Angle:** The modulation of the distribution of the azimuthal scattering angle Φ is strongest for large Compton scattering angles Θ (see equation 1.4). Therefore, another cut on the scattering angle is applied, to define the lower limit of the acceptance range, depending on the geometries of the detector system.

All events, which pass the event selection, undergo the polarization analysis afterwards.

Polarization Analysis

The cosine modulation of the azimuthal scattering angle Φ is plotted and fitted with equation 1.10 according to subsection 1.4.2 (Polarimetry). The Polarization determination and analysis is not relevant for this thesis. For further details concerning the background simulations see M.Meier[36], C.Glas[22].

Sensitivity

The sensitivity of the ComPol telescope can be estimated with the knowledge obtained from the simulation of signal and background events and the event selection and polarization analysis afterwards [36],[22]. The estimation on the sensitivity of the instruments is usually performed by the determination of the Signal to Noise Ratio (SNR), the ratio of the signal rate (R_S) to the background rate (R_{BG}): $SNR = R_S/R_{BG}$

To estimate the sensitivity on the degree of polarization for the instrument, the so called Minimum Detectable Polarization (MDP) is used, describing the polarization sensitivity to a 99 % confidence level [42]:

$$MDP = \frac{4.29}{\mu \cdot R_S} \left(\frac{R_S + R_{BG}}{T} \right)^{1/2}, \quad (2.3)$$

where T is the observation time and μ is the modulation amplitude for 100 % polarized light, introduced in section 1.4.2.

Characterization of the Prototype SDD Modul

In the previous chapters the Compton ComPol-Mission, which will investigate the spectrum and polarization of the black hole binary system Cygnus X-1 over the duration of at least one year in the hard X-ray range (20 keV - 2 MeV) was introduced and theoretical and technical foundations were laid. The latter include e.g. the working principle of Compton telescope and polarization measurements in section 1.4, the process of Compton scattering in section 1.3.2, a brief introduction to Silicon drift detectors in general in section 2.1 and a description of the SDD detector for the ComPol and the ComPol-IOV mission in section 2.2.1. The calorimeter (CeBr_3) was presented in section 2.2.2. As stated above, the aim of ComPol-IOV is to prove the functionality and durability of the instrument in the space environment of a low earth orbit (LEO) and to measure in-orbit background fluxes and develop data acquisition routines for the final CubeSat mission.

The aim of this thesis is the characterization of the seven pixel SDD modul, the prototype for the ComPol-IOV mission. The procedure of the characterization and the results will be described in detail in this chapter, starting with the motivation of the characterization measurements in section 3.1. After that follows a detailed description of the setup in section 3.2. The performed characterization measurements are presented in section 3.5. The simulations of the measurement setup carried out with Geant4 are described in section 3.6. Finally, the results from the measurements and from simulations are discussed in section 3.7.

3.1 Scientific Motivation

The physical motivation for the characterization measurements is to reproduce the angle dependent Θ -differential cross-section for incoherent scattering according to the modified Klein-Nishina equation (see section 1.3.2, equation 1.8) by a Compton scattering experiment. Thereby the used setup consists of the SDD module, originally designed for the TRISTAN experiment, as scatter target and a commercially available Lanthanum(III) Bromide detector as calorimeter. The CeBr_3 detector will be characterized separately.

3.2 Experimental Setup

The procedure used to characterize the SDD, which will be described in detail in the following, can be simplified as follows:

A radioactive isotope source, in this case Americium (^{241}Am), decays by emitting pho-

tons with an initial energy of $E_0=59.5$ keV. The photon undergoes Compton scattering in the SDD. Some of the initial energy of the photon is transferred to an electron in the SDD. The energy of the electron $E_e(\Theta)$ is measured in the SDD. The scattered photon is deflected by an angle Θ , depending on the remaining energy. Subsequently, this scattered photon with the energy $E(\Theta)$ is completely absorbed in the calorimeter (the LaBr_3 scintillator) and measured there. The proceeding described above is very similar to that described in section 2.2 and **Fig:** 2.4, the difference lies only in the different calorimeter and in the exactly known photon energy resulting from the Americium source. For the illustration of the Compton scattering process and the energies of participants on the scattering process depending on the scattering angle, see section 1.3.2 and **Fig:** 1.5. In addition to the energies, the timestamps (describing the begin of a signal) of the events in both detectors are recorded. Only events which occur in a certain time-window in both detectors are considered for the determination of the rate (coincidence cut). The rates in dependence of the scattering angle, determined experimentally, are proportional to the incoherent Klein-Nishina cross-section, therefore, an appropriate fit can be performed. The aim of the characterization is to get a good agreement between the measured rates and the theory in a largest possible angular scattering range. The angular dependence of the Compton scattering is experimentally performed by changing the angle between the beam axis of the radioactive source and the calorimeter (the LaBr_3 Detector), which lies on a rotatable part (U-profile) with a pivot point below the center of the SDD. Note, that the term 'angle' is also used for simplicity in the following, describing the angle between the beam axis of the radioactive source and the position of the LaBr_3 scintillator.

In the following the experimental setup and its components are described in detail. The setup is illustrated schematically in **Fig:** 3.2, a photograph of the setup is shown in **Fig:** 3.3 The **prototype SDD module** used for characterization consists of seven hexagonal pixels, as described in section 2.2.1. A photograph is shown in the left part of **Fig:** 3.1. The SDD module is mounted on a printed circuit board (PCB) and assembled in a dark-box. The latter shields the detector from ambient light and thus reduces the leakage current during operation.

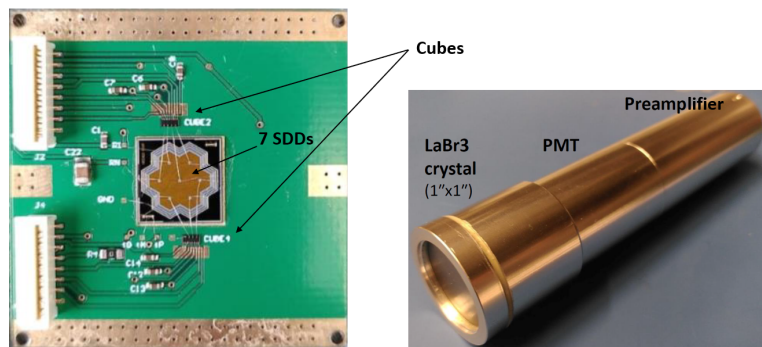


Figure 3.1 Prototype SDD Modul and the LaBr_3 Scintillator

The photographs were done by Matthias Meier.

Left: The Prototype SDD modul consists of seven hexagonal pixels. It is mounted on a printed circuit board (PCB). The signals coming from the seven SDDs go into the cubes. They are pre-amplifiers near the SDDs which translate the collected charge into a voltage ramp. The reset is done by a signal from the SFERA-board when the saturation voltage is reached.

Right: The LaBr_3 scintillator consists of a pre-amplifier, a PMT and a LaBr_3 crystal with a diameter and a thickness of one inch, covered by a thin Beryllium entrance window.

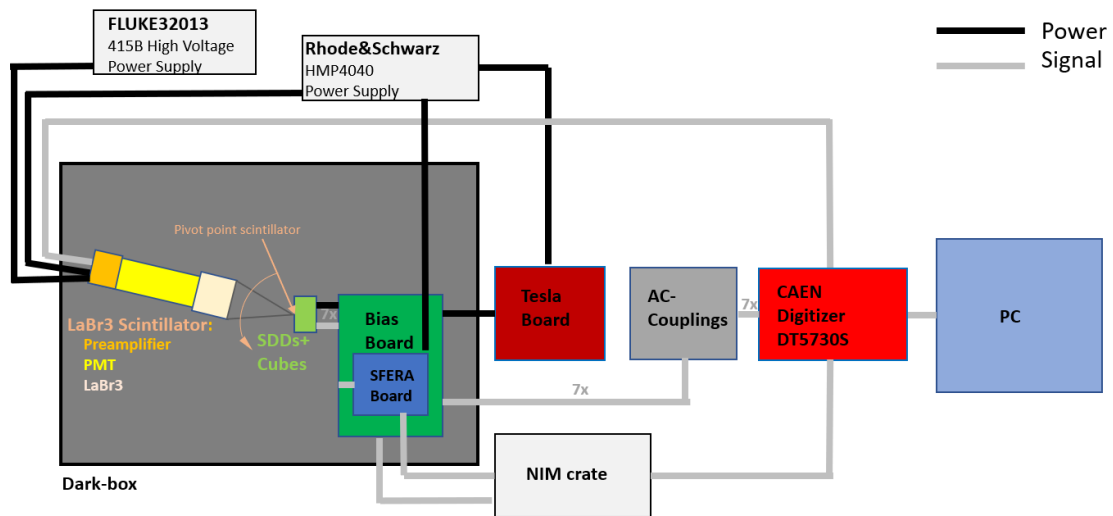


Figure 3.2 Schematic Sketch of the Setup (Top view, not to scale).

The sketch shows the setup used for the characterization measurements, without the placement of the radioactive source and the source itself. The connections to provide power are indicated as black lines, that of the signal connections as grey lines. The **LaBr₃ scintillator** consists of a **pre-amplifier**, a **PMT** and a **LaBr₃ crystal** with a diameter and a thickness of one inch, covered by a thin Beryllium entrance window. The prototype **SDD module** consists of seven hexagonal pixels, mounted on a printed circuit board (PCB). The signals coming from the seven SDDs go into the **cubes**, which are pre-amplifiers near the SDDs translating the collected charge into a voltage ramp. The reset is done by a signal from the **SFERA-board** when the saturation voltage is reached. The **SDDs** are connected to the **Bias board**, which in turn is connected to the **Tesla board**. The both together generate the voltages for the SDDs, which are needed for depletion and generating the drift fields. The **NIM crate** handles the reset and veto signal, the latter to avoid triggering on the reset. The **AC coupling** between SDDs and the CAEN digitizer consists of capacitors transforming the step like voltage ramps to short pulses, comparable to a differentiation. Finally, the data are digitized with the **CAEN DT5730S digitizer**, which is connected to a personal computer (PC). The **dark-box** shields the detectors and components from ambient light.

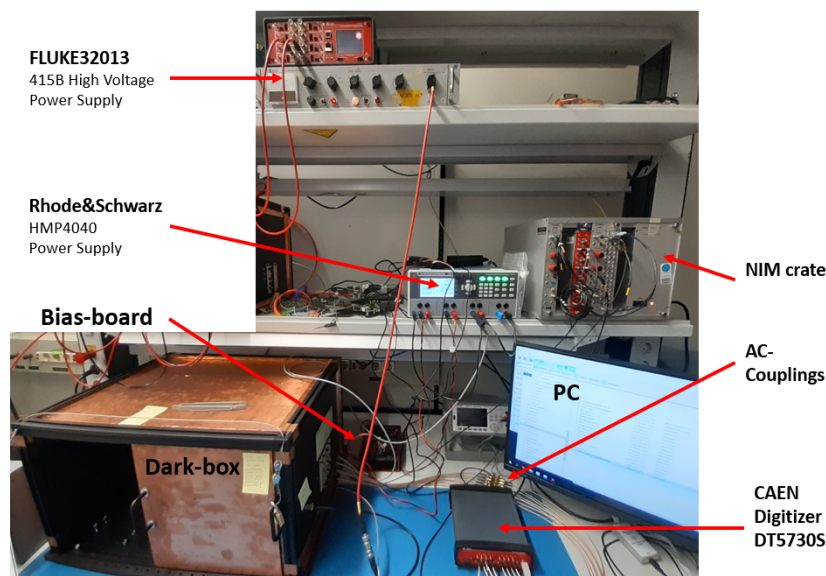


Figure 3.3 Photograph of the Setup.

Especially the power supply of the components are shown. Also the NIM crate, the Bias-board, the AC coupling between SDDs and the CAEN digitizer and the CAEN DT5730S digitizer itself are presented. For description see text and **Fig:3.2**.

First the power supply of the components will be described, followed by a description of the components themselves and the signal processing and, finally the data acquisition.

Power supply of the components, connections depicted as black lines in Fig: 3.2:

The **SDD pixels** are connected to the **Bias board**, which in turn is connected to the **Tesla board**. The **Tesla board** is powered by a conventional power supply (Rhode & Schwarz HMP4040) which provides a supply voltage of 24 V. The latter is transferred to ± 8 V on the Tesla board and after that to ± 5 V and 2 V on the Bias board which then serve as supply voltages for the cubes. Furthermore, the Tesla-board provides the medium (-30 V) and high (-110 V) voltages for the SDDs themselves (required for depletion and generating the drift fields), likewise using the Bias-board, which generates the voltages for the SDDs from the rough adjustment of the voltage in the Tesla-board. The -30 Volt are transferred to -27.2 V, the voltage for the innermost drift-ring (R1). The -110 Volt are transferred to -89.5 V, the voltage for the outermost drift-ring (Rx) and -82.2 V for the back-contact (R_C). On the SDD-board in addition the voltage for the back-frame-potential is created. Concerning the components of the **LaBr₃ scintillator**, the PMT is powered by the FLUKE32013 415B High Voltage Power Supply and the pre-amplifier by the conventional power supply Rhode & Schwarz HMP4040. The **SFERA board** is also powered by the Rhode & Schwarz HMP4040 (6 Volt), whereas the **NIM crate** has its own power supply.

Components and signal processing (grey lines) in Fig: 3.2:

The **LaBr₃ scintillator** consists of a **pre-amplifier**, a **PMT** and a **LaBr₃ crystal** with a diameter and a thickness of one inch, covered by a thin Beryllium entrance window, illustrated in the right part of **Fig: 3.1**. The light signal from an event transformed into an electric signal by the PMT (description see section 2.2.3) is further pre-amplified in the pre-amplifier and then goes directly into the **CAEN Digitizer**. The cables are visualized by grey lines. The signals coming from the seven SDDs go into the **cubes**, which are illustrated in the left part of **Fig: 3.1**. They are pre-amplifiers near the SDDs which translate the collected charge into a voltage ramp. The reset is done by a signal from the **SFERA-board** when the saturation voltage is reached (see the left part of **Fig: 3.4**). To avoid a triggering on the reset, the reset signal (a rectangle signal) coming from the **SFERA-board** is redirected via the **NIM crate** and divided up into two parts, one signal goes back into the cubes for the reset. The signal length of the second signal is extended (extended rectangle signal), leading to a larger time window. This signal is used as a veto for the reset in the CAEN Digitizer. An **AC coupling** between SDDs and the CAEN digitizer which consists of capacitors transforming the step like voltage ramps to short pulses, comparable to a differentiation (see the right part of **Fig: 3.4**). Finally, the data is digitized with the **CAEN DT5730S digitizer**, a state-of-the-art data acquisition (DAQ) system which is connected to a personal computer (PC). The DAQ is presented in more detail in subsection 3.2.1.

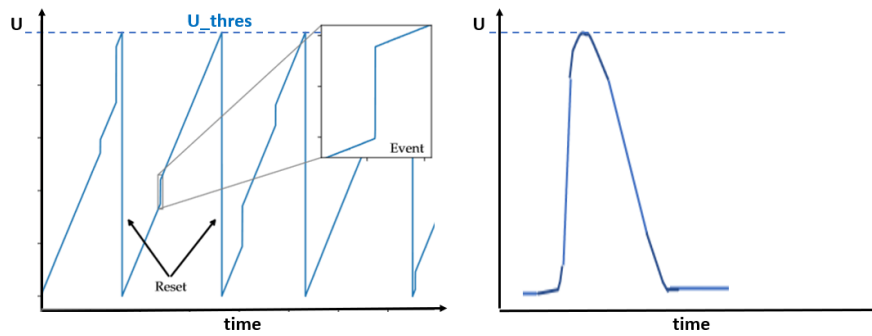


Figure 3.4 Signal Processing in the Cubes and the AC-Coupling.

Left: The signals coming from the seven SDDs go into the cubes. They are pre-amplifiers near the SDDs which translate the collected charge into a voltage ramp. An event occurring in the detector volume is visible as a step-like voltage increase, shown in the small window. The cubes are reset by a signal from the SFERA-board when the saturation voltage is reached (U_{thres}).

Right: The AC coupling between SDDs and the CAEN digitizer are capacitors transforming the step like voltage ramps to short pulses, comparable to a differentiation.

3.2.1 The CAEN Digitizer and the used Firmware

In the scope of this thesis data will be acquired with a CAEN DT5730S digitizer, an 8-channel 14-bit digitizer capable of recording waveforms with a sampling frequency of 500 MS/s, illustrated in **Fig: 3.5**. Furthermore, it features a Digital Pulse Processor (DPP), which allows for Pulse Height Analysis (DPP-PHA) and Pulse Shape Discrimination (DPP-PSD). The CAEN Firmware used in the characterization measurements, is the so called DPP-PSD Firmware which provides charge integration and γ -N discrimination. For a detailed description see the CoPASS User Manual [5]. The configuration of the field-programmable gate array (FPGA) board inside the digitizer and the acquisition can be completely managed by the CAEN CoPASS Software. It allows the user to set the parameters for the acquisition, to configure the boards and to perform the data readout. Furthermore, it allows to save and plot the energy and spectra.



Figure 3.5 Photograph of the Data Acquisition System (DAQ).

The CAEN DT5730S, an 8-channel 14-bit digitizer with a sampling rate of 500 MS/s.

There are two different data acquisition modes, the waveform mode and the list mode which will be described in more detail in the following:

In the **Waveform mode**, the timestamp and full waveform of every single event is recorded. The algorithm detects an event as soon as one of its samples exceeds a predefined threshold. This acquisition mode provides the most information on the events, but storing all waveforms requires a large amount of disk space.

In the **List mode**, only the timestamp and the not yet calibrated energy of every event is stored. Therefore it is crucial that the parameters of the energy estimation filter are set properly in the acquisition software. The advantage of the list mode compared to a full waveform digitization is a reduction of the required disk space. This mode is used during the characterization measurements. The output are several root files which are evaluated by python programs.

The output signals of the detectors are analog voltages. When a signal is read out by the CAEN, the analog voltage is digitized by the analog to digital converter (ADC). The PSD firmware integrates over the signal pulse, which corresponds to the charge. Thus, an ADC bin corresponds to a certain amount of charge. The resolution of the ADC defines the amount of bins available for the digital output values. Each bin corresponds to a certain level and is represented as least significant bit (lsb). The conversion from the ADC values into physical energy values in eV is done in a calibration process, using the spectrum of a well known radioactive source (with distinct line positions). This will be described in subsection 3.5.1, the ^{241}Am sources used for the calibration during the Compton scattering experiments are described in section 3.3.

3.2.2 Experimental Reproduction of the Scattering Angles

As stated above, the angular dependence of the Compton scattering is experimentally performed by changing the angle between the beam axis of the radioactive source and the LaBr_3 detector, which lies on a rotatable part (U-profile) with a pivot point below the center of the SDDs. The pivot point is also shown in **Fig:** 3.2 and further, the rotation possibility of the LaBr_3 Detector is sketched. The dark-box as detail of the schematic sketch is presented in the left part and a photograph of a look inside is presented in the right part of **Fig:** 3.6. The blue arrow and the eye in the left part represents the direction of the view for the photograph, which is presented in the right part of the figure. The LaBr_3 , lying on an U-profile, which is joint to the pivot-point for rotation and further, the SDDs on the PCB are depicted. The scattering angle of the Compton scattering process is experimentally performed by changing the angle between the beam axis of the radioactive source and the LaBr_3 detector. The scattering angles can be reproduced through screws in the grid of the dark-box. The U-profile touches the screw on its backside in direction of view. Each scattering angle is represented by a screw in the dark-box, shown in the lower picture.

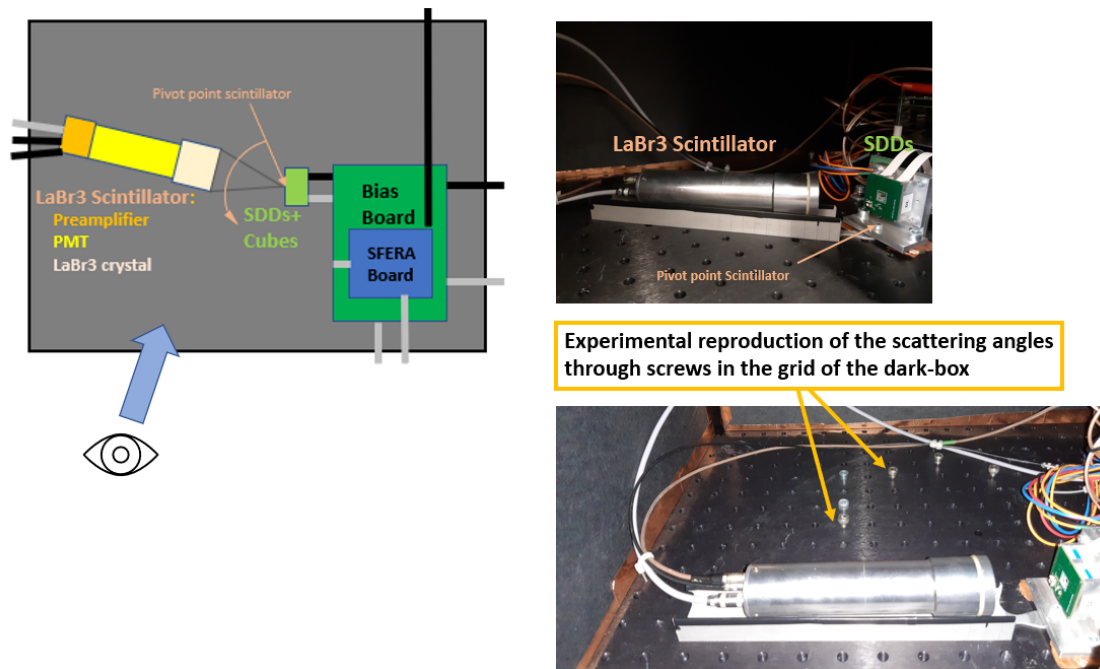


Figure 3.6 Sketch of the Dark-box (Top view) and Photograph of the Look inside the Dark-box.

Left: The dark-box as detail of the schematic sketch is illustrated. The blue arrow and the eye represents the direction of the photograph.

Right: The photographs present the view into the dark-box in direction of the blue arrow, shown in the left part of the figure. The LaBr_3 , lying on an U-profile, which is joint to the pivot-point for rotation and further, the SDDs on the PCB are depicted. The scattering angle of the Compton scattering process is experimentally performed by changing the angle between the beam axis of the radioactive source and the LaBr_3 detector. The scattering angles can be reproduced through screws in the grid of the dark-box. The U-profile touches the screw on its backside in direction of view. Each scattering angle is represented by a screw in the dark-box, shown in the lower picture.

The value of the angles, represented by the screws in the grid were determined geometrically by using the program *GeoGebra*, which is available for free in the web (see [7]). *GeoGebra* is a dynamic geometry software (DGS). It not only provides the usual geomet-

ric, but also an algebraic interface to the geometric objects. The latter can not only be drawn, but also changed by specifying or modifying equations. Therefore, by changing e.g. the position (the coordinates) of one screw, the new value of the angle is calculated and displayed immediately. The software was originally developed by Markus Hohenwarter as part of his diploma and doctoral thesis [26]. The geometric construction used for determination of the angles is called *construction of the inner tangent to two circles*. The angles are determined with respect to a line through the center of the SDDs and perpendicular to the surface of the SDDs. The grid in the dark-box is 2.5 cm times 2.5 cm. A plot of the determination of the scattering angles and the values of the latter are shown in **Fig: 3.7**, the grid depicted in the figure does not match the grid in the dark-box.

The specified screw positions, shown in the above mentioned figure were changed in the course of the work, the representation in the picture is to be understood as a representation of the principle. In the following only the values of the angles will be given.

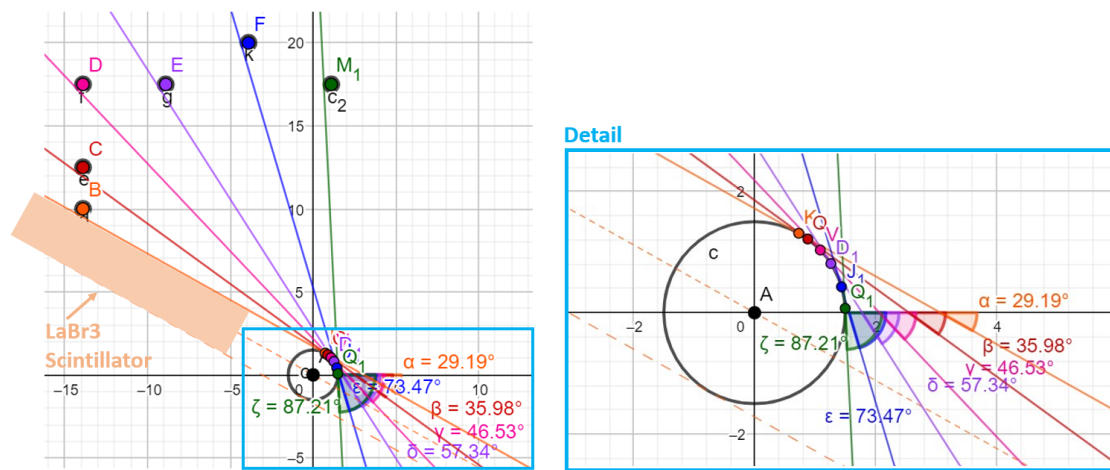


Figure 3.7 Geometrical Determination of the Scattering Angles.

The angles are determined with respect to a line through the center of the SDDs and perpendicular to the surface of the SDDs (in both plots the horizontal axis). The geometric construction is called *construction of the inner tangent to two circles*. The grid in the dark-box is 2.5 cm times 2.5 cm, the depicted grid does not match the grid in the dark-box.

Left: Determination of the scattering angles with the program *GeoGebra*. The colored dots (B, C, D, E, F, M1) illustrate the screws with a diameter of 9 mm. The distance between position B and C is 2.5 cm, between C and D and also D and E it is 5.0 cm. The LaBr₃ scintillator is shown as an orange rectangle.

Right: The detail around the pivot point A of the LaBr₃ scintillator is shown, lying directly under the center of the SDD.

3.2.3 Including Source Positions

The Compton scattering experiments performed in the scope of thesis can be separated in measurements in two kinds of setups depending on the position of the source.

Measurements with Two Source Positions:

First, four measurement runs were carried out with two source positions, each perpendicular to the surface of the SDDs, one for angles $< 90^\circ$ and one position for angles $> 90^\circ$, where angle, as mentioned above, is meant as the angle between the beam axis of the radioactive source and the position of the LaBr₃ scintillator. The determination of the angle depending of the position of the screws, explained above in section 3.2.2, refers to

angles $< 90^\circ$. Angles $> 90^\circ$ can be calculated by: 180° -angle. The positions of the sources in this case are shown in **Fig:** 3.8. The values of the angles used for the measurements are presented in the section of the individual measurement, section 3.5.2.1, 3.5.2.2 , 3.5.2.3 and 3.5.2.4.

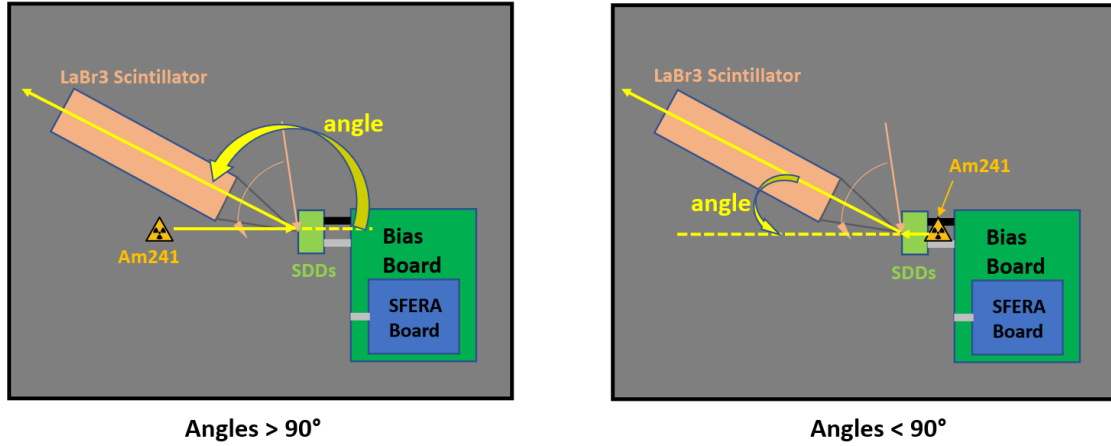


Figure 3.8 Positions of the Source in Measurements with Two Source Positions (not to scale): Two source positions, each perpendicular to the surface of the SDDs are used for an individual measurement run, one for angles $< 90^\circ$ (left) and one position for angles $> 90^\circ$ (right). Angle is meant as the angle between the beam axis of the radioactive source and the position of the LaBr₃ scintillator. The determination of the angle depending of the position of the screws, explained in section 3.2.2, refers to angles $< 90^\circ$. Angles $> 90^\circ$ are calculated by: 180° -angle. The values of the angles used for the measurements are presented in the section of the individual measurement run, section 3.5.2.1, 3.5.2.2 , 3.5.2.3 and 3.5.2.4

Measurements with One Source Position in the rearranged Setup:

Finally, one measurement run was performed with only one source position not perpendicular to the surface of the SDDs. Therefore the setup was rearranged such, that the SDD module was placed more in the center of the dark-box to get a larger range for placing the LaBr₃. In **Fig:** 3.9 the possible position of the LaBr₃ scintillator is presented as the range between the two orange lines, restricted by the volume of the dark-box, the size of the LaBr₃ detector and the collimator, with the source inside. Furthermore, different screw positions for experimental reproduction of the scattering angles were chosen and also the LaBr₃ is touched in two manners: Above the horizontal green line the screws touch the U-profile (with the LaBr₃) on the back, whereas below the green dashed line the screws touch the U-profile (with the LaBr₃) on the front, viewed from outside. Because of symmetry, only part of the angles have to be determined with *GeoGebra*. That is done by changing the screw coordinates in the DGS as described above, which leads to angles also wrt the axis perpendicular to the SDDs. The final angles between the beam axis of the radioactive source and the position of the LaBr₃ scintillator are then calculated by using the angle between the line of the beam axis and the line perpendicular to the SDDs (69.3°), illustrated in **Fig:** 3.9 by a dashed green angle. The values of the angles used for the individual measurement run are presented in section 3.5.3.

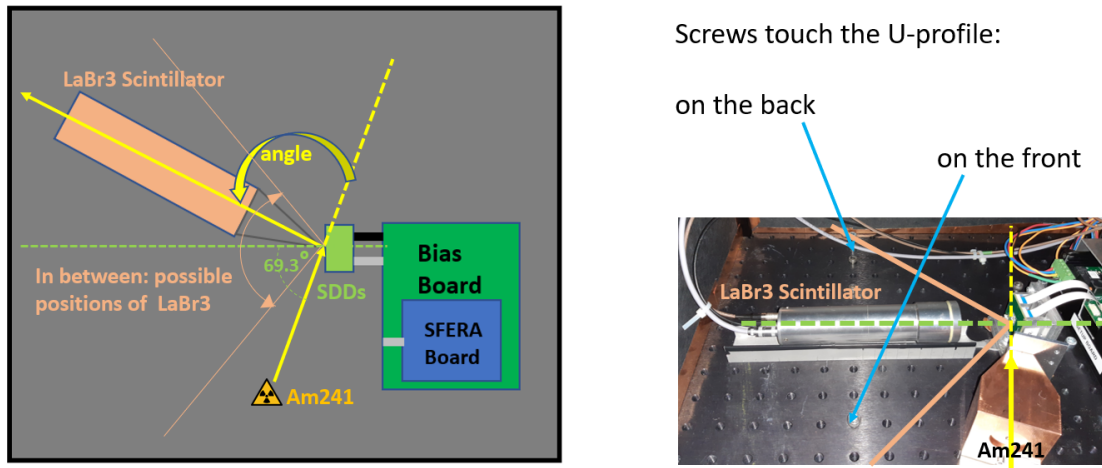


Figure 3.9 Position of the Source in Measurements in the rearranged Setup (not to scale): Only one source position not perpendicular the surface of the SDDs in the rearranged setup (SDDs placed more in the center of the dark-box) is used. The possible position of the LaBr₃ scintillator is presented as the range between the two orange lines.

Right: Different screw positions for experimental reproduction of the scattering angles were chosen. The U-profile with the LaBr₃ on it is touched in two manners: Above the horizontal green dashed line the screws touch the U-profile on the back, whereas below the green dashed line the screws touch the U-profile on the front, viewed from outside. Because of the symmetry, only part of the angles have to be determined with *GeoGebra*. The outcome are angles also wrt the axis perpendicular to the SDDs.

Left: The final angles between the beam axis of the radioactive source and the position of the LaBr₃ scintillator are then calculated by using the angle between the line of the beam axis (yellow) and the line perpendicular to the SDDs (69.3°), illustrated by a dashed green angle. The values of the angles used for the individual measurement run are presented in section 3.5.3.

3.3 Americium Sources

In the scope of this thesis two Americium (²⁴¹Am) sources with different activities were used. The sources also differ in their shape. The activities and the extents of the two radioactive sources are:

- **Source 1:** Activity of 0.375 MBq, point-like shape
- **Source 2:** Activity of 2.170 MBq, cylindrical shape

The 59.54 keV γ -ray emission of the ²⁴¹Am source is used as a radioactive source for the Compton scattering experiment. Moreover, a calibration of the energy spectra of the SDDs and the LaBr₃ can be conducted. The radioactive isotope ²⁴¹Am decays to ²³⁷Np (Neptunium) via electron capture with a half-life of $T_{1/2} = 2.2$ yr. The process of EC leads to a vacancy in the L-shell which is filled by an electron from a higher-lying shell, releasing the resulting surplus of energy in the form of Auger electrons and X-rays. The X-ray lines with energies of $E_{L\alpha_2} = 13.76$ keV with an intensity of 1.07%, $E_{L\alpha_1} = 13.95$ keV with an intensity of 9.60% can be used for calibration of the SDD energy spectra. Separate neighboring lines can not be resolved individually if the resolution of the detector is not sufficient. Therefore, the mean value weighted by the relative intensity of the components is considered. The 59.54 keV γ -ray emission with an intensity of 35.9% can be used for calibration of the LaBr₃ spectrum. There are several further X-ray and γ -ray lines. They are presented only if they become relevant during the measurements in the individual section. The values can be looked up in [20] or online (NuDat 3.0), maintained and updated by the National Nuclear Data Center (NNDC) [10].

3.4 Analysis Chain

As described above in section 3.2.1, data is acquired with the CAEN DT5730S digitizer, using the so called DPP-PSD Firmware in the list mode. The output are root files separately for each channel. Channel 0 is referred to the LaBr₃ scintillator and channel 1 – 7 to the seven SDDs. The energies of events (the raw data) are given in so called ADC units, the timestamps in pico seconds. The evaluation of the data is done with python programs in the jupyter interface, following the general analysis chain which is illustrated schematically in **Fig:** 3.10 and presented in the following. The process of the analysis chain is run through for each angle during the evaluation of each measurement run. To ensure a better understanding of the analysis chain, the steps two to five of the analysis are illustrated by figures taken from the analysis of the final measurement run in the rearranged setup with one source position and collimator (section 3.5.3). For simplicity only one angle (110.66°) and only one channel (6) of the seven SDD channels are considered, unless otherwise stated.

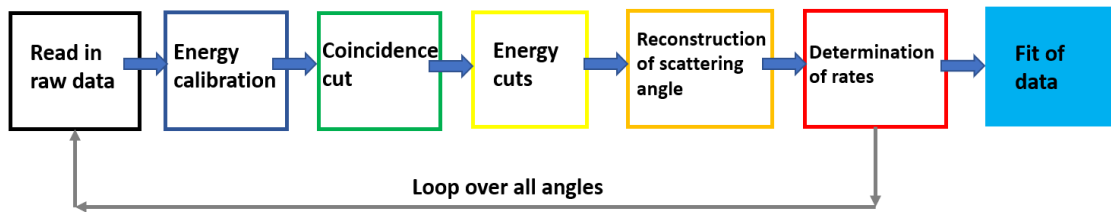


Figure 3.10 Analysis Chain schematically.

The general analysis chain is illustrated schematically. The process, which is presented in more detail in the text, is run through for each angle during the evaluation of each measurement run. In the sequence of figures the steps from energy calibration **Fig:** 3.11 to reconstruction of the scattering angle **Fig:** 3.14 are illustrated exemplary for the measurement in the rearranged at $\Theta=110.66^\circ$. For simplicity from the SDDs only channel 6 is considered.

The steps of the analysis chain, which are illustrated schematically in Fig: 3.10 are the following:

- **Read in of the raw data:** The root files are read in separately for each channel and the raw spectra in ADC units are determined for the LaBr₃ detector (channel 0) and for the seven SDDs (channel 1-7).
- **Energy calibration:** The energy calibrations are slightly different, depending on the measurement run, and will be discussed below in section 3.5, individually for each measurement. In general, calibrations are performed for each channel separately by fitting a dominant peak (ADC units) with a Gaussian. From that, the positions (in ADC units) of the peaks and the standard deviations (in ADC units) are given. The spectra can be calibrated by using the dominant lines of a source, see also section 3.3 for ²⁴¹Am. The X-ray lines with energies (weighted by intensities) of $E_{L_{\alpha 2}}=13.76$ keV and $E_{L_{\alpha 1}}=13.95$ keV are used for calibration of the SDD energy spectra. This is done for the measurement run without any shielding between source and SDDs, see section 3.5.2.1. In all other measurement runs, the peak positions for channel 1-7 from this calibration are used for calibration. The 59.54 keV γ -ray emission of ²⁴¹Am is used for calibration of the LaBr₃ spectra in all measurement runs without collimator. In the measurement runs with collimator, described in section 3.5.2.4 and 3.5.3, the calibration of the LaBr₃ energy spectra are

performed by using the Barium line from Lanthanum decaying to Barium ($^{138}_{58}\text{Ba}$) via electron capture (EC) at 37.4 keV, see [3]. Generally, linear energy calibrations were performed. The FWHM can be calculated from the calibrated standard deviation described above.

- **Coincidence cut:** Only events with interactions in both detectors at (almost) the same time are taken into account. For the coincidence window size 300 ns and for the window offset 60 ns were assumed, both taken from preliminary investigations performed by Matthias Meier.
- **Energy cuts:** Only the energy range of interest is considered. The sum of energies, deposited in both detectors is 59.5 keV. From the angle between the LaBr_3 scintillator and the beam axis of the source (the scattering angle, shortly denoted as angle) and the initial energy of the photon in the Compton scattering process, the energies of the electron and the scattered photon can be calculated, see section 1.3.2 and see **Fig: 1.5**. The energy cut in the LaBr_3 is set as range around the calculated energy of the scattered photon at the measured angle (e.g. $110.66^\circ \pm 13$ keV). The energy cut in the SDDs is set in all measurements except the measurement without Al shielding as fixed range between 3.5 keV and 13.5 keV. The cuts in the measurement without Al shielding are set as a range (± 2 keV) around the calculated value of the energy of the scattered electron at the measured angle, to avoid random coincidences from events, which are measured in the same coincidence window with an energy of 13.9 keV in the SDDs and 59.5 keV in the LaBr_3 scintillator and which could be construed as Compton scattering of a photon with an initial energy of 75 keV.
- **Reconstruction of the scattering angle:** A reconstruction of the angle after coincidence cut and energy cut can be performed by rearranging the equations in section section 1.3.2 and solving for Θ .
- **Determination of rates and uncertainty of rates:** The rates are calculated by the number of the remaining counts divided by the measurement time. The uncertainties of rates (according to Poisson) are calculated by the square-root of the number of the remaining counts divided by the measurement time. The rates considering random coincidences and the total rate uncertainties considering propagation of the statistical uncertainties are determined according to **Appendix A.2**.

After running through the analysis chain for each angle, the rates considering random coincidences are given as data-points depending on the scattering angle Θ . The rates are normalized by the raw rates in the SDDs after energy cut to take e.g. different distances between the source and the SDDs into account. Finally, a fit of the data with the fit-function according to incoherent scattering by considering the effect of detector response is performed, to consider the opening angle of the LaBr_3 detector. Thereby the normalization is the free variable. The Θ -differential cross-section for incoherent scattering, equation 1.8, is convoluted with the projection of a circle, leading to the the model which describes the incoherent scattering considering the effect of detector response, illustrated by the blue line in **Fig: 3.15**. The differences between incoherent scattering with and without considering detector response are small in the angle range relevant for this thesis ($45^\circ - 150^\circ$).

Sequence of Figures describing step two to five of the analysis chain exemplary: Step two to five of the analysis chain, which are illustrated schematically in **Fig: 3.10** and described above, are now presented as a sequence of figures describing the analysis for an angle of 110.66° and SDD channel number 6 for the measurement in the rearranged setup with collimator and 3 mm Al shielding (see section 3.5.3).

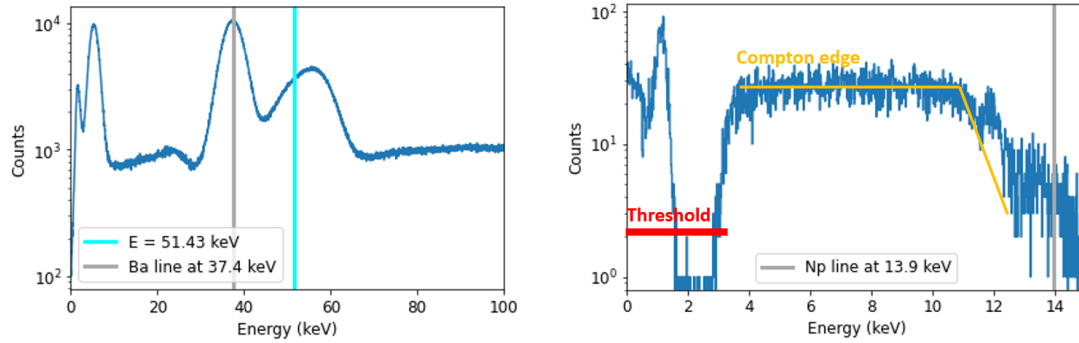


Figure 3.11 Energy Calibration.

The calibrated spectra are shown. In general, calibrations are performed for each channel separately by fitting a dominant spectra peak of the raw spectrum obtained from the read in with a Gaussian.

Left: The calibration of the LaBr₃ energy spectrum is performed by using the Barium line from Lanthanum decaying to Barium ($^{138}_{58}\text{Ba}$) via electron capture at 37.4 keV (grey), see [3]. Moreover, the calculated energy of the scattered photon (cyan) at the measured angle (e.g. 110.66°) ± 13 keV is shown.

Right: For the calibration of the spectrum of SDD channel 6, the calibration of the first measurement without shielding is used (e.g. the peak position for channel 6), as the peak at 13.9 keV is no longer visible because of the 3mm Al shielding in front of the collimator. The Compton edge (yellow) is shown at around 11.3 keV. Moreover, the lower threshold used in the energy cut of the SDD spectrum is shown (in red).

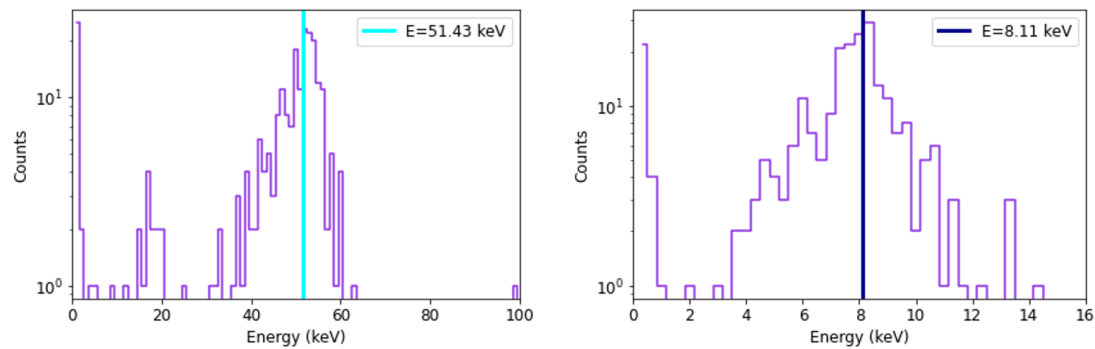


Figure 3.12 Coincidence Cut.

The calibrated spectra after coincidence cut are shown.

Left: From the coincident events in LaBr₃ detector with them in SDD channel 6 the energy spectrum in the LaBr₃ after coincidence cut is given (violet). The cyan line is the calculated energy of a photon with an initial energy of 59.5 keV after being scattered about $\Theta=110.66^\circ$.

Right: The energy spectrum of the electrons channel 6 is illustrated (violet) The dark blue line indicates the calculated energy of a scattered electron for a scattering angle of $\Theta=110.66^\circ$ of the photon.

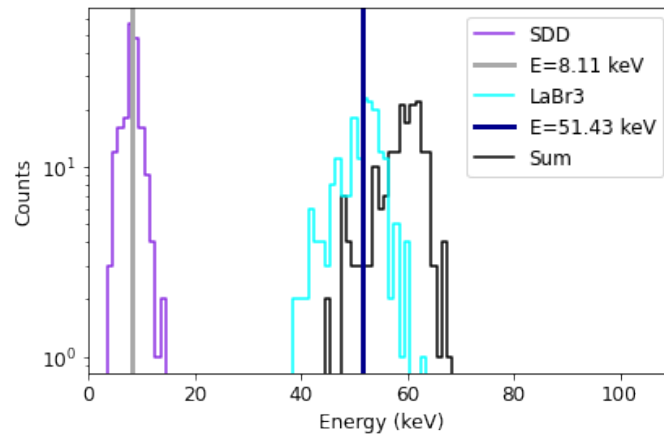


Figure 3.13 Energy Cuts.

The calibrated spectra after coincidence cut and energy cut are shown in one plot. Thereby, the energy cut in the LaBr₃ were set as range around the calculated energy of the scattered photon at the measured angle (e.g. $110.66^\circ \pm 13$ keV). The energy cut in the SDD were set as fixed range between 3.5 keV and 13.5 keV. The spectrum of SDD channel 6 is illustrated in violet, that of the LaBr₃ scintillator in cyan. The sum of energies, deposited in both detectors is 59.5 keV. From the angle between the LaBr₃ scintillator and the beam axis of the source and the initial energy of the photon in the Compton scattering process, the energies of the electron (8.1 keV) and the scattered photon (51.4 keV) can be calculated, see section 1.3.2 and see **Fig:** 1.5. The peaks of the spectra arise at the calculated energies.

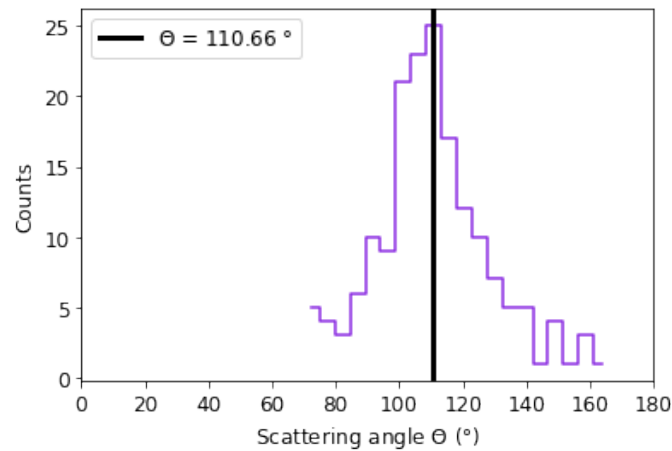


Figure 3.14 Reconstruction of the Scattering angle.

A calculation of reconstructed scattering angles can be performed by rearranging the equations in section 1.3.2 and solving for Θ . The input are the calibrated spectra after coincidence and energy cut from the previous step, see **Fig:** 3.13. The reconstructed scattering angles are distributed around the scattering angle experimentally performed by the position of the LaBr₃ detector wrt the beam axis of the ²⁴¹Am source.

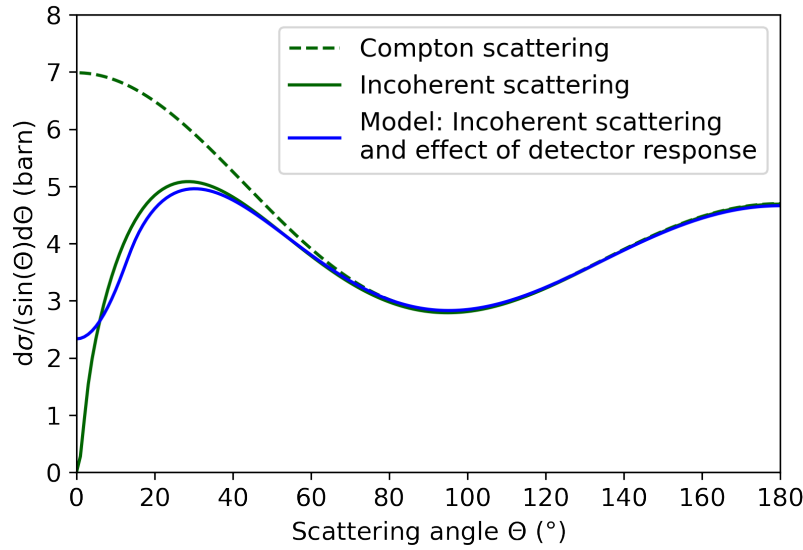


Figure 3.15 Model describing the measured Cross-section.

The Θ -differential cross-section for incoherent scattering, equation 1.8, is convoluted with the projection of a circle, leading to the the model which describes the incoherent scattering including the effect of detector response (blue line). The cross-sections of Compton scattering (green dashed) and incoherent scattering (green), both without the effect of the detector response are shown for comparison. The differences between incoherent scattering with and without detector response are small in the angle range relevant for this thesis ($45^\circ - 150^\circ$).

3.5 Measurements

As stated in section 3.1, the physical motivation for the characterization measurements carried out in the scope of this work is to reproduce the angle dependent Θ -differential cross-section for incoherent scattering according to the modified Klein-Nishina equation by a Compton scattering experiment. Thereby the SDD module, originally designed for the TRISTAN experiment, is used as scatter target and a Lanthanum(III)Bromide detector as a calorimeter. The scattering angles are experimentally performed by changing the angle between the beam axis of the radioactive source and the LaBr_3 detector. In this section the characterization measurements carried out are presented and the results are discussed, starting with a preliminary measurement with a ^{55}Fe source in subsection 3.5.1, followed by the Compton scattering measurements in developing setups with two source positions in section 3.5.2. The measurements in the rearranged setup are described and discussed in section 3.5.3. Details about the Americium (^{241}Am) sources are given above in section 3.3.

3.5.1 Measurements with a ^{55}Fe Source

A measurement with a ^{55}Fe source was carried out to check the performance of the SDD module by determination of the detector resolution. It was conducted in the setup described above but without using the LaBr_3 scintillator. For this purpose, a ^{55}Fe source was placed directly in front of the SDD module. ^{55}Fe is a radioactive isotope which decays to ^{55}Mn via electron capture (EC) with a half-life of $T_{1/2} = 2.74$ yr. The process of EC leads to a vacancy in the K-shell which is filled by an electron from a higher-lying shell, releasing the resulting surplus of energy in the form of Auger electrons and X-rays. The

X-ray lines have energies of $E_{K_\alpha}=5.90$ keV and $E_{K_\beta}=6.49$ keV and are used for detector calibrations and determination of the resolution. The calibrated spectra for all channels are presented in the left part of **Fig: 3.16**. As spectral resolution the definition FWHM is used, determined in eV. The results, shown in the right part of **Fig: 3.16**, are around 250 eV, which is good, even the Si escape peak is visible in the spectra, plotted on the left part. It arises, when an incident photon with a characteristic energy is absorbed in the detector volume. If the energy is sufficiently high, a photo-electron from an inner shell of the Si atom is produced. Subsequently, the excited atom can emit a fluorescence X-ray photon, a K_α photon, which is most of the times reabsorbed and therefore contributes to the charge pulse. That photon can also escape from the crystal, carrying off the definite energy of the Si K_α energy. The charge pulse appears as a photon energy $E_{initial} - E_{K_\alpha}$ and therefore shows up in the spectrum as separate peak [4]. The spectra of all channels match very well, shown in the left part of **Fig: 3.16**.

This measurement was repeated after the measurement run in the rearranged setup with only one source position, see section 3.5.3.

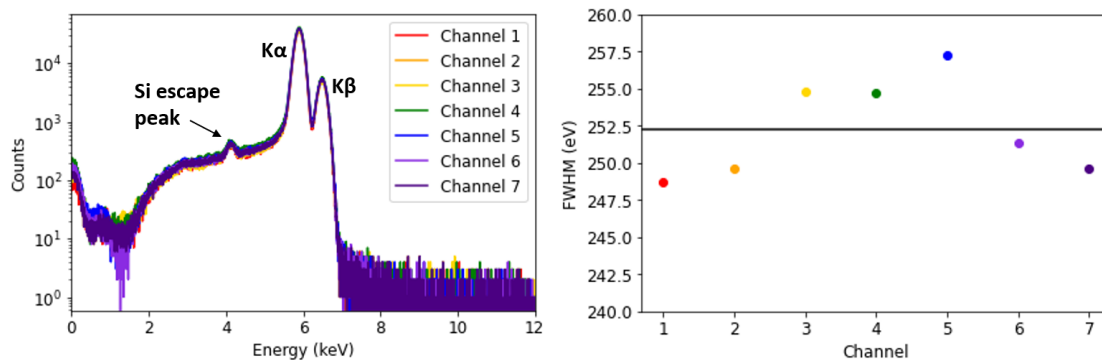


Figure 3.16 Calibrated ^{55}Fe spectra and Resolutions for all channels.

The X-ray lines have energies of $E_{K_\alpha}=5.90$ keV and $E_{K_\beta}=6.49$ keV and were used for detector calibration and determination of the resolution.

Left: Calibrated ^{55}Fe spectra for all channels, the E_{K_α} peak at 5.90 keV and the E_{K_β} peak at 6.49 keV are shown. Even the Si escape peak is visible.

Right: The spectral resolution FWHM, determined in eV, is illustrated depending on the channel. The mean FWHM is ~ 252 eV (black line).

3.5.2 Measurement Runs in an Evolving Setup (two Source Positions)

In the following subsections, the measurements in an evolving setup are presented. For all measurements, the radioactive source was placed at two different positions for measurements of scattering angles smaller or larger than 90° , as described in section 3.2.3 and shown in **Fig: 3.8**. The setup changed only in that the radioactive source holder was altered to add different shielding between source and SDD module. Since the rates decrease with increasing distance between the source and the detector, two sources of different strengths were used (see section 3.3). Photographs of the evolving setup exemplary for angles larger than 90° are shown in **Fig: 3.17**. From the upper left to the lower right part, the evolving setup is shown. Starting with a setup without any shielding between source and SDD module, presented in section 3.5.2.1 in the upper left, first a 3 mm Aluminium (Al) shielding was added between source and SDD module, see section 3.5.2.2, shown in the upper right. Two 5 mm Copper (Cu) shields were then designed which also act as holder (section 3.5.2.3), illustrated in the lower left. Finally two collimators were

constructed into which the source was inserted (section 3.5.2.4), the one for angles larger 90° is shown in the lower right part of the figure. Moreover the change of the source is presented. The source with higher activity was used in measurement runs with Copper shielding and collimator as the distance between source and SDD module had increased for angles larger 90° . All source holders for measurements at angles smaller 90° were constructed similarly as shown in **Fig:** 3.17 for angles larger 90° , but due to the restricted place between the SDD module and the Bias-board the holders and also the collimator are smaller.

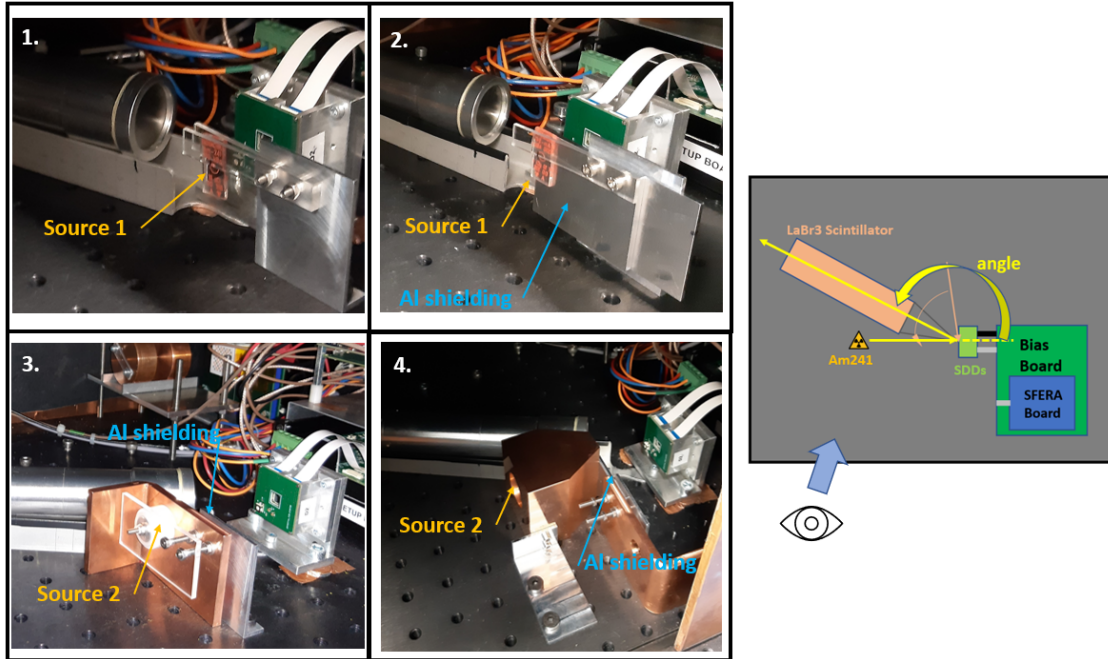


Figure 3.17 Evolving Setup for measurements at angles $> 90^\circ$, exemplary.

Photographs of the evolving setup exemplary for angles larger than 90° are illustrated.

From the upper left (1.) to the lower right part (4.), the evolving setup is shown. Starting with a setup without any shielding between source and SDD module (1.), presented in section 3.5.2.1 in the upper left, first a 3 mm Aluminium (Al) shielding was added (2.), see section 3.5.2.2, shown in the upper right. A 5 mm Copper (Cu) shield was then added (3.) (section 3.5.2.3), illustrated in the lower left. Finally two collimators were constructed into which the source was inserted (section 3.5.2.4), shown in the lower right part of the figure (4.). Moreover the change of the source is presented. The photographs were made in direction of the blue arrow, shown in the schematical drawing taken from **Fig:** 3.8.

The source holders (the collimator) for angles $< 90^\circ$ were constructed similarly.

3.5.2.1 Measurement run without Shielding

First, source 1 with the lower activity (see section 3.3) was used in the setup without any shielding between source and SDD module. The source positions are illustrated in **Fig:** 3.8 schematically. Photographs of the holder with the source are shown in the upper left part of **Fig:** 3.17 for angles $> 90^\circ$. Measurements in the setup were experimentally performed at the angles Θ (angle between the LaBr₃ detector and the beam axis of the source) given in equation 3.1.

$$\Theta \in [29.2, 36.0, 46.5, 57.3, 73.5, 87.2, 106.5, 133.5, 150.9] \quad (3.1)$$

The distance between the source and the SDD module was the same for both positions of the source.

The results of the first measurement run were used as the basis for improvements to the setup and for evaluation in the following experiments. The analysis chain (section 3.4), deviates from that presented above in the sequence of figures, namely in **Fig: 3.11**. The spectrum in channel 6 is illustrated in **Fig:3.18** for the angles $\Theta \sim 74^\circ$ and $\Theta \sim 133^\circ$, exemplary. The Energy calibration in the SDDs were done by fitting the dominant peak using the Np line from ^{241}Am at 13.9 keV. The positions of that peak (in ADC units) were used in the evaluations of all measurements conducted later for calibration. Moreover, the energy cut in the SDDs was different from the subsequent measurements. The energies of the scattered electrons were calculated for each angle and the range of considered events was set to $E_e \pm 2$ keV, which leads to energy cuts depending on the angle Θ , illustrated in **Fig: 3.18**. As for the spectrum itself, there are several additional lines. The Np line at 11.89 keV from ^{241}Am is visible.

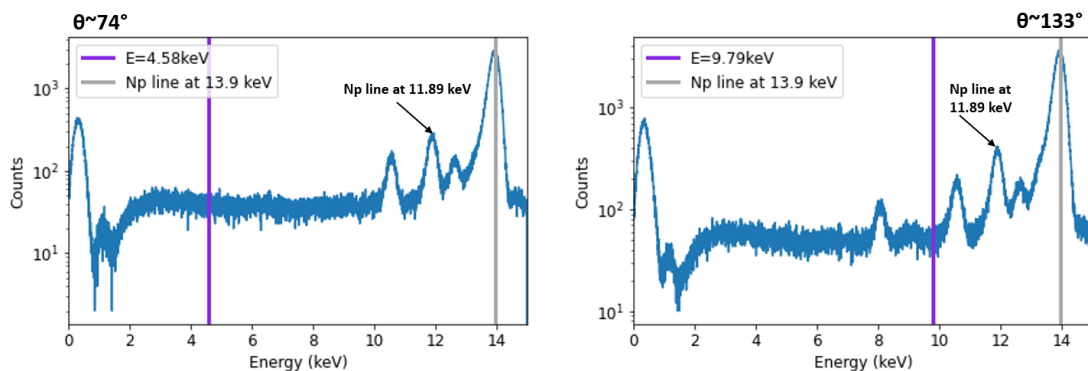


Figure 3.18 Energy Spectra and energy cuts in SDD channel 6 for two angles, exemplary.

The Energy calibration was done by fitting the dominant peak using the Np line from ^{241}Am at 13.9 keV (grey line). Several additional lines arise. The Np line at 11.89 keV from ^{241}Am is visible.

Left: The spectrum in channel 6 is illustrated for angle $\Theta \sim 74^\circ$. The energies of the scattered electrons were calculated for each angle (dark violet line) and the range of considered events in energy cut was set to $E_{cut} = 4.58 \text{ keV} \pm 2 \text{ keV}$, for an angle of $\sim 74^\circ$.

Right: The spectrum in channel 6 is illustrated for the angle $\Theta \sim 133^\circ$. The energies of the scattered electrons were calculated for each angle (dark violet line) and the range of considered events was set to $E_{cut} = 9.79 \text{ keV} \pm 2 \text{ keV}$ for an angle $\sim 133^\circ$. An additional line arises around ~ 8 keV which is not visible for the angle $\sim 74^\circ$. It could come from the decay of the daughter ^{237}Np at 8.22 keV or from a Copper line at 8.04 keV.

The Compton event rates for all angles, which result from the measurements and the evaluation described above were fitted taking the detector response of the LaBr_3 detector into account. This was achieved by convoluting the Θ -differential cross-section for incoherent scattering with the projection of a circle which has a diameter equal to the diameter of the LaBr_3 detector (1 inch). The result is shown in **Fig: 3.19**, the deviations between the theory (blue line) and measurement (orange dots) are huge.

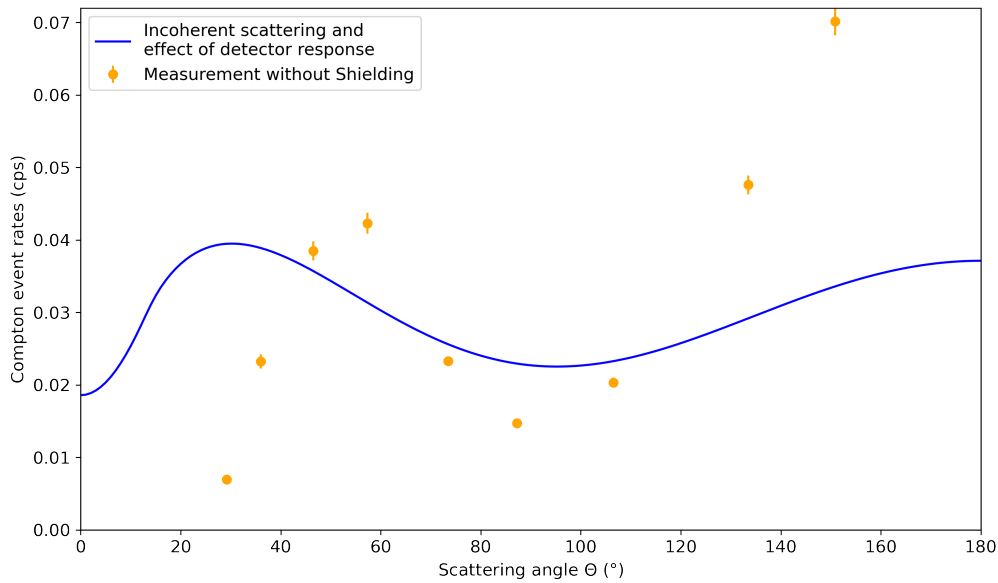


Figure 3.19 Measurement without shielding: Compton Event rates depending on the scattering angle Θ .

The Compton event rates (orange dots) were fitted with the incoherent scattering cross-section including the effect of detector response (blue line), the deviations between the theory and measurement are huge.

To investigate the influence of the random coincidences, density plots were performed, showing the counts depending on the sum of the energies in the SDDs and the LaBr_3 , and the scattering angle Θ . Exemplary the density plots for angles $\Theta \sim 74^\circ$ and $\Theta \sim 133^\circ$ are shown in **Fig: 3.20**. The cuts were set as a range around the calculated values of the energies in the detectors for each scattering angle, which is illustrated as distorted red rectangle. Events from random coincidences are clearly visible. They are measured in the same coincidence window with an energy of 13.9 keV in the SDDs and 59.5 keV in the LaBr_3 scintillator. The events inside the blue ellipse could be construed as Compton scattering of a photon with an initial energy of 75 keV scattered by $\Theta \sim 135^\circ$. Moreover, the population of the Compton events (inside the distorted rectangle) is shifted towards the random coincident events (inside the ellipse) for larger angles, which lead to an overlap. This could partly explain the huge rates for larger angles shown in **Fig: 3.19**. On the other hand photons with initial energies according to the other arising lines, could have been considered. Therefore, an Aluminium shielding was implemented in the following measurement run.

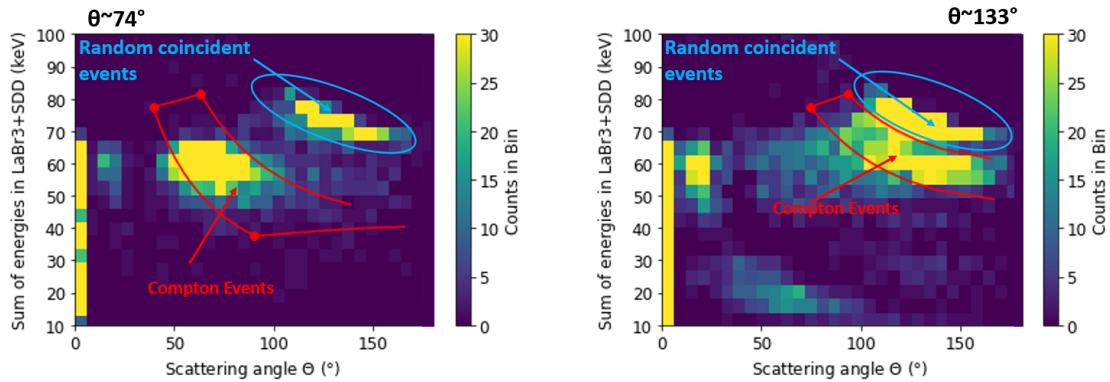


Figure 3.20 Investigation of Random coincident Events.

The plots illustrate density plots after coincidence cut for angles $\Theta \sim 74^\circ$ and $\Theta \sim 133^\circ$. The counts depending of the sum of the energies in the SDDs and the LaBr₃ and the scattering angle Θ are depicted. The Energy cuts were set as a range ($E_e \pm 2$ keV) around the calculated values of the energies in the detectors for a scattering angle, e.g. $\Theta \sim 74^\circ$ and $\Theta \sim 133^\circ$, shown as distorted red rectangle. Random coincident events are clearly visible (inside the blue ellipse). They are measured in the same coincidence window with an energy of 13.9 keV in the SDDs and 59.5 keV in the LaBr₃ scintillator. The events inside the blue ellipse could be construed as Compton scattering of a photon with an initial energy of 75 keV scattered by $\Theta \sim 135^\circ$.

Left: The population of the Compton events (inside the distorted rectangle) is separated from the random coincident events for an angle of $\Theta \sim 74^\circ$.

Right: The population of the Compton events (inside the distorted rectangle) is shifted towards the random coincident events (inside the blue ellipse) for higher angles, which lead to an overlap. This leads to the huge rates for larger angles.

3.5.2.2 Measurement Run with 3 mm Aluminium Shielding

The setup changed in this measurement only in that an 3 mm Al shielding was added between source and SDD module. The transmission probability through a 3 mm Al plate is shown in **Fig:** 3.21.

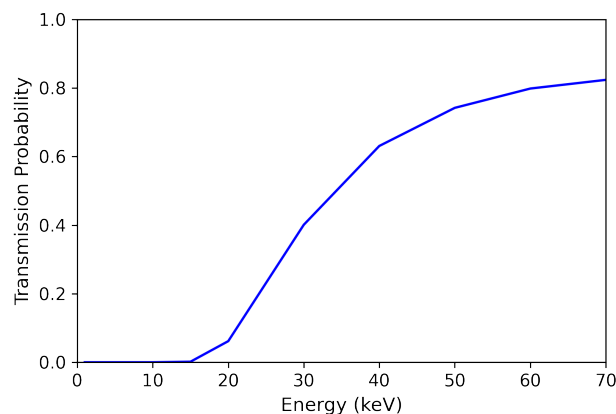


Figure 3.21 Transmission Probability through a 3 mm Al plate.

The Transmission Probability through a 3 mm Al plate is shown, depending on the energy. Energies below ~ 15 keV are almost completely shielded but 80% of photons with an energy of 60 keV are transmitted.

The source 1 with the lower activity was used as before in the same distance to the SDD module for all angles. The source positions are illustrated in **Fig:** 3.8 schematically. Photographs of the holder with the source are shown in the upper right part of **Fig:** 3.17 for

angles $> 90^\circ$. Measurements in the setup were experimentally performed at the scattering angles Θ (angle between the LaBr_3 detector and the beam axis of the source) are given in equation 3.2.

$$\Theta \in [46.5, 51.6, 57.3, 63.9, 73.5, 87.2, 106.5, 116.1, 122.7, 133.5, 144.0, 150.9] \quad (3.2)$$

Compared to the measurements without shielding, it is visible in **Fig: 3.22** and **Fig: 3.23**, exemplary for an angle $\sim 133^\circ$, that both the random coincidence events with a population around 75 keV and 135° are shielded as well as incident photons with energies lower than 15 keV coming e.g. from lines below 15 keV. Also the Np line at 13.9 keV is not visible anymore (peak around dark violet line) in **Fig: 3.22**. It can also be seen that the energy cut range has changed (distorted red rectangle). The energy range of consideration is now fixed.

For evaluating this measurement run and all measurement runs which follow, the energy cut range has a fixed range as explained and depicted in the sequence of figures, especially visualized in the calibrated spectrum of channel 6 in **Fig: 3.11**. The energy range of consideration is now fixed between 3.5 keV and 13.5 keV.

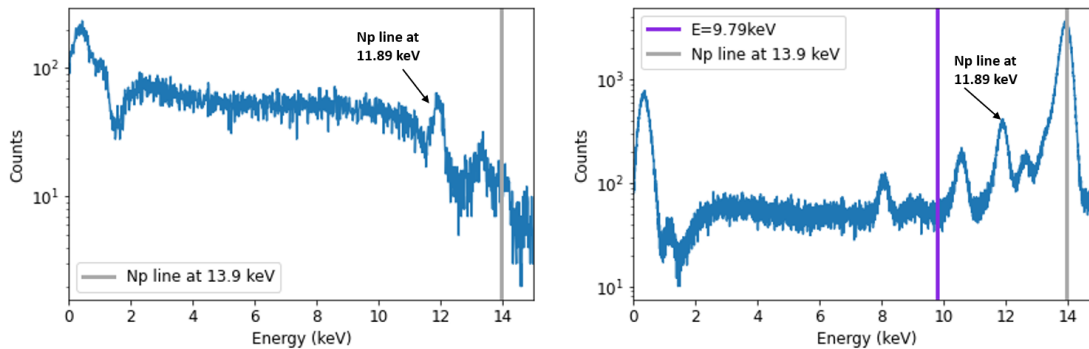


Figure 3.22 Improvements through Implementing a 3 mm Al Shielding between Source and SDDs.

A comparison of the spectra at an angle $\sim 133^\circ$ is shown for the measurements with and without a 3 mm Al shielding.

Left: The spectrum of channel 6 is shown for the measurement at $\sim 133^\circ$ with 3 mm Al shielding. Most of the lines below 15 keV are not visible anymore. However, the Np line at 11.89 keV is slightly visible. The position of the Np line at 13.9 is shown by the grey line. The peak is also slightly visible.

Right: The spectrum of channel 6 for the measurement at $\sim 133^\circ$ without shielding is shown for comparison.

In contrast to the measurement run without shielding, random coincidences, namely events in one detector which are uncorrelated to events in the other detector, were taken into account when determining the Compton event rates, see **Appendix A.2**. The Compton event rates in cps are shown as orange dots in **Fig: 3.24**. Furthermore, the Compton event rates considering random coincidences (red dots) are illustrated. The latter were fitted with the incoherent scattering cross-section including the effect of detector response (blue line). The deviations between the theory and measurement are still huge.

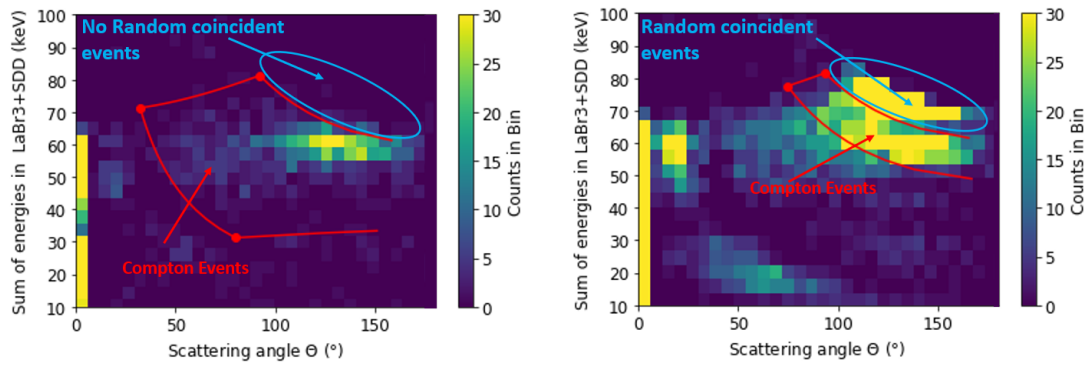


Figure 3.23 Shielding of Random Coincident Events.

A comparison of density plots after coincidence cut for measurements with and without 3 mm Al shielding at an angle $\sim 133^\circ$ is shown.

Left: It is visible that in case of the measurement with 3 mm Al shielding, the random coincidence events with a population around 75 keV and 135° are shielded. The energy range of consideration is now fixed between 2.0 keV and 12 keV for comparison (3.5 keV to 13.5 keV was later used), shown as the red distorted rectangle.

Right: The density plot after coincidence cut for measurements without 3 mm Al shielding at an angle $\sim 133^\circ$ is shown for comparison, explanation see **Fig. 3.20**.

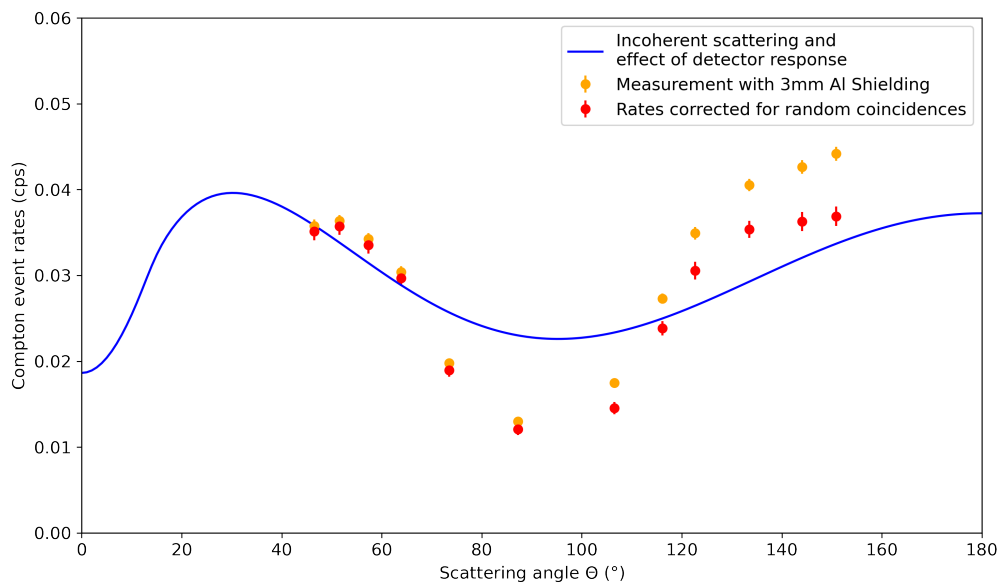


Figure 3.24 Measurement with 3 mm Al shielding: Compton Event rates depending on the scattering angle Θ .

The Compton event rates from the measurement with 3 mm Al shielding are illustrated by orange dots. The rates corrected for random coincidences and the total rate uncertainties considering the propagation of the statistical uncertainties are determined according to **Appendix A.2** for all angles (red dots). They were fitted with the incoherent Compton scattering cross-section considering the effect of detector response (blue line). The deviations between the theory and measurement are still huge.

3.5.2.3 Measurement run with 3 mm Aluminium and 5 mm Copper Shielding

In this measurement run a Copper shielding was added. For this purpose, two new holders were designed for the source, which also act as shielding between the source and the detectors. They have an L-shape with a 12 mm diameter hole behind which the ^{241}Am source is fixed. The thickness of the Cu holder is about 5 mm. Since for the measurements

at angles larger than 90° the holder has a larger distance to the SDD module, the source with the higher activity (source 2, see 3.3) is used for all measurements. A photograph of the Cu-holder which also acts as shielding with the source is shown in the lower left part of **Fig: 3.17** for angles larger 90° . The positions of the source are presented in **Fig: 3.8** schematically. In contrast to the previous measurement runs, the distance between the source and the SDD module is no longer the same for measurements at small and large angles. The 3 mm Al shielding was added in front of the holder as in the measurement described in the previous section. The transmission probability through a 5 mm Cu shielding depending on the energy is shown in **Fig: 3.25**. All photons with energies below ~ 60 keV are almost completely shielded.

Fig: 3.25. The scattering angles between the LaBr₃ detector and the beam axis exper-

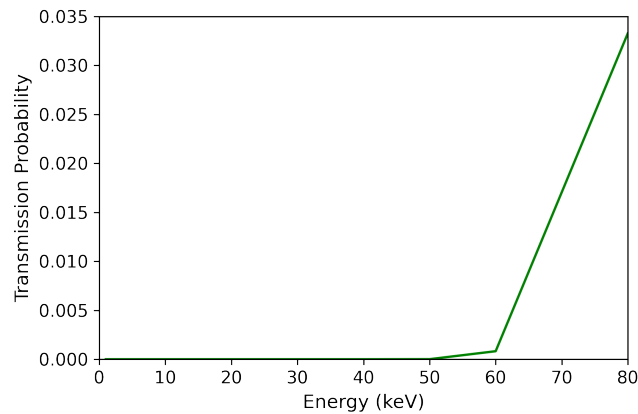


Figure 3.25 Transmission Probability through a 5 mm Cu plate.

The Transmission Probability through a 5 mm Cu plate is shown, depending on the energy. All photons with energies below ~ 60 keV are almost completely shielded.

imentally performed during the measurement run in the setup with two source positions and 3 mm Al and 5 mm Cu shielding are given in equation 3.3.

$$\Theta \in [46.5, 51.6, 57.3, 73.5, 87.2, 106.5, 116.1, 133.5, 150.9] \quad (3.3)$$

The evaluation procedure was the same as that described in the previous section. The Compton event rates corrected for random coincidences (red dots) are illustrated for all angles in **Fig: 3.26**. They were fitted with the incoherent Compton scattering cross-section including the effect of detector response (blue line), the deviations between the theory and measurement are still huge especially for large angles. However, the difference between the rates and the rates corrected for random coincident events are smaller than in the previous measurement run. In order to achieve further improvements and also to avoid the line of sight effect, which leads to an increase of events from photons going directly from the source into the LaBr₃ detector especially for angles larger 90° , it was decided to construct two collimators.

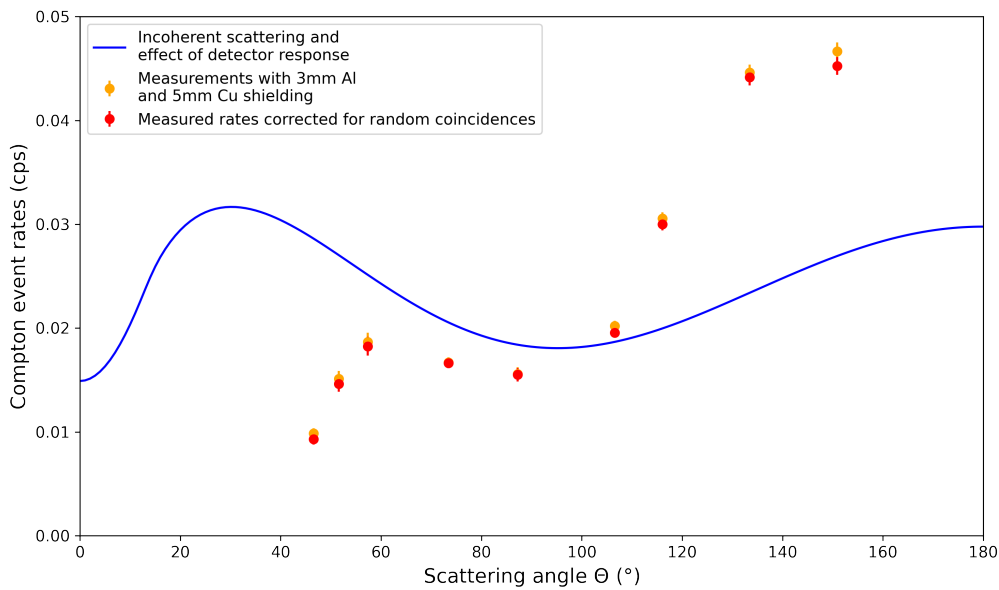


Figure 3.26 Measurements with 5 mm Cu and 3 mm Al shielding: Compton Event rates depending on the scattering angle Θ .

The Compton event rates from the measurement are illustrated by orange dots. The Compton event rates corrected for random coincidences (red dots) for all angles were fitted with the incoherent Compton scattering cross-section including the effect of detector response (blue line), the deviations between the theory and measurement are still huge especially for large angles.

3.5.2.4 Measurement run with Collimator and 3 mm Aluminium Shielding

In order to achieve further improvements, two collimators were constructed, one for measurements at angles smaller than and one for angles larger than 90° . Both have a hole with a diameter of 6 mm. Since for the measurements at angles larger than 90° the collimator has a larger distance to the SDD module, the source with the higher activity (source 2, see 3.3) is used for all measurements. A photograph of the Collimator with the source inside is shown in the lower right part of **Fig: 3.17** for angles larger 90° . The positions of the source are presented in **Fig: 3.8** schematically. As in the previous measurement run, the distance between the source and the SDD module is not the same for measurements at small and large angles. Therefore, the rates must be normalised accordingly. The 3 mm Al shielding was added in front of the collimator as in the measurement described in the previous sections. The scattering angles between the LaBr_3 detector and the beam axis experimentally performed during the measurement run in the setup with collimators and 3 mm Al shielding in front are given in equation 3.4.

$$\Theta \in [46.5, 51.6, 57.3, 73.5, 87.2, 106.5, 116.1, 133.5, 150.9] \quad (3.4)$$

The evaluation procedure was the same as that described in the previous two sections. The Compton event rates corrected for random coincidences (red dots) are illustrated for all angles in **Fig: 3.27**. They were fitted with the incoherent scattering cross-section including the effect of detector response (blue line). The difference between the rates and the rates corrected for random coincident events are now not visible anymore, the red dots overlap the orange dots. However, the deviations between the theory and measurement are still huge especially for large angles.

In the course of the development of the setup described above, some improvements could

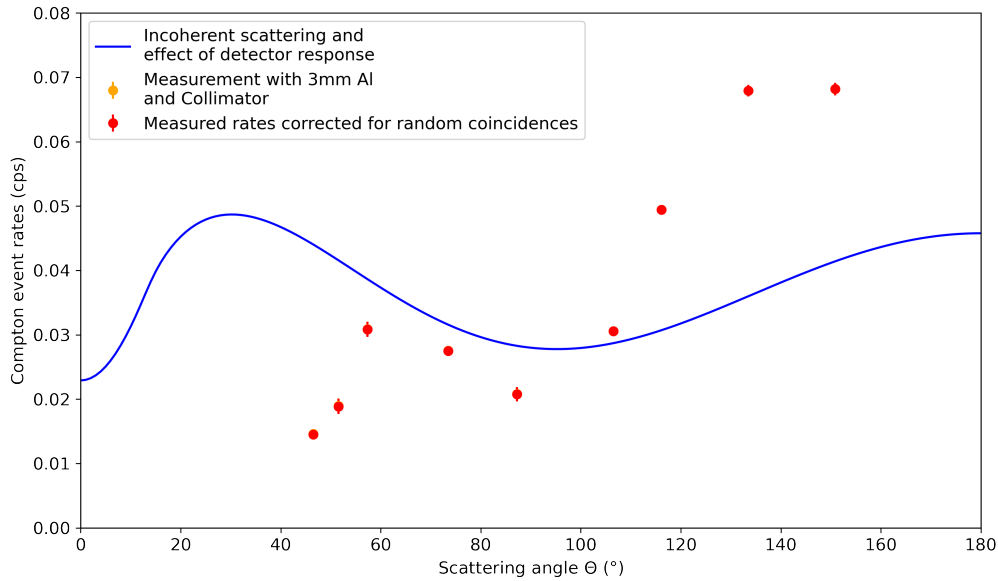


Figure 3.27 Measurements with Collimator and 3 mm Al Shielding: Compton Event rates depending on the scattering angle Θ .

The Compton event rates corrected for random coincidences are illustrated as red dots. They were fitted for all angles with the incoherent scattering cross-section considering the effect of detector response (blue line). The difference between the rates and the rates corrected for random coincident events are now not visible anymore. The deviations between the theory and measurement are still huge especially for large angles.

be achieved, but the results still deviate strongly from those predicted of the theory. To avoid shielding through the PCB hosting the SDD module, which could play a role, the setup was modified. The measurements in the rearranged setup are presented in section 3.5.3. At the same time, simulations of a simplified setup were carried out, which are described in section 3.6.

3.5.3 Measurement Run in the Rearranged Setup

The PCB hosting the SDD module could act as shielding between the SDD module and the LaBr₃ detector. An estimation of the attenuation through 1.8 mm PCB is shown in right part of **Fig: 3.28**, in the left part a photography of the PCB hosting the SDD module is presented and the attenuation through the shielding is sketched schematically. For the calculation of the transmission probability, a continuous plate of PCB with a thickness of 1.8 mm, made of carbon was assumed. This means that depending on the scattering angle of the photon, the path through the PCB for angles larger than 0° is correspondingly longer, shown schematically in the sketch.

The setup was rearranged so that, on the one hand, the collimator is permanently mounted at only one position, hosting the source inside and, on the other hand, the LaBr₃ detector can be rotated so that it is not shielded from the PCB. The rearranged setup is shown schematically in **Fig: 3.9** for determining the angles. The collimator from the previous measurement run for angles larger than 90° was used. Since the distance between the source and the SDD was further increased, the diameter of the collimator hole was increased to 12 mm. The Compton event rates are nevertheless very low, so that a measurement lasted about 5 days. Therefore, the number of measurements within the run was reduced. A

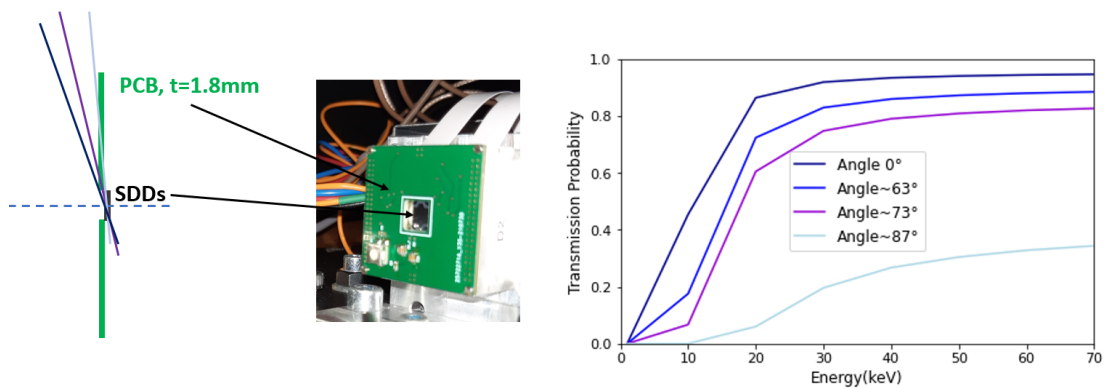


Figure 3.28 Estimation of the attenuation through 1.8 mm PCB.

The estimation of the attenuation through 1.8 mm PCB, hosting the SDD module, is illustrated.

Left: Depending on the scattering angle of the photon, the path through the PCB for angles larger than 0° is correspondingly longer. A schematic sketch is shown (not to scale)

Middle: A photograph of the PCB hosting the SDD module is presented.

Right: An estimation of the attenuation through 1.8mm PCB is shown. For the calculation of the transmission probability, a continuous plate of PCB with a thickness of 1.8mm, made of carbon was assumed.

photograph of the rearranged setup is shown in **Fig: 3.29**. The range of the angles between the LaBr_3 detector and the beam axis experimentally performed during the measurement run is restricted by the size of dark-box, the size of the LaBr_3 detector and the position of the collimator. It is illustrated as range between the orange lines.

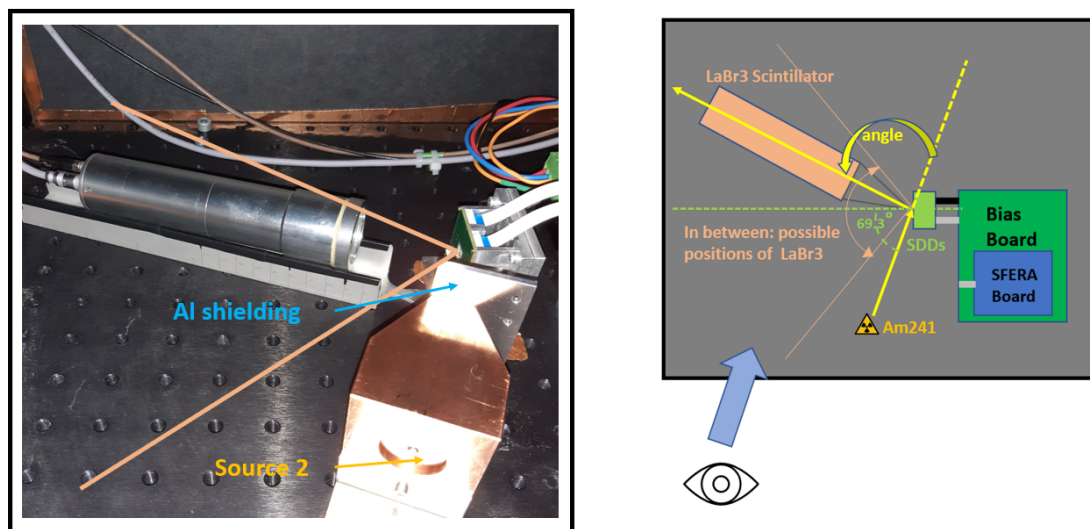


Figure 3.29 Rearranged setup, Collimator with 3 mm Al shielding.

The collimator with 3 mm Al shielding is shown in the rearranged setup. The collimator is permanently mounted with the source inside and the LaBr_3 detector can be rotated so that it is not shielded from the PCB. The rearranged setup is shown schematically in the right part of the figure. The photograph was taken in direction of the blue arrow. The collimator form the previous measurement run for angles larger than 90° was used. The diameter of the collimator hole was increased to 12 mm. The range of the angles between the LaBr_3 detector and the beam axis experimentally performed during the measurement run is restricted by the size of the dark-box and the position of the collimator. This is illustrated as range between the orange lines.

The range of scattering angles used during the measurement run in the rearranged setup are given in equation 3.5.

$$\Theta \in [68.99, 74.68, 89.40, 110.66, 131.95, 152.40] \quad (3.5)$$

The evaluation procedure was exactly the same as that described in section 3.4 in the sequence of figures starting with **Fig: 3.11**. The Compton event rates corrected for random coincidences are illustrated as red dots for all angles in **Fig: 3.30**. The data was fitted with the incoherent scattering cross-section including the effect of detector response shown as a blue line. The difference between the theory and measurement are now small, except for angles $< 90^\circ$.

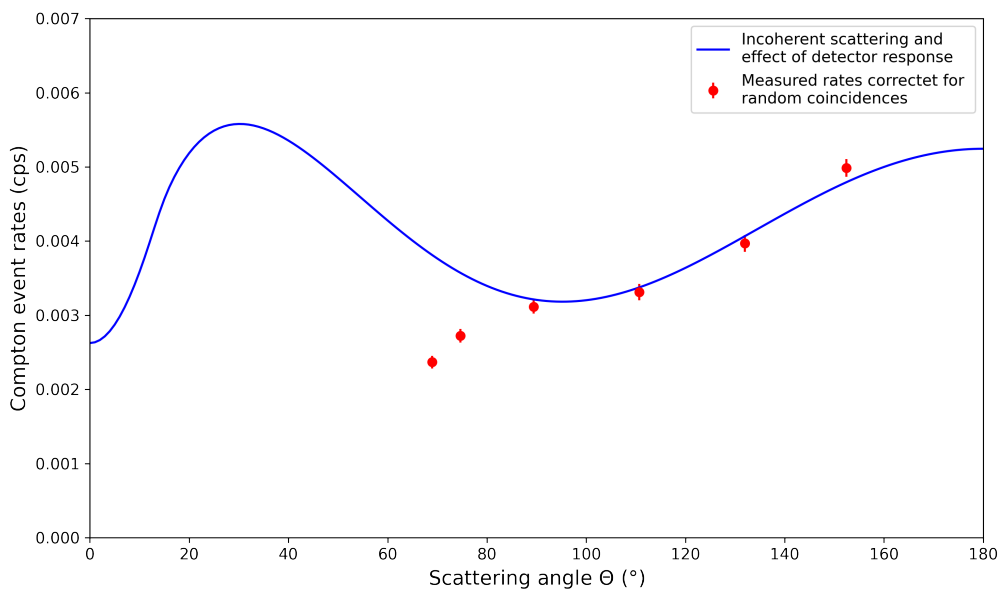


Figure 3.30 Measurements in the Rearranged Setup: Compton Event rates depending on the scattering angle Θ .

The measured rates corrected for random coincidences are illustrated as red dots. They were fitted for all angles with the incoherent scattering cross-section considering the effect of detector response (blue line). The difference between the theory and measurement are now small, except for angles $< 90^\circ$.

In order to explore the possibility of reducing the energy threshold in the SDDs, different settings of the CAEN digitizer (see [5]) were investigated, performing measurements with the ^{55}Fe source analogously to the measurement described above in section 3.5.1. The only possibility found, was to lower the energy threshold in the digitizer from 100 lsb to 50 lsb. With this setting, the ^{55}Fe spectra and the resolutions FWHM in eV of the SDD were determined first. The calibrated spectra for all channels are presented in the left part of **Fig: 3.31**. The spectral resolution FWHM is around 446 eV, shown in the right part of **Fig: 3.31**, which is worse than at the beginning of the measurements. The Si escape peak is visible weakly. Moreover, the spectra of all channels don't match well.

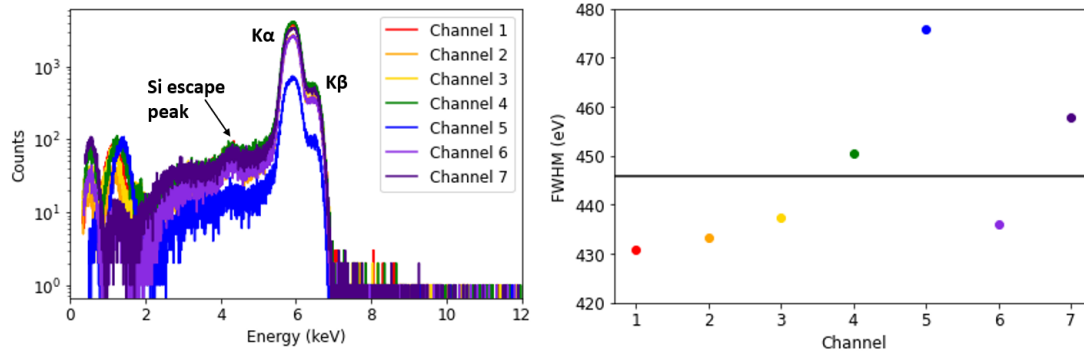


Figure 3.31 Calibrated ^{55}Fe spectra and Resolutions for all SDD channels.

The X-ray lines have energies of $E_{K\alpha}=5.90$ keV and $E_{K\beta}=6.49$ keV and were used for detector calibration and determination of the resolution as before.

Left: Calibrated ^{55}Fe spectra for all channels, the $E_{K\alpha}$ peak at 5.90 keV and the $E_{K\beta}$ peak at 6.49 keV are shown. The Si escape peak is visible weakly. The spectra of all channels don't match well. The separation of the peaks is only weakly resolved.

Right: The spectral resolution FWHM, determined in eV, is illustrated depending on the channel. The mean FWHM is ~ 446 eV, which is much worse than in the beginning of the measurements.

The measurements at the angles $\sim 69^\circ$ and $\sim 75^\circ$ were repeated with a reduced energy threshold in the digitizer of 50 lsb instead of 100 lsb which leads to more noise in the resulting spectra. By lowering the energy threshold in the digitizer, the lower limit of the energy cut for the two measurements could be reduced from 3.5 keV to ~ 2 keV. This allows more Compton events to be taken into account. The result is shown in **Fig: 3.32**.

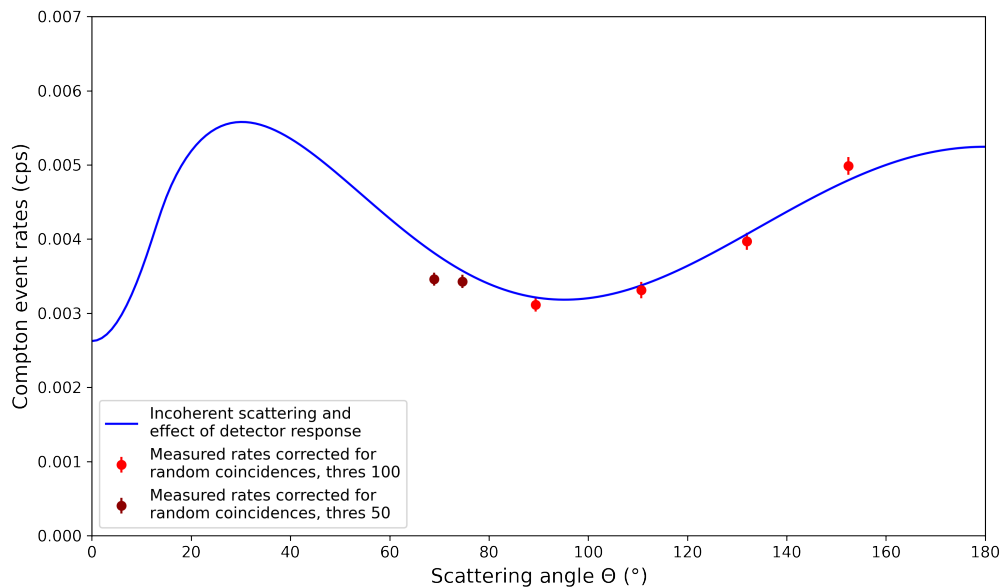


Figure 3.32 Measurements (final) in the rearranged Setup: Compton Event rates depending on the scattering angle Θ .

The Compton event rates corrected for random coincidences are illustrated as red dots, the results for the repeated measurements with lower energy threshold in the digitizer as dark-red dots. The data points were fitted with the incoherent scattering cross-section considering the effect of detector response (blue line). The difference between the theory and measurement are now small, except for angle $\sim 69^\circ$.

The energy threshold which is needed to resolve a scattering angle depending on the energy can be determined by calculating the energy of the electron absorbed in the SDD for Compton scattering, presented in section 1.3.2 The result is the dark blue line in **Fig: 3.33**. The 3σ value can be calculated from the resolution which was given in $\text{FWHM} \sim 446 \text{ eV}$, by $3\sigma = 3 \cdot \text{FWHM} / 2.35$. The energy threshold required to resolve e.g. an angle of 70° is $\sim 3.2 \text{ keV}$, shown in the right part of **Fig: 3.33**, can be determined by following the violet arrows. The blue band illustrates the calculated energy of the electron absorbed in the SDD for Compton scattering \pm the 3σ value of the resolution.

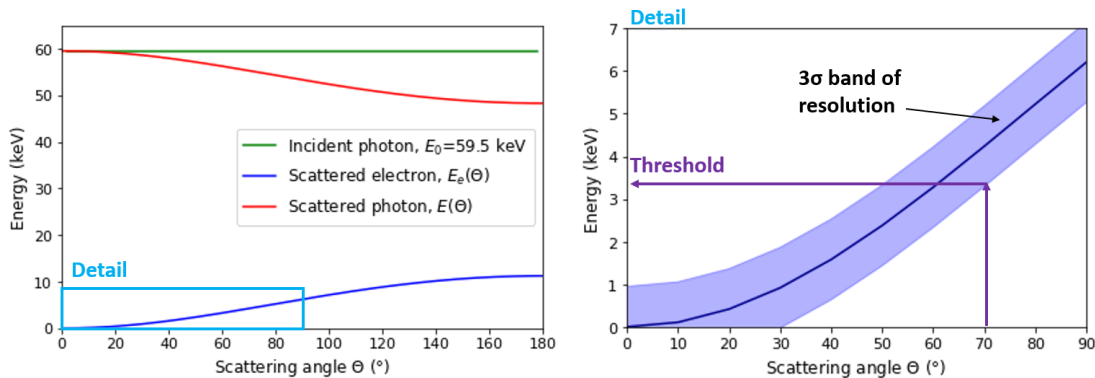


Figure 3.33 Required Energy Threshold depending on the scattering angle Θ .

The energy threshold which is required to resolve a scattering angle depending on the energy is shown.

Left: The energy of the electron absorbed in the SDD for Compton scattering can be calculated (see section 1.3.2) The result is the blue line.

Right: A detail of the left part is shown. The energy of the electron absorbed in the SDD for Compton scattering (blue line) is illustrated for small scattering angles. The 3σ value can be calculated from the resolution. The energy threshold required to resolve e.g. an angle of 70° is $\sim 3.2 \text{ keV}$. It can be determined by following the violet arrows. The blue band illustrates the calculated energy of the electron absorbed in the SDD for Compton scattering \pm the 3σ value of the resolution.

A good energy resolution of the SDDs, leading to a lower energy threshold, is therefore crucial to resolve small scattering angles in particular. However, the angle dependent Θ differential cross-section for incoherent scattering according to the modified Klein-Nishina equation could be reproduced in the angle range between $\sim 75^\circ$ and $\sim 152^\circ$. The results are discussed in section 3.7

3.6 Simulations

As mentioned above, simulations were carried out in parallel with the measurements in the rearranged setup. They are presented in this section, after a brief introduction to Geant4 specifically in relation to settings used during the simulations in this work. The analysis chain is also briefly described. Then the simulations to investigate the influence of the lower energy threshold of the SDDs are presented, followed by the simulations to investigate the reduced number of counts in the angular range around an angle of 90° .

Simulations of detectors and their properties are common in detector physics. Geant4 (for GEometryANdTracking) is a Monte Carlo tool in a C++ framework for simulating

the passage of particles through matter and their interactions with it [6]. It has been developed and is maintained at CERN and is one of the most used simulation frameworks within the field of particle physics, medical physics, astrophysics and other fields. Geant4 is often used for the development of detectors and accelerators as well as for the verification of physical models and measurement data.

The user defines the geometry of the setup, including the design of the detector, the surrounding material and the particle source. Therefore, the user constructs volumes of the desired shape of each part of the detector and assigns a material, consisting of chemical elements, to each volume, also compound materials can be created. A database provided by Geant4 contains the properties of all chemical elements. The selection of particles for the simulation is very flexible. The user can choose between all particles of the standard model or create particle types according to his own definition. The required interaction types for the simulation are also selected by the user. It is possible to deactivate processes or define new ones. The implemented physics is applicable from 250 eV up to several 10^{15} eV. For simplification, the user can choose between main groups of physical processes. That are e.g. particle decay processes, electromagnetic interactions, photoleptonic interactions, hadronic interactions or solid state physics. Each initial particle and the secondary particles produced during an event are simulated. The user defines the number of events. An event begins with the generation of a first particle in the source and ends with the tracking of all particles until they are absorbed or leave the region of interest. All information about the individual interactions, including position, time, type of interaction, deposited energy, particle type, etc. can be stored.

In the context of this work, Geant4 is used to simulate a Compton scattering experiment in a simplified setup, according to the characterisation measurements, as mentioned above. The software version used for this work is Geant4 10.7.4. The settings used for the implemented setup and for the simulations are described in the following.

Geometry

The simplified setup implemented for simulations contains only the LaBr₃ detector and the SDD module. The distance between the detectors is set to 54 mm, according to the first measurement without shielding. The LaBr₃ detector is implemented as a cylinder with a diameter and a thickness of 1 inch (2.54 cm). The SDD module has been implemented in two different ways. A choice can be made between a geometry consisting of seven hexagons (combined to one detector for read out), as described in section 2.2.1, and a cylinder with a height of 0.45 mm, which is equal to the thickness of the SDDs. The radius can be varied. The two geometries are illustrated in **Fig: 3.34**.

The angle between the LaBr₃ detector and the beam axis can be varied by a messenger. During the simulations, the angles were varied in a range between 0° and 180°. At an angle of 0°, the detector is aligned perpendicular to the SDD module and is located on the other side of the SDDs than the source. The geometry of the setup consisting of the SDDs (seven hexagonal pixels) and the LaBr₃ is shown in **Fig: 3.35**. The materials are implemented as mentioned above.

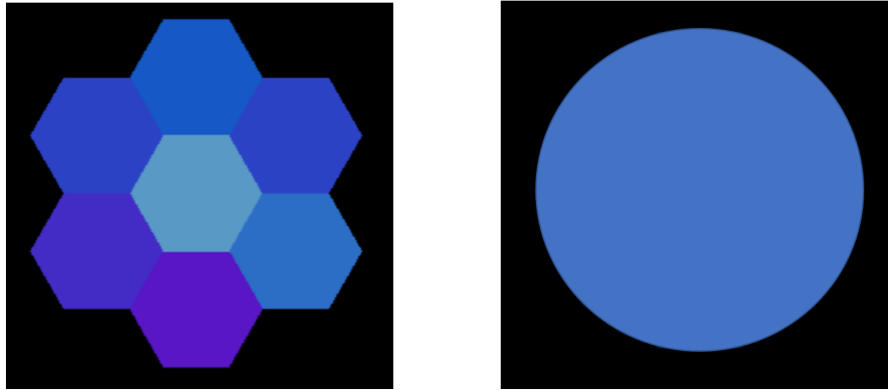


Figure 3.34 Geometry of the SDDs used for Simulations.

The SDD module has been implemented in two different ways.

Left: One possibility is a geometry consisting of seven hexagons, as described in section 2.2.1. The thickness is 0.45 mm.

Right: The second possibility is a cylinder with a height of 0.45 mm, which is equal to the thickness of the SDDs, while the radius can be varied (not to scale).

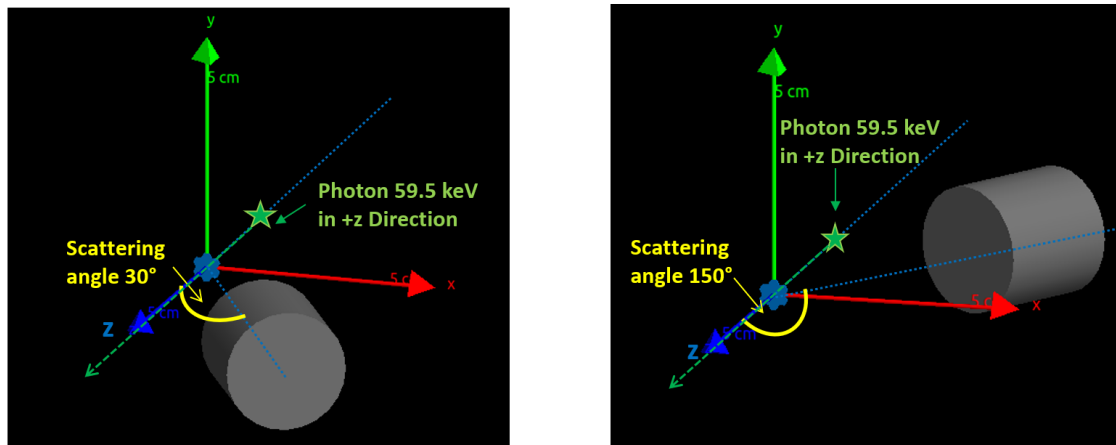


Figure 3.35 Setup for Simulation and source position, two angles exemplary.

The seven hexagonal SDDs are illustrated in blue. The angle (scattering angle) between the LaBr_3 detector (grey), and the beam axis can be varied by a messenger. During the simulations, the angles (scattering angles) were varied in a range between 0° and 180° .

Left: At an angle of 0° , the detector is aligned perpendicular to the SDD module and is located on the other side of the SDDs than the source, indicated by the green star, exemplary the angle 30° is shown for angles smaller 90° . The photon with an energy of 59.5 keV propagates in positive z-direction.

Right: At an angle of 180° , the detector is aligned perpendicular to the SDD module and is located on the same side of the SDDs as the source, indicated by the green star, exemplary the angle 150° is shown for angles larger 90° . The photon with an energy of 59.5 keV propagates in positive z-direction.

Physics list

In the so-called physics list, the particles are defined and also the physical processes which are considered during the simulation. The **G4EmLivermorePolarizedPhysics** constructor, a predefined physics list for the low energy range (250 eV to 100 GeV) provided by Geant4 is used during the simulations carried out in the scope of this work. It contains electromagnetic interactions, including polarized gamma models.

Particle source

One particle source emitting a perfect photon beam is used for the simulations. The photon has an initial energy of 59.5 keV for comparability with the measurements where an ^{241}Am source was used. The beam then consists of 7 million photons that strike the SDDs perpendicular to the surface and in the center of the silicon detector. The position of the incident photons is shown in **Fig: 3.35**. Each photon of the beam starts at the position indicated by the green star and propagates in positive z-direction.

Detector response

In order to get a more realistic description of the detector, the implementation of the detector response is required. This can be done by Geant4 too by an external user defined description of the detector resolution. However, in the scope of this thesis it was decided to consider the detector response in a post process after the simulation by a python program which also evaluates the data. The advantage is the possibility to investigate effects of the detector resolution without having to run the simulations multiple times. The detector response is required for both detectors, the SDDs and the LaBr_3 , as they both have a limited energy and position resolution and a lower energy threshold. The detector resolution was described in section 2.2.4. The energy dependent values were illustrated in **Fig: 2.7** for the LaBr_3 and in **Fig: 2.8** for the SDDs. The detector response i.e. the energy resolutions of the two detectors are now implemented as Gaussian uncertainties. The width of the Gaussian of each detector is energy dependent. According to this Gaussian distribution, the energy deposit for each event is shifted by a random value.

The energy thresholds of the detectors are set differently to investigate the influence. If the total energy deposit per event is lower than the energy threshold of the respective detector, the event is not considered.

Analysis chain

The Analysis chain is similar to that described in section 3.4 with slight differences. It is illustrated schematically in **Fig: 3.36**, the differences are presented in the following. The process of the analysis chain is run through for each angle during the evaluation of each simulation.

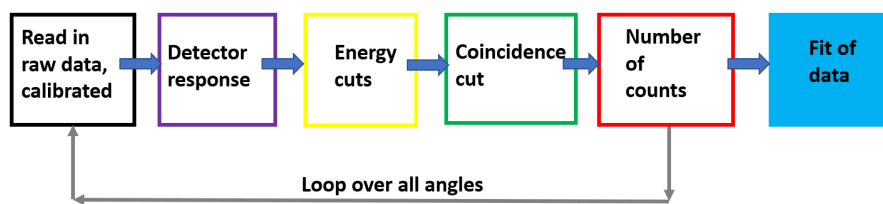


Figure 3.36 Analysis chain for Simulations.

The Analysis chain is similar to that described in section 3.4 with slight differences. The process of the analysis chain is run through for each angle during the evaluation of each simulation.

- **Read in of the raw data.**

First, the data from the simulation are read in, but a calibration is not necessary, the energies are given in MeV. In contrast to the measurement, the spectrum in the SDD module is given for each angle combined for all hexagons.

- **Considering the detector response.**

As a second step the detector response is considered as described above.

- **Coincidence cut.**

The coincidence cut is performed after the energy cut. Each incident photon has its own event number, therefore the coincidence cut can be done by searching for events in both detectors which have the same event number.

- **Number of counts.**

The result of the previous steps is the number of coincident counts in the given energy range. The lower energy range bound sets the energy threshold. The determination of the rates is not necessary, as for each angle a beam of 7 million photons was considered. The uncertainties of the counts (according to Poisson) are calculated by the square-root of the number of counts.

After running through the analysis chain for each angle, the number of counts are given as data-points depending on the scattering angle Θ . Finally a fit of the data is performed as described in section 3.4.

Investigation of the lower Energy Threshold in the SDDs

To investigate the lower energy threshold in the SDDs, the setup for simulation was implemented as described above, using the geometry of the seven hexagonal SDDs. In the analysis with python, the lower energy threshold in the SDDs was set to 0 keV first, then to 2 keV and to 3.5 keV, which was chosen analog to the settings during the measurements, described in the previous sections. The change of the spectra in the LaBr_3 detector and the SDD module during the analysis is shown and explained in **Fig: 3.37** and **Fig: 3.38** exemplary for an angle of 110° .

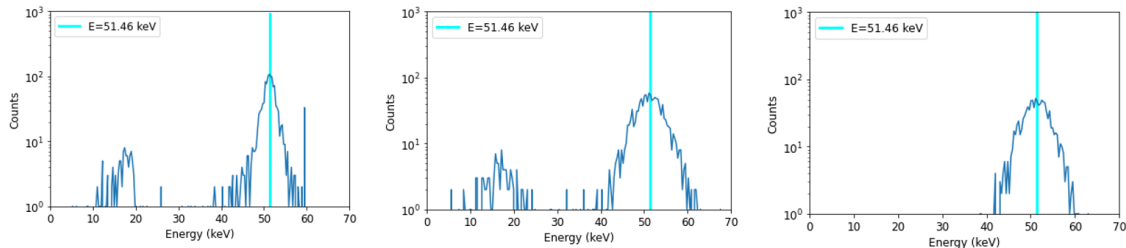


Figure 3.37 Evaluation of a LaBr_3 spectrum from Simulation, exemplary for $\Theta=110^\circ$.

The change of the spectrum in the LaBr_3 detector during the analysis is shown exemplary for simulations with threshold 0 keV.

Left: The spectrum in the LaBr_3 after read in is shown. A line at 59.5 keV is clearly visible as well as a peak around the calculated energy of the scattered photon for an angle of $\Theta=110^\circ$.

Middle: The spectrum in the LaBr_3 after considering the detector response is shown. The peak around the calculated energy of the scattered photon for an angle of $\Theta=110^\circ$ is now broader.

Right: The spectrum in the LaBr_3 after considering the effect of detector response and after Energy and coincidence cut is shown. The peak around the calculated energy of the scattered photon for an angle of $\Theta=110^\circ$ is visible.

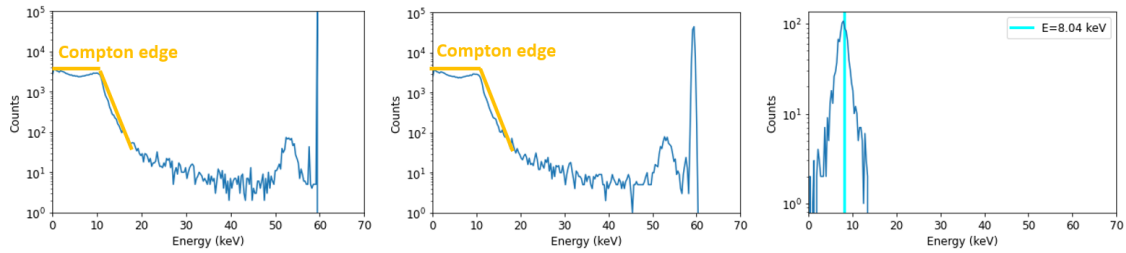


Figure 3.38 Evaluation of a SDD spectrum from Simulation, exemplary for $\Theta=110^\circ$.

The change of the spectrum in the SDD module during the analysis is shown for simulations with threshold 0 keV.

Left: The spectrum in the SDD module after read in is shown, the Compton edge around 11.3 keV is visible and also a line at 59.5 keV .

Middle: The spectrum in the SDD module after considering the effect of detector response is shown, the Compton edge around 11.3 keV is visible and also a line at 59.5 keV.

Right: The spectrum in the SDD module after considering the detector response and after energy and coincidence cut is shown, now only the peak around the calculated energy of the scattered electron for an angle of $\Theta=110^\circ$ is visible.

The results of the investigation of the influence of the lower threshold in the SDD module are shown in **Fig: 3.39**, where the three different thresholds 0 keV (black), 2 keV (dark green) and 3.5 keV (light green) were considered. It can be seen that even for the 0 keV threshold, the number of Compton events from simulation does not agree well with the fit in the range of angles $\Theta < 20^\circ$ and around 90° . In the range of angles $\Theta < 20^\circ$ the number of events is higher and around 90° lower than predicted. The difference which concerns small angles is possibly due to a different model for the correction factor $S_H(E_0, \Theta)$ for incoherent scattering, see 1.7, or the detector response is not modelled accurately enough. Since both effects affect only very small scattering angles, this disagreement was not further investigated.

Comparing the different thresholds, it can be seen that the possibility to resolve a certain angle gets worse with a higher threshold, similar to the measurements performed in the rearranged setup. There are similarities visible between the results of the simulation and the results of the measurements where the source was placed so that the photons hit the SDD module perpendicularly. This meant that the photons had to travel a different distance in the PCB material during the measurement, as illustrated in **Fig: 3.28**. Therefore, it will be investigated in the following whether the different length of the path of the photons through the SDD module itself has a non-negligible influence on the number of Compton events in the angular range around 90° .

However, the results of the investigation of the influence of the lower threshold in the SDD module via simulation confirm the results from the measurements. The lower energy threshold is of decisive importance for the resolution of smaller scattering angles. Since the energy threshold is related to the resolution of the detector, a good detector resolution is very important.

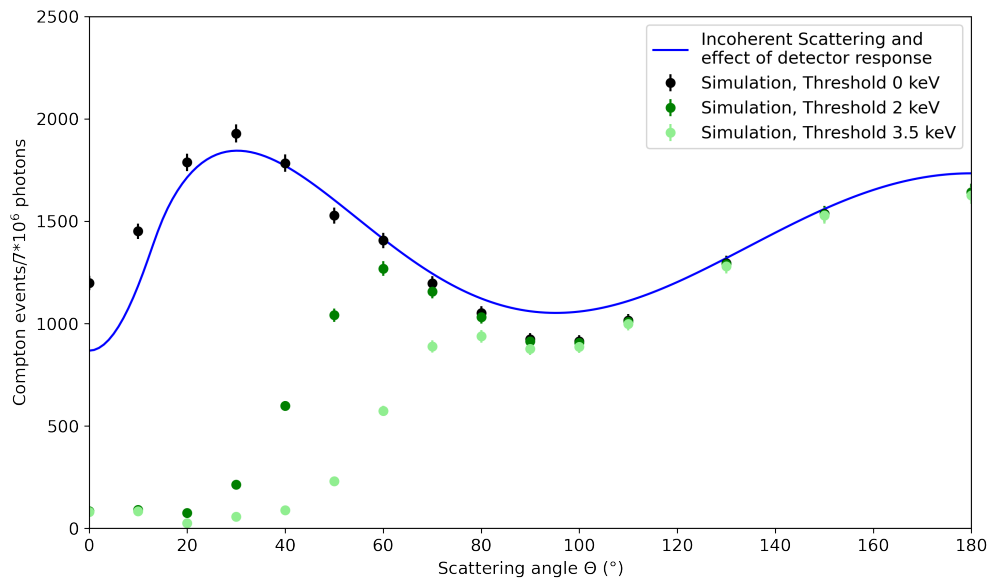


Figure 3.39 Influence of the lower Energy Threshold in the SDD module.

The results of the investigation of the influence of the lower threshold in the SDD module are shown. Three different thresholds 0 keV (black), 2 keV (dark green) and 3.5 keV (light green) were considered. Even for the 0 keV threshold, the number of Compton events from simulation does not agree well with the fit (in blue) in the range of angles $\Theta < 20^\circ$ and around 90° . In the range of angles $\Theta < 20^\circ$ the number of events is higher and around 90° lower than predicted. Comparing the different thresholds, it can be seen that the possibility to resolve a certain angle gets worse with a higher threshold, similar to the measurements performed in the rearranged setup.

Investigation of the reduced Number of Compton Events in the angular range around 90°

To investigate the the reduced number of Compton events in the angular range around 90° , the setup for simulation was implemented as described above, but now using the geometry of a cylinder with a radius equal to the thickness (0.45 mm), this makes the path in the SDD module independent from the scattering angle. The lower energy threshold in the SDD module was set to 0 keV. The result is shown in **Fig: 3.40**. The number of Compton events from simulation agree well with the fit (in blue) in the range of angles around 90° . But in the range of small and large angles are still deviations.

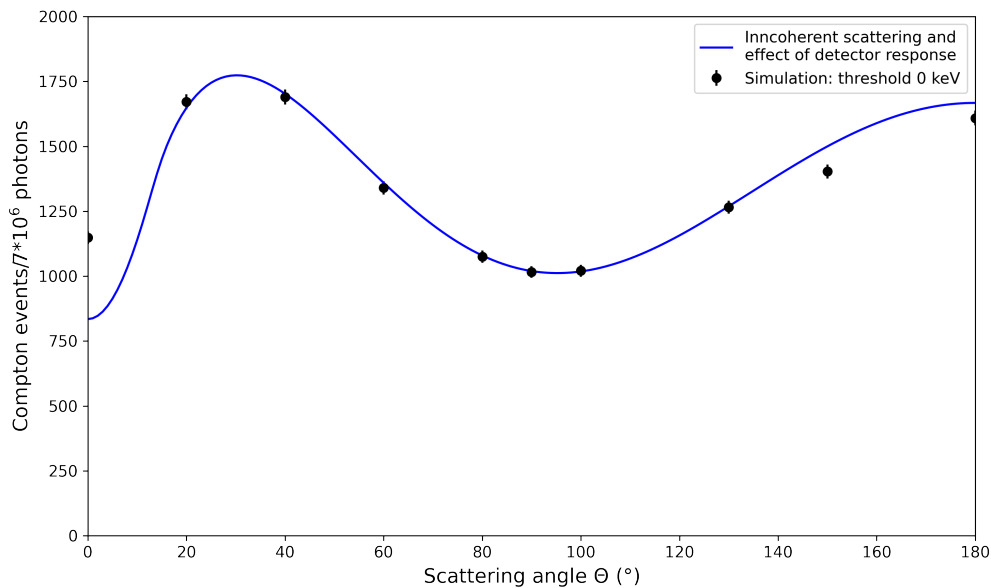


Figure 3.40 Investigation of the reduced Number of Compton Events in the angular range around 90°

The results of the investigation of the reduced number of Compton events in the angular range around 90° are shown. The setup for simulation was the same, but the geometry of the SDDs was implemented as a cylinder with a radius equal to the thickness (0.45mm). The lower energy threshold in the SDD module was set to 0 keV. The number of Compton events from simulation agree well with the fit (in blue) in the range of angles around 90° , but not in the range of small and large angles.

It can be concluded that the length of the path of the incident photon through the silicon of the SDD module itself is important. A longer path leads to a lower number of Compton events. This influence is particularly noticeable at scattering angles of 90° . The results are discussed in the following section 3.7.

3.7 Summary and Discussion

The goal of this thesis is the characterization of the seven pixel SDD module, the prototype for the ComPol-IOV mission. The procedure of the characterization and the results are described in detail above in this chapter, starting with the motivation of the characterization measurements in section 3.1 and a detailed description of the setup in section 3.2. The performed characterization measurements are presented in section 3.5 and the simulations carried out with Geant4 are described in section 3.6.

The Compton scattering experiments performed in the rearranged setup could reproduce the angle dependent Θ -differential cross-section for incoherent scattering according to the modified Klein-Nishina equation in the angle range between $\sim 75^\circ$ and $\sim 152^\circ$. Furthermore it could be shown that a good energy resolution of the SDDs, leading to a lower energy threshold, is crucial to resolve small scattering angles in particular. The results of the investigation of the influence of the lower threshold in the SDD module by means of simulation confirm these results from the measurements. Two measurements with a ^{55}Fe source at different times, the second 8 month after the first, lead to different detector resolutions. The detector resolution FWHM changed from ~ 252 eV to ~ 445 eV. It is not necessarily the case that the system has deteriorated, there is probably an external influence, as the equipment in the laboratory has been rebuilt and the setup in the dark-

box has been changed. The position of the dark-box has also been changed. In addition, it turned out, that the length of the path of the incident photon through any material, e.g. the PCB or even the silicon of the SDD module itself, is important. A longer path leads to a lower number of Compton events. The results of the measurements and the simulations, especially concerning their impact on the ComPol mission, are discussed in the following.

Impacts of the Results on the ComPol Mission.

The influence of the lower energy threshold in the SDDs has the strongest effect at low energies. The lower the energy of the incident photon, the lower the energy of the Compton edge and the energy of the photons where the polarization dependency is the highest.

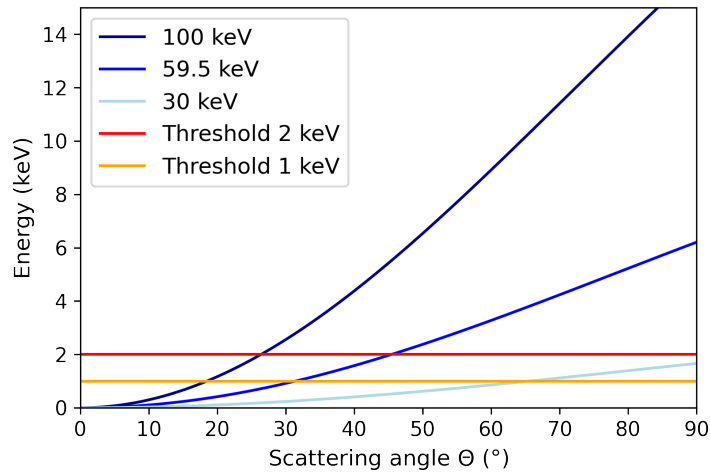


Figure 3.41 Influence of the Energy Threshold on the detectable Energy Range.

The energies of the electrons absorbed in the SDD for Compton scattering are shown for small angles. The energies of the electrons were calculated from the energies of the initial photons, see section 1.3.2. The energies of the initial photons are set to 30 keV, 59.5 keV and 100 keV. It is visible that events with energies of 30 keV are not detectable for a lower energy threshold of 2 keV (red horizontal line). The lower energy threshold of 1 keV (orange horizontal line) is shown also, as a threshold of 1 keV was assumed in the sensitivity study performed by Matthias Meier.

The influence of the energy threshold on the detectable energy range is shown in **Fig:** 3.41. Exemplary three different energies (30 keV, 60 keV and 100 keV) are shown in **Fig:** 3.41, illustrating incident photons in a Compton scattering process. The energies of the electron absorbed in the SDD for Compton scattering are presented exemplary for these three energies of the initial photons and only for small scattering angles. The energies of the electrons were calculated from the energies of the initial photons, see section 1.3.2. It is visible, that events with energies of 30 keV are not detectable for a lower energy threshold of 2 keV (red horizontal line). The value 2 keV is chosen here because it is the current limit with the data acquisition system that is foreseen for the SDD readout. A lower energy threshold of 1 keV (orange horizontal line) is shown also which was assumed in the sensitivity study performed by Matthias Meier [36].

The 3σ value of resolution, which was shown in **Fig:** 3.33, was not considered here. Assuming a lower energy threshold of 3.5 keV, it would be even worse. Also fewer Compton events remain for initial photons with energies higher 30 keV that can subsequently be

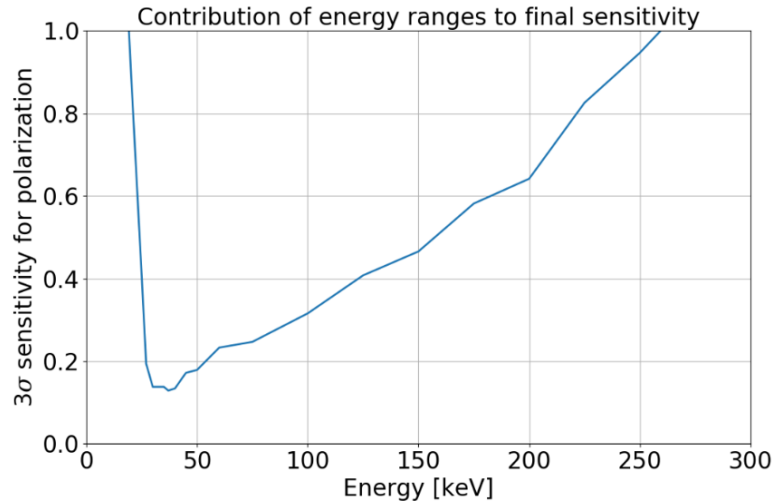


Figure 3.42 Minimum Detectable Polarization, Threshold 1 keV.

The Minimum Detectable Polarization, for one year observation is plotted over the energy. (Taken from [36]). The results are obtained by simulations (threshold 1 keV) with mono-energetic photon beams, weighted by the spectrum of Cygnus X-1. The blue line illustrates the smallest degree of polarization that can be measured depending on the energy. So far it was always assumed that the most sensitive range starts at ~ 30 keV. If the threshold is higher, small energies will not be considered and the cutoff will be shifted to the right by approximately 10-20 keV.

subjected to polarization analysis. However, the relative energy resolution gets better with increasing energy, even though the absolute energy resolution gets worse with increasing energy. During the measurements, the CAEN digitizer was mostly used at a setting of 100 lsb for the threshold, resulting in an energy threshold of 3.5 keV. This could be lowered to 2 keV by setting the threshold in the digitizer to 50 lsb. However, the latest measurements with the data acquisition system that will be used for the final system resulted in a lower threshold of 2 keV, therefore the lower energy threshold in **Fig: 3.33** was set to 2 keV for illustration.

So far in the the sensitivity study performed by Matthias Meier [36] always a threshold of 1 keV in the SDD was assumed. From that the sensitivity results shown in **Fig: 3.42** were received. The Minimum Detectable Polarization, the 3σ sensitivity, for one year observation is plotted over the energy. The photon beam in the simulation was mono-energetic but weighted by the spectrum of Cygnus X-1. The figure is taken from [36], for details see there. The blue line illustrates the smallest degree of polarization that can be measured depending on the energy. The most sensitive range was so far always assumed to start at ~ 30 keV. If the threshold is higher, small energies will be not considered and the cutoff will be shifted to the right by approximately 10-20 keV.

The ComPol mission will carry out polarization measurements. Due to geometric reasons and the polarization dependency of Compton scattering, the best polarization is achieved for a cut on the scattering angles Θ between 55° and 83° [36]. Therefore in addition the impact of the lower energy threshold in the SDD, the shielding by the SDD itself could be important, since the Compton events are most strongly shielded at scattering angles where the polarisation is maximum (90°), see **Fig:1.8**, especially at low energies. To avoid this effect, the geometry of the setup could be redesigned. By redesigning, it might be possible to reduce the self-absorption of the SDD and therefore gain sensitivity in the low energy range.

Conclusion and Outlook

Black holes, neutron stars and white dwarfs are fascinating objects in the universe. To better understand these compact objects, great efforts have been made in recent decades. But some questions are still unanswered. The Compton Polarimeter (ComPol) is a CubeSat mission. Its aim is to study the spectrum and polarization of the black hole binary system Cygnus X-1 over a period of at least one year in the hard X-ray range to gain new insights into its geometry, accretion disk properties, X-ray emission mechanisms and other features. An adapted instrument is currently being prepared for an in-orbit verification mission on an external platform aboard the International Space Station (ComPol-IOV). The launch is planned for the end of 2023. The main objective of ComPol-IOV is to demonstrate the functionality and durability of the instrument in the low earth orbit. Besides that, it allows for a in-orbit background study and for developing data acquisition routines using real data.

The focus of this thesis is the characterization of the Silicon drift detector module, the prototype for the ComPol-IOV mission. The physical motivation for the characterization measurements is to reproduce the angle dependent Θ -differential cross-section for incoherent scattering according to the modified Klein-Nishina equation by a Compton scattering experiment. Thereby the used setup consists of the SDD module, originally designed for the TRISTAN experiment, as scatter target and a commercially available Lanthanum(III)Bromide detector as calorimeter. The angular dependence of the Compton scattering is experimentally performed by changing the angle between the beam axis of the radioactive source and the calorimeter (the LaBr₃ Detector), which lies on a rotatable part (U-profile) with a pivot point below the center of the SDD. In addition, simulations with Geant4 were carried out implementing a simplified setup, consisting of only the two detectors.

Characterization measurements were performed in an evolving setup with different shieldings and different holders for the two ²⁴¹Am sources with different activities that were used. The first measurements showed that the PCB hosting the SDD module plays a non-negligible role for measurements at larger angles. Therefore the setup was rearranged so that, on the one hand, the collimator is permanently mounted at only one position, hosting the source inside, and on the other hand, the LaBr₃ detector can be rotated so that it is not shielded from the PCB. The Compton scattering experiments performed in this setup could reproduce the angle dependent Θ -differential cross-section for incoherent scattering in the angle range between $\sim 75^\circ$ and $\sim 152^\circ$. Furthermore, it could be shown that a good energy resolution of the SDDs, leading to a lower energy threshold, is crucial to resolve small scattering angles in particular. The results of the investigation of the influence of the lower threshold in the SDD module by means of simulation, carried out in parallel to the measurements in the rearranged setup confirm these results from the measurements. In addition, it turned out as a result from the simulations, that also the

length of the path of the photon through the Silicon of the SDD module, is of influence. A longer path at larger scattering angles leads to a reduced number of Compton events.

The ComPol mission will carry out polarization measurements. Due to geometric reasons and the polarization dependency of Compton scattering, the best polarization is achieved for a cut on the scattering angles Θ between 55° and 83° . Therefore, the absorption of the SDD itself is probably reducing the sensitivity. This could be important, because the Compton events are most strongly shielded at scattering angles where the polarization signal is strongest (at $\sim 90^\circ$). Especially low energies are affected by this.

The influence of the lower energy threshold in the SDDs also has the strongest effect at low energies. The lower the energy of the incident photon, the lower the energy of the Compton edge and the energy of the photons where the polarization dependency is highest. Therefore, fewer Compton events remain that can subsequently be subjected to polarization analysis. During the measurements, the CAEN digitizer was mostly used at a setting of 100 lsb for the threshold, resulting in an energy threshold of 3.5 keV. This could be lowered to 2 keV by setting the threshold in the digitizer to 50 lsb. However, the data acquisition system planned to be used for ComPol currently shows an energy threshold of 2 keV.

More Compton events at lower energies are expected from Cygnus X-1, so a good resolution and a low energy threshold would be important. By redesigning it might be possible to reduce the self-absorption of the SDD and thus gain sensitivity in the low energy range. This is not crucial for the ComPol-IOV mission. However, insights into the lower energy threshold are expected, which can be compared with expectations from simulations and measurements to provide indications to the final energy threshold and conclusions for future polarization measurements, leading to improvements for the ComPol mission.

Appendix

A.1 Abbreviations and Acronyms

ADC	Analog to Digital Converter
BGR	Background Rate
BH	Black Hole
BHB	Black Hole Binary
CEA	Commissariat à l'Énergie Atomique
ComPol	Compton Polarimeter
CS	Compton Scattering
DAQ	Data Acquisition System
DGS	Dynamical Geometry Software
DPP	Digital Pulse Processor
EC	Electron Capture
FWHM	Full Width at Half Maximum
HSS	High Soft State
IGR	Inner Guard Ring
IOV	In Orbit Verification
IS	Incoherent Scattering
ISS	International Space Station
JFET	Junction Field Effect Transistor
LEO	Low Earth Orbit
LHS	Low Hard State
LRSM	Laboratory for Rapid Space Mission
lsb	least significant bit

MDP	Minimum Detectable Polarization
NNDC	National Nuclear Data Center
PC	Personal Computer
PCB	Printed Circuit Board
PHA	Pulse Height Analysis
PMT	Photo-Multiplier Tube
PSD	Pulse Shape Discrimination
SDD	Silicon drift detector
SiPM	Silicon Photo Multipliers
SNR	Signal to Noise Ration
TUM	Technical University Munich

A.2 Random Coincidence Events and Propagation of Statistical Uncertainties

In general the major source of uncertainties in the performed measurements is given by the statistical uncertainty on the number of counts (according to Poisson, i.e. square-root of number of counts). Additionally uncertainties on the measured time, the scattering angle (position of the screws in the dark-box) and the energy calibration could arise. However, these are assumed to be small and are neglected.

The determination of event rates is done for two detectors, the LaBr₃ scintillator and the SDD, for simplicity the detectors are associated with numbers in the following according to:

Detector1: SDD, total rate R_1 after energy cut before coincidence cut.

Detector2: LaBr₃, total rate R_2 after energy cut before coincidence cut.

The Compton event rate R_{CS} is the same in both detectors. The rates in the LaBr₃ are angle dependent, the angle between the scintillator and the source varies. The rates in the SDDs are not angle dependent, as the position of the SDD wrt the source during a measurement run is the same. The variables and values used in the following equations are explained below the equations.

The rates of random coincidences can be calculated as follows:

$$R_{RC} = 2 \cdot \tau R_{rand,1} R_{rand,2} \quad (\text{A.1})$$

The final rate of all coincident events is given by:

$$R_{final} = R_{CS} + R_{RC} = R_{CS} + 2 \cdot \tau R_{rand,1} R_{rand,2} \quad (\text{A.2})$$

The random rates in the two detectors are:

$$R_{rand,1} = R_1 - R_{CS} \quad \text{and} \quad R_{rand,2} = R_2 - R_{CS} \quad (\text{A.3})$$

Inserting equations A.3 into equation A.2:

$$R_{final} = R_{CS} + 2 \cdot \tau (R_1 - R_{CS})(R_2 - R_{CS}) \quad (\text{A.4})$$

Multiplication and rearranging leads to:

$$R_{final} = R_{CS} + 2 \cdot \tau (R_1 \cdot R_2 - R_{CS} R_1 - R_{CS} R_2 + (R_{CS})^2) \quad (\text{A.5})$$

$$0 = (R_{CS})^2 + (R_{CS})(1/2\tau - R_2 - R_1) + (R_1 \cdot R_2 - R_{final}/2\tau) \quad (\text{A.6})$$

The equation can be simplified by using the following definitions for substituting:

$$a := (1/2\tau - R_2 - R_1) \quad (\text{A.7})$$

and

$$b := (R_1 \cdot R_2 - R_{final}/2\tau) \quad (\text{A.8})$$

Solving for R_{CS} results in the rate of **Compton events considering random coincidences**, where a and b are defined as above derived in equations A.7 and A.8.

$$f := R_{CS} = -a/2 + \sqrt{a^2/4 - b} \quad (\text{A.9})$$

The propagation of statistical uncertainties is defined as:

$$\sigma_{CS} = \sqrt{\sigma_{final}^2 + \sigma_{RC}^2} \quad (\text{A.10})$$

where with $f := R_{RC}$ according to equation A.9, the partial derivatives have to be considered to:

$$\sigma_{RC} = \sqrt{\left(\frac{\partial f}{\partial R_1} \sigma_{rand,1}\right)^2 + \left(\frac{\partial f}{\partial R_2} \sigma_{rand,2}\right)^2 + \left(\frac{\partial f}{\partial R_{final}} \sigma_{final}\right)^2} \quad (\text{A.11})$$

The partial derivatives of the function $f := R_{CS}$ derived above can be calculated by using the chain-rule and considering the definitions of a and b (equations A.7 and A.8) for simplicity.

$$\frac{\partial f}{\partial R_1} = -\frac{1}{2} + \frac{1}{2} \cdot \left(\frac{a^2}{4} - b\right)^{-1/2} \cdot (2/4(a)(-1) - 1 + 0) \quad (\text{A.12})$$

$$= -\frac{1}{2} + \frac{1}{2} \cdot \left(\frac{a^2}{4} - b\right)^{-1/2} \cdot (-1/2(a) - 1) \quad (\text{A.13})$$

$$\frac{\partial f}{\partial R_2} = -\frac{1}{2} + \frac{1}{2} \cdot \left(\frac{a^2}{4} - b\right)^{-1/2} \cdot (2/4(a)(-1) - 1 + 0) \quad (\text{A.14})$$

$$= -\frac{1}{2} + \frac{1}{2} \cdot \left(\frac{a^2}{4} - b\right)^{-1/2} \cdot (-1/2(a) - 1) \quad (\text{A.15})$$

$$\frac{\partial f}{\partial R_{final}} = 0 + \frac{1}{2} \cdot \left(\frac{a^2}{4} - b\right)^{-1/2} \cdot \left(0 + 0 + \frac{1}{2\tau}\right) \quad (\text{A.16})$$

$$= \frac{1}{2} \cdot \left(\frac{a^2}{4} - b\right)^{-1/2} \cdot \frac{1}{2\tau} \quad (\text{A.17})$$

The values which are inserted in the above equations are derived as follows:

- R_i : raw rates in detector number i
- $R_{rand,i}$: rate of events in detector number i that are uncorrelated to events in the other detector
- $\sigma_{rand,i}$: uncertainties on the rates $R_{rand,i}$
- R_{final} : rate of the coincident events
- σ_{final} : uncertainties on the rates R_{final}
- R_{CS} : rate of Compton scattering events
- R_{RS} : rate of random coincident events
- τ : time window for the coincidence cut ($300 \cdot 10^{-9}$ s)

List of Figures

1.1	Cygnus X-1, Illustrations.	2
1.2	Cygnus X-1, Spectra of the two Main States.	2
1.3	Illustration of the Low Hard State, LHS	3
1.4	Illustration of the High Soft State, HSS	4
1.5	Compton Scattering Process	6
1.6	Θ -Differential Cross-sections for Incoherent Scattering (IS), in Silicon (Z=14), for three different energies	7
1.7	Schematic Illustration of a COMPTEL Type Compton Telescope	8
1.8	Polar Plot of the Differential Cross-section for Incoherent Scattering in Silicon for an Incident Photon with an Energy of 100 keV	9
1.9	Exemplary Data and Fit of the Cosine Modulation of the Azimuthal Scattering Angle Distribution for Polarized Photons	10
2.1	Band Structures of an Insulator, a Semiconductor, and a Conductor.	12
2.2	Combining p-Type and n-Type Semiconductor Materials to build a Diode	13
2.3	Schematic Sketch of a Silicon Drift Detector	14
2.4	Detector Setup of the ComPol CubeSat	16
2.5	Module Design and Prototype of the Silicon Drift Detector	17
2.6	Energy Resolution depending on the Shaping Time	18
2.7	Energy Resolutions of the SDD	19
2.8	Energy Resolutions of the LaBr ₃ Calorimeter	19
3.1	Prototype SDD Modul and the LaBr ₃ Scintillator	22
3.2	Schematic Sketch of the Setup	23
3.3	Photograph of the Setup	23
3.4	Signal Processing in the Cubes and the AC-Coupling	25
3.5	Photograph of the Data Acquisition System (DAQ)	25
3.6	Sketch of the Dark-box and Photograph of the Look inside the Dark-box	27
3.7	Geometrical Determination of the Scattering Angles	28
3.8	Positions of the Source in Measurements with Two Source Positions	29
3.9	Position of the Source in Measurements in the Rearranged Setup	30
3.10	Analysis Chain schematically	31
3.11	Energy Calibration	33
3.12	Coincidence Cut	33
3.13	Energy Cuts	34
3.14	Reconstruction of the Scattering angle	34
3.15	Model describing the measured Cross-section	35
3.16	Calibrated ⁵⁵ Fe spectra and Resolutions for all channels	36
3.17	Evolving Setup for measurements at angles > 90°,exemplary	37

3.18	Energy Spectra and energy cuts SDD channel 6 for two angles, exemplary .	38
3.19	Measurement without shielding: Compton Event rates depending on the scattering angle Θ	39
3.20	Investigation of Random coincident Events	40
3.21	Transmission Probability through a 3 mm Al plate	40
3.22	Improvements through Implementing a 3 mm Al Shielding between Source and SDDs	41
3.23	Shielding of Random Coincident Events	42
3.24	Measurement with 3 mm Al shielding: Compton Event rates depending on the scattering angle Θ	42
3.25	Transmission Probability through a 5 mm Cu plate	43
3.26	Measurements with 5 mm Cu and 3 mm Al shielding: Compton Event rates depending on the scattering angle Θ	44
3.27	Measurements with Collimator and 3 mm Al Shielding: Compton Event rates depending on the scattering angle Θ	45
3.28	Estimation of the attenuation through 1.8 mm PCB	46
3.29	Rearranged setup, Collimator with 3 mm Al shielding	46
3.30	Measurements in the Rearranged Setup: Compton Event rates depending on the scattering angle Θ	47
3.31	Calibrated ^{55}Fe spectra and Resolutions for all SDD channels, repeated . .	48
3.32	Measurements (final) in the rearranged Setup: Compton Event rates depending on the scattering angle Θ	48
3.33	Required Energy Threshold depending on the scattering angle Θ	49
3.34	Geometry of the SDDs used for Simulations	51
3.35	Setup for Simulation and source position, two angles exemplary	51
3.36	Analysis chain for Simulations	52
3.37	Evaluation of a LaBr_3 spectrum from Simulation, exemplary for $\Theta=110^\circ$. .	53
3.38	Evaluation of a SDD spectrum from Simulation, exemplary for $\Theta=110^\circ$. .	54
3.39	Influence of the lower Energy Threshold in the SDD module	55
3.40	Investigation of the reduced Number of Compton Events in the angular range around 90°	56
3.41	Influence of the Energy Threshold on the detectable Energy Range	57
3.42	Minimum Detectable Polarization, Threshold 1 keV	58

Bibliography

- [1] <https://commons.wikimedia.org/w/index.php?curid=15406373>. [Online; accessed 2023-03-23].
- [2] https://www.nasa.gov/sites/default/files/cygnus1_ill.jpg. [Online; accessed 2023-03-23].
- [3] <https://www.rexon.com/LBRBLANKSPEC.pdf>. [Online; accessed 2023-04-24].
- [4] <https://www-pub.iaea.org/MTCD/publications/PDF/TCS-51/html/topics/216.html>. [Online; accessed 2023-04-27].
- [5] Caen user manual. https://www.caen.it/products/compass/UM5960_Compass_UserManual_rev18.pdf. [Online; accessed 2023-04-22].
- [6] Geant4 collaboration. <https://geant4.web.cern.ch/>. [Online; accessed 2023-04-27].
- [7] Geogebra, a dynamical geometry software. <https://www.geogebra.org/>. [Online; accessed 2023-04-22].
- [8] Introduction to silicon photo-multipliers. https://www.first-sensor.com/cms/upload/appnotes/AN_SiPM_Introduction_E.pdf. [Online; accessed 2023-04-4].
- [9] Nasa cubesat. https://www.nasa.gov/sites/default/files/atoms/files/nasa_csli_cubesat_101_508.pdf. [Online; accessed 2023-03-31].
- [10] Nudat3 database. <https://www.nndc.bnl.gov/nudat3/>. [Online; accessed 2023-04-22].
- [11] Burkhard Beckhoff, Birgit Kanngießer, Norbert Langhoff, Reiner Wedell, and Helmut Wolff. *Handbook of practical X-ray fluorescence analysis*. Springer Science & Business Media, 2007.
- [12] Charles Thomas Bolton. Identification of cygnus x-1 with hde 226868. *Nature*, 235(5336):271–273, 1972. <https://doi.org/10.1038/235271b0>.
- [13] C Brocksopp, AE Tarasov, VM Lyuty, and P Roche. An improved orbital ephemeris for cygnus x-1. *arXiv preprint astro-ph/9812077*. <https://doi.org/10.48550/arXiv.astro-ph/9812077>.
- [14] T Brunst, S Mertens, K Altenmüller, T Houdy, D Siegmann, M Slezák, A Alborini, L Bombelli, M Carminati, C Fiorini, et al. Development of a silicon drift detector

- system for the tristan project—future search for sterile neutrinos. *Nuclear Instruments and Methods in Physics Research Section A: Accelerators, Spectrometers, Detectors and Associated Equipment*, 936:235–236, 2019. <https://doi.org/10.1088/1361-6471/abc2dc>.
- [15] Max Camenzind. *Compact objects in astrophysics*. Springer, 2007.
- [16] Floriane Cangemi, Jérôme Rodriguez, Victoria Grinberg, Philippe Laurent, and Joern Wilms. High energy spectral study of the black hole cygnus x-1 with integral. *arXiv preprint arXiv:1810.12049*, 2018. <http://arxiv.org/abs/arXiv:1810.12049>.
- [17] Arthur H Compton. Wave-length measurements of scattered x-rays. *Physical Review*, 21(6):715, 1923. <https://doi.org/10.1103/PhysRev.22.409>.
- [18] Wolfgang Demtröder and Wolfgang Demtröder. *Atome, Moleküle und Festkörper*. Number Wolfgang Demtröder ; 3 in *Experimentalphysik*. Springer Spektrum, Berlin Heidelberg, 5., neu bearbeitete und aktualisierte auflage edition, 2016. OCLC: 936378433.
- [19] Frank Edzards. *Characterization of Point Contact Germanium Detectors and Development of Signal Readout Electronics for LEGEND*. PhD thesis, TU München Munich, 2021.
- [20] Richard B Firestone and Virginia S Shirley. *Table of isotopes, 2 volume set*. 1998.
- [21] Katrin Geigenberger. Mechanical design and shielding against optical photons for the compol-iss in-orbit-verification mission. Master’s thesis, TU München Munich, 2022.
- [22] Cynthia Glas. Background studies for the compol cube-satellite. Master’s thesis, TU München Munich, 2022.
- [23] Aleksandar Gostojic. *Development of a Compton Telescope with 3D Imaging Calorimeter for Gamma-Ray Astronomy*. PhD thesis, Université Paris-Saclay, Paris-Saclay, 2016.
- [24] V Grinberg, K Pottschmidt, M Böck, C Schmid, MA Nowak, P Uttley, JA Tomsick, J Rodriguez, N Hell, A Markowitz, et al. Long term variability of cygnus x-1.vi. energy-resolved x-ray variability 1999–2011. *Astronomy & Astrophysics*, 565:A1, 2014. <https://doi.org/10.1051/0004-6361/201321128>.
- [25] WM Higgins, A Churilov, E Van Loef, J Glodo, M Squillante, and K Shah. Crystal growth of large diameter labr3: Ce and cebr3. *Journal of Crystal Growth*, 310(7-9):2085–2089, 2008. <https://doi.org/10.1016/j.jcrysgro.2007.12.041>.
- [26] Markus Hohenwarter, Daniel Jarvis, and Zsolt Lavicza. Linking geometry, algebra, and mathematics teachers: Geogebra software and the establishment of the international geogebra institute. *International Journal for Technology in Mathematics Education*, 16(2), 2009.
- [27] John H. Hubbell, Wm. J. Veigele, Edward A. Briggs, R. T. Brown, Don T. Cromer, and ROBERT J. Howerton. Atomic form factors, incoherent scattering functions, and photon scattering cross sections. *Journal of Physical and Chemical Reference Data*, 4:471–538, 1975. <https://doi.org/10.1063/1.555523>.

- [28] Oskar Klein and Yoshio Nishina. Über die streuung von strahlung durch freie elektro-
nen nach der neuen relativistischen quantendynamik von dirac. *Zeitschrift für Physik*,
52(11-12):853–868, 1929. <https://doi.org/10.1007/BF01366453>.
- [29] G. F. Knoll. *Radiation Detection and Measurement*. Wiley, USA, 2010.
- [30] Philippe Laurent, J Rodriguez, J Wilms, M Cadolle Bel, K Pottschmidt, and V Grin-
berg. Polarized gamma-ray emission from the galactic black hole cygnus x-1. *Science*,
332(6028):438–439, 2011. <https://doi.org/10.1086/306683>.
- [31] Philippe Laurent and Lev Titarchuk. The converging inflow spectrum is an intrinsic
signature for a black hole: Monte carlo simulations of comptonization on free-falling
electrons. *The Astrophysical Journal*, 511(1):289, 1999. <https://doi.org/10.1126/science.1200848>.
- [32] P. Lechner et al. Silicon drift detectors for high resolution room temperature X-
ray spectroscopy. *Nucl. Instr. Meth. A*, 377:346, 1996. [https://doi.org/10.1016/0168-9002\(96\)00210-0](https://doi.org/10.1016/0168-9002(96)00210-0).
- [33] Wilfried Ley, Klaus Wittmann, and Willi Hallmann. *Handbuch der Raumfahrttechnik*.
Carl Hanser Verlag GmbH Co KG, 2019.
- [34] Daniel Maier. *Development of a stacked detector system and its application as an
X-ray polarimeter*. PhD thesis, Citeseer, 2015.
- [35] Jordan Vannitsen Marco Agnan and Yun-Peng Tsai. Feasibility study for the compol
mission. *ODY SSEUS Space Inc. 2018*.
- [36] Matthias Meier. Tristan fly high - design studies for a cubesat compton telescope.
Master’s thesis, TU München Munich, 2019.
- [37] James CA Miller-Jones, Arash Bahramian, Jerome A Orosz, Ilya Mandel, Lijun Gou,
Thomas J Maccarone, Coenraad J Neijssel, Xueshan Zhao, Janusz Ziółkowski, Mark J
Reid, et al. Cygnus x-1 contains a 21–solar mass black hole—implications for massive
star winds. *Science*, 371(6533):1046–1049, 2021. <https://arxiv.org/pdf/2102.09091.pdf>.
- [38] F Perotti and C Fiorini. Observed energy dependence of fano factor in silicon at hard
x-ray energies. *Nuclear Instruments and Methods in Physics Research Section A:
Accelerators, Spectrometers, Detectors and Associated Equipment*, 423(2-3):356–363,
1999. [https://doi.org/10.1016/S0168-9002\(98\)01264-9](https://doi.org/10.1016/S0168-9002(98)01264-9).
- [39] Jérôme Rodriguez, Victoria Grinberg, Philippe Laurent, Marion Cadolle Bel, Katja
Pottschmidt, Guy Pooley, Arash Bodaghee, Jörn Wilms, and Christian Gouiffes.
Spectral state dependence of the 0.4–2 mev polarized emission in cygnus x-1 seen
with integral/ibis, and links with the ami radio data. *The Astrophysical Journal*,
807(1):17, 2015. <https://doi.org/10.1088/0004-637X/807/1/17>.
- [40] Helmuth Spieler. *Semiconductor detector systems*, volume 12. Oxford university press,
2005.
- [41] Tod E Strohmayer and Tim R Kallman. On the statistical analysis of x-ray po-
larization measurements. *The Astrophysical Journal*, 773(2):103, 2013. <https://doi.org/10.1088/0004-637X/773/2/103>.

-
- [42] Martin C Weisskopf. X-ray polarimetry: historical remarks and other considerations. *X-Ray Polarimetry: A New Window in Astrophysics*, 1:1–8, 2010. <https://doi.org/10.1017/CB09780511750809.002>.
- [43] Jörn Wilms, MA Nowak, Katja Pottschmidt, Guy G Pooley, and Sonia Fritz. Long term variability of cygnus x-1-iv. spectral evolution 1999–2004. *Astronomy & Astrophysics*, 447(1):245–261, 2006. <https://doi.org/10.1051/0004-6361:20053938>.
- [44] Janusz Ziółkowski. Evolutionary constraints on the masses of the components of the hde 226868/cyg x-1 binary system. *Monthly Notices of the Royal Astronomical Society*, 358(3):851–859, 2005. <https://arxiv.org/abs/astro-ph/0501102>.
- [45] Andreas Christian Zoglauer. *First Light for the next Generation of Compton and Pair telescopes*. PhD thesis, Technische Universität München, 2005.

Acknowledgements

I would like to take this opportunity to thank everyone who supported me during my master's thesis and also during my studies.

First I would like to thank Prof. Dr. Susanne Mertens for giving me the opportunity to write my master's thesis at her chair. I learned a lot during my time in her group.

I would also like to thank Matthias Meier for his patience in explaining the electronics in the Lab to me and for the support and proofreading of my work.

I would also like to thank Florian Henkes who supported me with his knowledge of computer science beyond python and my roommates Markus Kandler and Pia Voigt for discussions beyond physics and all the other members of the group who have accepted me into the group.

Special thanks to my children Teresa, Clara and Robert and my husband Christian Wenhart for accepting me as an unusual mother/wife and for their great support.